Etude de matériaux pour mémoires à changement de phase : effets de dopage, de réduction de taille et d'interface

Giada Eléonora Ghezzi

UNIVERSITÉ DE GRENOBLE

THÈSE

Pour obtenir le grade de

DOCTEUR DE L'UNIVERSITÉ DE GRENOBLE

Spécialité : **Physique**

Arrêté ministériel : 7 août 2006

Présentée par

Giada Eleonora Ghezzi

Thèse dirigée par **Françoise Hippert**
et codirigée par **Sylvain Maîtrejean**

préparée au sein **CEA Leti, Minatec campus et LMGP (CNRS, Grenoble-INP, Minatec**
et de **Ecole Doctorale de Physique**

Material studies for advanced phase change memories: doping, size reduction and interface effect

Thèse soutenue publiquement le **25 février 2013**,
devant le jury composé de :

Pr. Yves Bréchet
Professeur Grenoble INP, Président
Pr. Olivier Thomas
Professeur Université d'Aix-Marseille, Rapporteur
Pr. David Wright
Professor University of Exter, Rapporteur
Dr. Christophe Bichara
Directeur de recherche CNRS, Examinateur
Dr. Paola Zuliani
Project leader at ST Microelectronics, Examinatrice
Françoise Hippert
Professeur Grenoble INP, Directeur de thèse
Sylvain Maîtrejean
Ingénieur-chercheur CEA, Co-Directeur de thèse

To my beloved family

Contents

Summary

Phase Change Memories (PCM) are considered the best candidate for the next generation of non volatile memories (NVM), which market is actually dominated by Flash technology. PCM are based on the properties of some chalcogenide materials, called phase change (PC) materials, to reversibly switch between a crystalline and an amorphous phase. These two phases are characterized by very different electrical and optical properties, which makes possible to store information. For PCM to be competitive a great research effort is still needed. This effort should be directed to improve technological aspects such as device architecture, layout and control circuitry, but also to optimize the PC materials used in the memory cell. The effect of scaling and interface layers on the PC materials properties must also be understood. Up to now the most used and studied PC material is $Ge_2Sb_2Te_5$ (GST), sometimes doped with nitrogen, but research is extremely active in looking for other compounds that can offer better properties. Materials to be used in PCM should crystallize fast, exhibit large optical and electrical contrast between the amorphous and crystalline phases, have a melting temperature sufficiently low to limit the electric power needed for amorphization and their amorphous phase must be stable to grant good retention performances. PC materials doping has been identified as a promising solution for properties optimization. Moreover, those properties must not decay after many transformation cycles between the amorphous and crystalline states and must be kept with scaling, i.e. for a small amount of PC material embedded

in conducting and/or insulating materials. In this context, the aim of this work is to investigate the effect of scaling and doping on PC materials properties. Here, three directions have been explored. One is a contribution to understand the impact of doping on the structure of amorphous GeTe. The second one is an investigation of the effect of 3D confinement on the phase change in GST. The third one is the study of influence of interface materials on crystallization of GST and GeTe thin films.

In the first part of the thesis the local structural properties of C and N doped amorphous GeTe are investigated through X-ray scattering experiments performed at the synchrotron SOLEIL (Saclay, France). At the beginning of this work it was demonstrated that C and N doping improves drastically the data retention of GeTe and lowers the current needed for amorphization. The goal was to understand the impact of doping on the amorphous structure of GeTe by analyzing the pair distribution function of doped and undoped samples. The impact of doping is revealed experimentally by the appearance of a new peak in the pair distribution function of doped GeTe, indicating the formation of a bond at a new distance, absent in the undoped amorphous material. Ab initio simulations show the formation of new tetrahedral and triangular or pyramidal environments centered on carbon or nitrogen as well as long carbon chains and a few N_2 molecules. The new peak observed experimentally corresponds to Ge-Ge distances in the units centered on carbon or nitrogen. These structural changes can be related to the enhanced crystallization temperature and activation energy of C and N-doped GeTe.

The effect of confinement on the phase change in GST is the subject of the second part of this work. The capability of PC materials to be scaled while maintaining their properties is a fundamental requirement for further development of PCM. There have been many studies on thin films of varying thickness. In some cases the crystallization temperature has been reported to increase drastically with reduced dimensions for films thinner than 10 nm, up to the point of losing the phase change property for films thinner than 2 nm. These studies deal with confinement in only one direction, the film thickness, but the ideal system for studying the effect of scaling on PC materials in a memory cell (where both size

and interface effects play a role) is a set of nanoclusters. Indeed, the volume of clusters is confined in three dimensions and the interface effects are enhanced due to a larger surface/volume ratio. Nano-sized clusters of GST with an average size of around 5.7 nm ($\pm$ 1 nm) in a matrix of Al_2O_3 have been made using a sputtering gas phase condensation source and characterized by X-Ray diffraction measurements performed at the ESRF synchrotron (Grenoble). At the moment, those clusters are the smallest GST clusters ever deposited by sputtering, and with the narrowest size distribution. These clusters have been made by a method close to those used for PCM thin films deposition, thus giving information that can be easily exported to device fabrication. The crystallization temperature of clusters is around 180°C, only slightly above the crystallization temperature (155°C) of a 10 nm thin film of GST deposited under the same conditions and embedded in Al_2O_3 . The crystalline phase is the cubic metastable phase of GST for both clusters and thin film. The lattice parameter is larger in clusters than in thin films. The lattice variation can be explained by supposing that the surrounding rigid Al_2O_3 matrix exerts a tensile strain on the clusters and that their volume during crystallization is forced to remain constant and equal to their volume in the amorphous phase. Various effects could contribute to the difference in crystallization temperature between clusters and the 10 nm thin film, i.e. a composition effect, different surface to volume ratio, matrix influence, stress or strain effects or an intrinsic size effect.

The third part of this thesis is dedicated to a study of the effect of interface layers on the crystallization temperature of GeTe and GST thin film (10 to 100 nm thick). Despite its broad scientific and technological interest, this subject has not been widely treated in literature up to now. First, measurements of the crystallization temperature of GST and GeTe 100 nm thin films embedded in three different materials (Ta, TiN and SiO_2) through reflectivity measurements are reported. It is observed that in both GeTe and GST interfaced with Ta the crystallization temperature is around 20°C higher than the one obtained by interfacing those materials with TiN or SiO_2 . Even if some studies in literature put in evidence the influence of interface over the crystallization temperature of Ge-Sb-Te thin films, such a remarkable interface effect in relatively thick films

(100 nm) was never reported before. The structural properties of the crystalline phase of GeTe films, such as the grain size and texture, are investigated through X-Ray diffraction analysis for the three different interface materials. The results show that the SiO_2 interfaced samples are characterized by a strong texture while a weak texture is observed for Ta and TiN interfaced samples. Moreover, the grain size calculated from the 012 Bragg peak width for SiO_2 interfaced samples is bigger than the ones calculated for Ta and TiN interfaces for a tilting angle of 40°of the sample. This suggest that for planes tilted by 40°compared to the (012) plane the SiO_2 /GeTe surface is energetically favorable, resulting in an abnormal growth with a preferred orientation with the (100) or (010) plane parallel to the sample surface. If this hypothesis is true, a different nucleation and growth mechanism for the different interfaced samples can be supposed.

In the last part, general conclusions and perspectives are presented.

Résumé

Les mémoires à changement de phase (PCM) sont l'un des candidats les plus prometteurs pour la prochaine génération de mémoires non-volatiles (NVM), dont le marché est dominé par la technologie Flash. Les PCM sont basées sur la propriété des certains matériaux chalcogénures, appelés matériaux à changement de phase (PC), de changer réversiblement d'état entre une phase cristalline et une phase amorphe. Ces deux phases sont caractérisées par des propriétés électriques et optiques très différentes, ce qui rend possible de stocker des informations. Pour que les PCM soient compétitives un grand effort de recherche est encore nécessaire. Cet effort devrait être dédié d'une part à l'amélioration des aspects technologiques, comme l'architecture des dispositifs, le layout et le circuit de contrôle, et d'autre part à l'optimisation des matériaux PC utilisés dans la cellule de mémoire. L'effet de la réduction de taille et celui des couches d'interface sur les propriétés de matériaux PC doivent aussi être compris. Jusqu'ici le matériau PC le plus utilisé et étudié est $Ge_2Sb_2Te_5$ (GST), parfois dopé avec de l'azote, mais la recherche est extrêmement active dans l'investigation d'autres composés qui peuvent offrir de meilleures propriétés. Les matériaux à utiliser dans les PCM doivent cristalliser vite, montrer un grand contraste optique et électrique entre les phases amorphes et cristallines, avoir une température de fusion suffisamment basse pour limiter l'énergie électrique nécessaire pour l'amorphisation et la stabilité de leur phase amorphe doit être grande pour garantir une bonne rétention des données. Le dopage des matériaux PC a été identifié comme une

solution prometteuse pour l'optimisation de propriétés. De plus, ces propriétés ne doivent pas se détériorer après beaucoup de cycles de transformation entre les états amorphes et cristallins et doivent être conservés quand la taille est réduite, c'est-à-dire pour une petite quantité de matériau PC incorporé entre des matériaux conducteurs et/ou des isolants. Dans ce contexte, le but de ce travail est d'examiner l'effet de la réduction de taille et du dopage sur les propriétés des matériaux PC. Trois axes ont été explorés. Le premier est une contribution pour comprendre l'impact du dopage sur la structure de GeTe amorphe. Le deuxième est une investigation de l'effet de confinement en 3D sur le changement de phase de GST. Le troisième est l'étude d'influence du matériau d'interface sur la cristallisation des films minces de GST et GeTe.

Dans la première partie de la thèse la structure locale de GeTe amorphe dopé avec C ou N est déterminée par des expériences de diffusion des rayons X exécutées au synchrotron SOLEIL (Saclay, France). Au début de ce travail il avait été démontré que le dopage par C ou N de GeTe améliore spectaculairement la rétention de données et baisse le courant nécessaire pour l'amorphisation dans les dispositifs. Le but était donc de comprendre l'impact du dopage sur la structure amorphe de GeTe en analysant la fonction de distribution de paires d'échantillons dopés et pas dopés. L'impact du dopage est révélé expérimentalement par l'apparition d'un nouveau pic dans la fonction de distribution de paires de GeTe dopé, indiquant la formation d'une liaison à une nouvelle distance, absente dans le matériau amorphe non dopé. Des simulations ab initio montrent la formation de nouveaux environnements tétraédriques, triangulaires ou pyramidaux centrés sur le carbone ou l'azote ainsi que des longues chaînes de carbone et quelque molécules d'N_2. Le nouveau pic observé expérimentalement correspond aux distances Ge-Ge dans les unités centrées sur le carbone ou l'azote. Ces changements structurels peuvent être reliés à l'augmentation de la température de cristallisation et de l'énergie d'activation du GeTe dopé C ou N.

L'effet de confinement sur le changement de phase de GST est le sujet de la deuxième partie de cette thèse. La capacité des matériaux PC à être confinés en maintenant leurs propriétés est une exigence fondamentale pour le

développement des PCM. Il y a eu beaucoup d'études sur des films minces d'épaisseur variable. Dans quelques cas, une très forte augmentation de la température de cristallisation a été trouvée pour des films plus minces que 10 nm, jusqu'au point de perdre la propriété de changement de phase pour des films plus minces que 2 nm. Ces études traitent du confinement dans une seule direction, l'épaisseur de film, mais le système idéal pour étudier l'effet de la réduction de taille sur des matériaux PC dans une cellule de mémoire (où tant la taille que les effets d'interface jouent un rôle) est un ensemble de nanoparticules. En effet, la taille des particules est limitée dans trois dimensions et les effets d'interface sont augmentés en raison d'un plus grand rapport surface/volume. Des agrégats de GST, avec une taille moyenne d'autour de 5.7 nm ($\pm$ 1 nm) et déposées dans une matrice de Al_2O_3 , ont été fabriqués par pulvérisation puis déposés et caractérisés par des mesures de diffraction des rayons X faites au synchrotron ESRF (Grenoble). À l'heure actuelle, ces particules sont les plus petites particules de GST jamais déposées par pulvérisation et avec la distribution de taille la plus étroite. Ces particules ont été fabriquées par une méthode proche de celle utilisée pour la déposition de films minces dans les dispositifs PCM, et donc les informations obtenues peuvent être facilement exportées vers la fabrication des dispositifs. La température de cristallisation des nanoparticules est autour de 180°C, seulement légèrement au-dessus de la température de cristallisation (155°C) d'un film mince de GST de 10 nm déposé dans les mêmes conditions et encapsulée par Al_2O_3 . La phase cristalline est la phase métastable cubique de GST tant pour les nanoparticules que pour le film mince. Le paramètre de maille est plus grand dans les nanoparticules que dans le film mince. On peut expliquer la variation de paramètre de maille en supposent que la matrice Al_2O_3 , qui est rigide, exerce une tension sur les nanoparticules et que leur volume pendant la cristallisation est forcé de rester constant et égal au volume occupé dans la phase amorphe. Divers effets pourraient contribuer à la différence entre la température de cristallisation des nanoparticules et du film mince de 10 nm, soit un effet de composition, la différence de rapport surface/volume, l'influence de la matrice, des effets de contraints et déformations ou un intrinsèque effet de taille.

La troisième partie de cette thèse est consacrée à une étude de l'effet de

couches d'interface sur la température de cristallisation de films minces de GeTe et GST (épaisseur de 10 à 100 nm). Malgré son large intérêt scientifique et technologique, ce sujet n'a pas été largement traité dans la littérature jusqu'ici. D'abord, la température de cristallisation de films minces de GST et GeTe de 100 nm encapsulés dans trois matériaux différents (Ta, TiN et SiO_2) est déterminée par des mesures de réflectivité. Il est observé que, tant dans le GeTe que dans le GST, la température de cristallisation obtenue dans le cas d'interface avec du Ta est autour 20°C plus haute que celle obtenue en interfaant ces matériaux avec TiN ou SiO_2 . Même si quelques études de la littérature ont mis en évidence l'influence d'interfaces sur la température de cristallisation de films minces de Ge-Sb-Te, un effet d'interface si remarquable dans des films relativement épais (100 nm) n'a jamais été rapporté auparavant. Les propriétés structurelles de la phase cristalline de films du GeTe, comme la taille de grains et la texture, sont examinées par diffraction des rayons X pour les trois différents matériaux d'interface. Les résultats montrent que l'échantillon interfacé avec SiO_2 est caractérisé par une texture forte tandis qu'une texture faible est observée pour les échantillons interfacés avec Ta et TiN. De plus, la taille de grains, calculée en utilisant la largeur du pic de Bragg 012, pour l'échantillon interfacé avec SiO_2 est plus grande que celle calculées pour les interfaces Ta et TiN pour un angle d'inclinaison de l'échantillon de 40°. Ceci suggère que l'interface SiO_2 /GeTe est énergétiquement favorable pour les plans inclinés de 40°par rapport aux plans 012, aboutissant à une croissance anormale dans cette direction. Si cette hypothèse est vraie, on peut supposer un mécanisme de nucléation et croissance différent pour les échantillons interfacés avec différents matériaux. Dans la dernière partie, des conclusions générales et des perspectives sont présentées.

Chapter 1

Phase Change Memories Overview

1.1 Introduction

The necessity to store informations has always been one of the basic needs of mankind throughout its history. In the last few decades, with the explosive developing of electronics and computers, this need became an urgency. Since the formulation of Moore's Law in 1965 [1] the microelectronics industry development has been ruled by the trend of reducing device cost of one half every two years. This has been achieved by conventional CMOS device architectures by increasing the integration density of devices, meaning reducing their dimensions or even developing new strategies as 3D device integration that allows higher density at the same device size. Floating gate non-volatile memories (NVM), usually named Flash memories, represent the mainstream in the NVM market. They have been the reference technology for years, but their further scaling become difficult due to technological and physical constraints. Already over the past few years, Flash memories have faced hard challenges for keeping the scaling trend and great difficulties arise for the next technology nodes that make hard to even maintain actual specifications.

As a consequence, there is a rising industrial interest for emerging alternative NVM technologies that can offer better scaling possibilities with even better memory performances than Flash memories. Among those alternatives the most interesting one is the Phase-Change resistive memory (PCM). PCM are based on the properties of some chalcogenide materials, called phase change (PC) materials, to reversibly switch between a crystalline and an amorphous phase. These two phases are characterized by very different electrical and optical properties and this makes possible to store the information in terms of '0' and '1' levels, as it will be described in details in section 1.2. Phase-change memories, also called Ovonic Unified Memory, offer a scalability beyond Flash technology and can potentially be better than Flash memories in terms of faster random access time, higher density and higher endurance [2].

The first to investigate extensively the switching properties of chalcogenides and to demonstrate their practicality was S. R. Ovshinsky, during the 1950s and 1960s [3]. In early 1970s the interest in PCM rose and a first 256-bit memory

array of phase change memory cells was developed by R. G. Neale, D. L. Nelson and G. E. Moore in 1970. However, the programming operation parameters of this memory were very poor. Other studies on phase change memory electrical devices have been done until 1978 but the enormous power required for programming constituted a strong limitation and they were abandoned (Chapter 1 of Ref. [4]). The reason for this enormous power consumption were the big dimensions of the memory cell. The PCM devices were not as competitive as the metal oxide semiconductor memories that were rising in market at those times, so the interest in PCM subsided and there were no further developments until the first years of 2000.

However, during the 1970s and 1980s chalcogenide materials continued to attract interest because of their suitability for use in optical memories. The most important result of this effort was the discovery in 1987, by Yamada and co-workers, of the $GeTe - Sb_2Te_3$ pseudobinary line [5] and in particular of the $Ge_2Sb_2Te_5$ compound, called GST [6]. The properties of those materials opened the way to the development of phase change optical recording devices such as Compact Disk (CD), Rewritable Compact Disk (CD-RW), Digital Versatile Disk (DVD) and Blue-Ray DVD. On the other hand, at the beginning of 2000s the new shrinking possibilities obtained through the great development of lithographic techniques triggered a new interest in phase change memory electrical devices [4]. The now reduced available volume of the memory cell, resulting in lower power consumption, led PCMs to be developed by the Research and Development departments of many industrial companies as Intel, STMicroelectronics and Samsung. Nowadays, PCMs are one of the best candidates to replace market-leader Flash Non Volatile Memories (NVM) that are approaching their critical size limit.

One of the open research subjects in the PCM field is material study and optimization. While the device architecture faces the challenges of scaling and vertical integration [2], new materials that can offer better performances should be investigated. A deeper understanding of the phase change mechanism and how PC materials structures are related to their properties is mandatory. Nowadays, this need is combined with the rising scientific interest of Phase Change

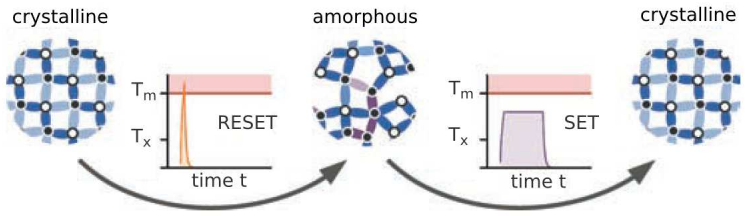

Figure 1.1: Basic principle of the phase transformation [8]. PC materials can switch reversibly between an amorphous state, corresponding to the logical level '0' or RESET, and a crystalline state corresponding to the logical level '1' or SET. The SET operation consists in programming the cell into the SET state, while the RESET operation consists in programming the cell into the RESET state. To obtain the amorphous phase the PC material must be annealed above its melting temperature and then rapidly cooled down. To obtain the crystalline phase the material must be annealed above its crystallization temperature T_x .

Materials. In the last years the importance of the basic research on PC materials has been confirmed by an increasing interest of the scientific community, and by the success of dedicated symposium as, for example, the Phase Change symposium in the Material Research Society Spring conference. The number of articles dedicated to studies of the fundamental properties of PC materials has rose in the last years (see for example Ref. [7] and [8]), confirming that this is an active and promising research field.

The aim of this thesis is to study those materials, focusing on the effect of doping well known compounds, the effect of different material interfaces and the shrinking effect on very small nanoparticles. The following of this first Chapter will be dedicated to an introduction on PCM basic working principle (Section 1.2), the description of the theory of amorphization and crystallization (Section 1.3) and a brief review of the main structural characteristics of PC materials, focusing on the structure of the well known compounds GeTe and GST (Section 1.4).

1.2 Phase Change Memories working principle

Phase change memories (PCM) are based on the property of so called phase change materials (PC materials) to change reversibly between an amorphous and a crystalline state, as schematically shown in Figure 1.1.

The phase change is obtained through heating of the material. In memory devices the heating can be provided by electric or laser pulses. If a PC material is heated above its melting temperature T_m and cooled down quickly (with a cooling rate of $10^9 - 10^{11} K/s$) it solidifies in a glassy structure, the amorphous phase. The glass is in a metastable state so it will tend to crystallize on very long time scale. This time should be of the order of several years since it determines the capability to maintain the information. If the amorphous material is annealed for a sufficiently long time (usually tens of nanoseconds) below T_m but above its crystallization temperature T_x , it switches to the crystalline phase. The theory of the phase change mechanism will be explained with more details later in Section 1.3. The two phases are characterized by very different optical and electrical parameters, thus providing the contrast required to distinguish between logical states. For example, the amorphous phase exhibits a high value of resistivity and a low value of reflectivity, and vice-versa for the crystalline phase. The optical contrast between the amorphous and crystalline phase is illustrated in Figure 1.2 for the case of $Ge_2Sb_2Te_5$.

The phase change property allows to store an information by associating the logical level '0' and '1' to the two different phases. Traditionally, the level '0' (or RESET level) has been associated to the amorphous phase and the level '1' (or SET level) to the crystalline phase. Crystallization is the slowest process involved. It must occur quickly in the programming operation in order to achieve fast programming speed, but the spontaneous crystallization of the metastable amorphous phase should not take place for many years at room temperature in order to grant data retention. This means that the crystallization rate of PC materials must increase by orders of magnitude with the change in temperature between room temperature and T_x .

In the following sections the working principle of a schematic cell device will be explained and the programming curves and electrical characteristics of the cell will be presented.

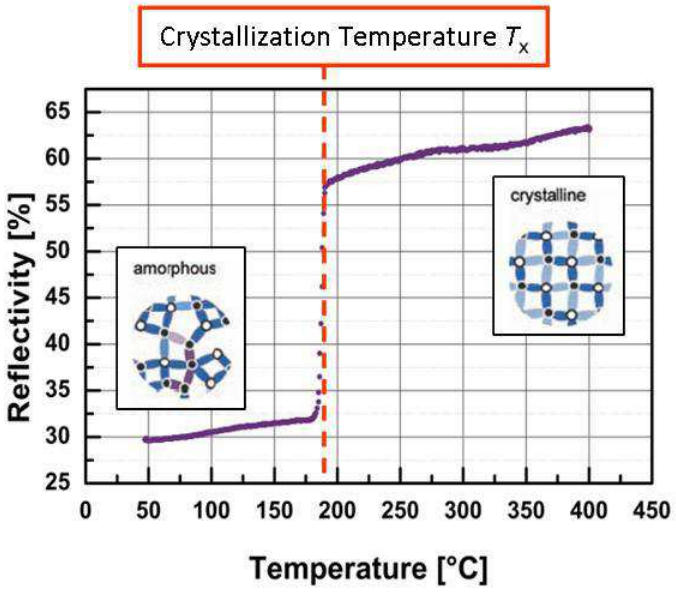

Figure 1.2: Evidence of the different optical properties of the PC material $Ge_2Sb_2Te_5$ in the amorphous and crystalline phases. The reflectivity of GST is reported as a function of temperature starting from an initially amorphous sample. The amorphous phase is characterized by a low reflectivity value compared to the one of the crystalline phase. On the graph it is easy to identify the crystallization temperature at which the phase transformation occurs.

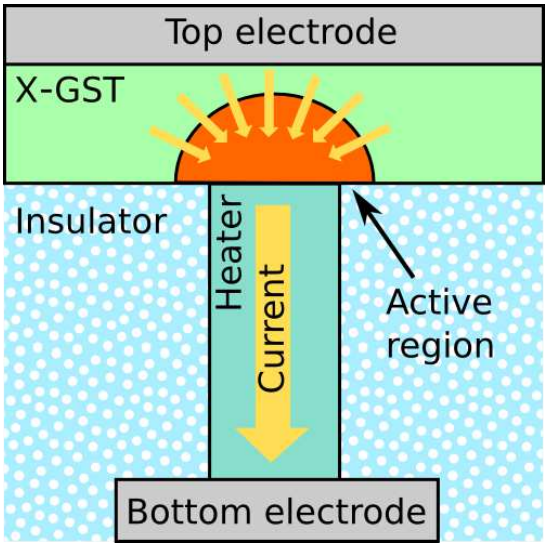

Figure 1.3: Schematic representation of the lance-like structure of a PCM cell device. The PC material is interfaced with a top electrode and a bottom electrode (heater).

1.2.1 Basic device example

The schematic picture of a Ovonic Unified Memory (OUM) PCM cell in its simplest form (lance-like structure) is reported in Figure 1.3.

The device consists in a thin film of PC material which is electrically accessible by a *top electrode* and a *bottom electrode*, also called *heater* . For almost all the PC materials integrated in devices the as-fabricated cell is entirely crystalline, due to the high temperatures reached in fabrication process. In order to read and program the cell, an imposed external voltage is applied at the electrodes generating a current that flows from to the top electrode the heater through the PC material. To read the state of the cell a low power current pulse is imposed and the overall resistance of the cell is measured. If the resistance is high the cell is in the RESET state, while if the resistance is low the cell is in the SET state. It is worth noting that the cell is considered to be in the SET state when the read resistance value is sufficiently low, and this can be achieved by the formation of crystalline paths percolating through the amorphous volume and not necessarily by crystallizing the entire volume. Concerning the program operations, the shape and intensity of the applied current pulse determines if the cell will be programmed in the amorphous state (RESET operation) or in

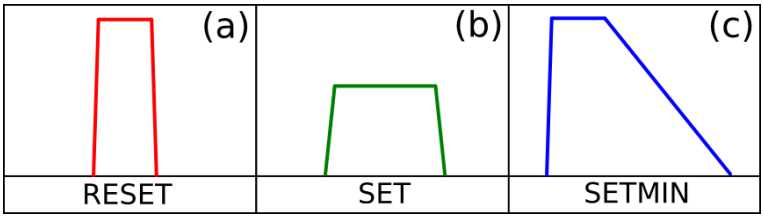

Figure 1.4: Current pulses for the programming operation of the cell. RESET pulse (a) SETMIN pulse (b) and SET pulse (c).

the crystalline state (SET or SETMIN operation) as shown in Figure 1.4. The contact area between the PC material and the heater is very narrow so the current density reaches its highest value at the PC material - heater interface. As shown in Figure 1.4a, for the RESET operation a current pulse of high intensity with a rapid falling edge is applied (RESET pulse) so that the current density at the PC material / heater interface is sufficiently high to heat the PC material over the melting temperature by Joule heating. The abrupt falling edge of the RESET pulse induces a fast quench of the material that solidifies in the amorphous phase in an hemispherical volume. Amorphization of this area blocks the low-resistive current path and results in an overall large resistance. It is worth underlining that reducing the heater dimension, meaning reducing the cell size, results in an increased current density so that the current required for amorphization is reduced. The SET pulse can be chosen to have the same shape as the RESET pulse but with a lower intensity and a longer duration (SET pulse, Figure 1.4b) or an intensity sufficiently high to melt the PC material but with a slow falling edge (SETMIN pulse, Figure 1.4c). In the first case the PC material is heated below its melting temperature and the amorphous to crystalline transition is induced. Usually the transformation does not involve all the amorphous volume but results in the creation of percolating paths, as explained before. Thus the overall resistance is higher than the resistance of an entirely crystalline cell, but still two or three order of magnitude lower than the RESET value. In the SETMIN case the PC material is first melted and then crystallized by a slow quenching and the final resistance value is lower than in the SET case.

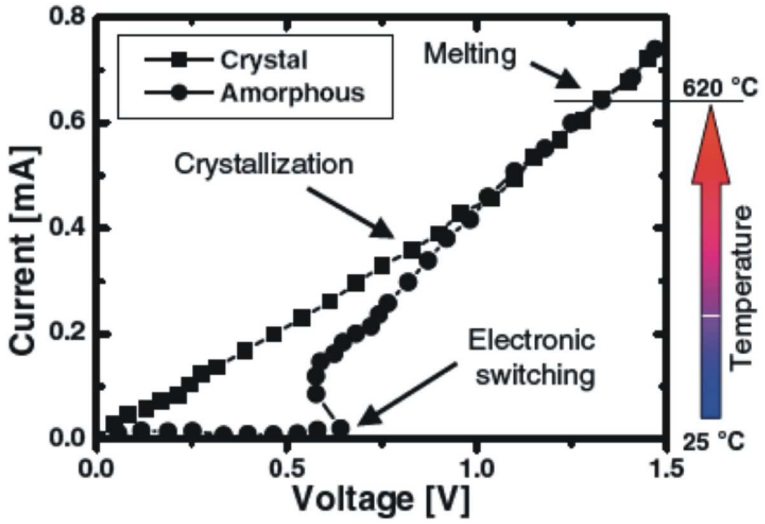

Figure 1.5: I-V characteristic of a PCM cell in the crystalline and amorphous states (from Ref.[9]). The I-V characteristic of the amorphous state present a snap-back in correspondence of a threshold voltage that is not present in the crystalline I-V curve.

1.2.2 Electrical conduction model

The mechanism of electrical conduction in phase change memories is a very active research field, due to the important role of electrical properties in devices. The current-tension (I-V) characteristic of a PCM cell is reported in Figure 1.5. It is possible to distinguish between a low electrical field region and an high electrical field region. For low applied voltages (low electrical field region) the GST amorphous conductance is low compared to the crystalline GST conductance. When the external bias reaches a certain value (called threshold switching voltage) a *snap-back* takes place and the conductance abruptly switches to a higher value. This threshold switching, also called Ovonic Threshold Switching (OTS), was first discovered by Ovshinsky [3]. The crystalline GST I-V curve presents no evidence of such a switching and in the high field region the conductances of both states are equal. It is important to underline that the threshold switching does not correspond to the amorphous to crystalline transition. After the switching takes place, the cell remains amorphous until Joule heating is sufficient for inducing crystallization. The OTS is fundamental in order to grant low power dissipation during the SET operation. When the voltage applied to the amorphous cell exceeds the threshold value, the current flowing through it

increases drastically, allowing the phase transition to take place with a low applied power. Without the switching phenomenon, the high power required to perform the SET operation would make the programming operation unpractical. The physical mechanism for OTS has been widely investigated. Even if it is still not conclusively clarified, it is generally supposed to be an electronic effect rather than a thermal or structural effect. Ielmini and Zhang proposed a model for conduction [10, 11] described by the Poole-Frenkel effect that well describes the transport properties of the crystalline and amorphous phases as well as the switching effect.

1.3 Physics of phase change transformations

1.3.1 Amorphization

As already stated in the introduction, the amorphous phase can be obtained from the melt by a rapid quench, fast enough to avoid crystallization. If a liquid is cooled below its melting temperature T_m it does not crystallize instantaneously and it can be undercooled. While the temperature decreases, the liquid viscosity η increases. Such an undercooled liquid is in a metastable equilibrium, meaning that it is metastable with respect to the crystalline stable phase but it is still in its internal equilibrium. If the undercooled liquid is cooled down below the so-called *glass transition temperature* T_g it becomes configurationally frozen, losing the thermal equilibrium, and it becomes a glass. T_g is commonly defined as the temperature at which the time scale necessary for atomic rearrangements becomes larger than the measurement time, and it usually occurs at the point where the viscosity equals 1×10^{12} Pa s [12, 8]. Below T_g the glass has a very low microscopic atomic mobility $D(T)$, which is inversely proportional to the macroscopic viscosity $\eta(T)$ according to the Stokes-Einstein relation $D(T) \propto T/\eta(T)$.

Crystallization is thermodynamically forbidden above T_m and it is extremely slow below T_g , while it can rapidly occur for temperatures between T_g and T_m. For temperatures slightly below T_m the driving force for crystallization is so low that crystallization would occur only very slowly, so with a rapid

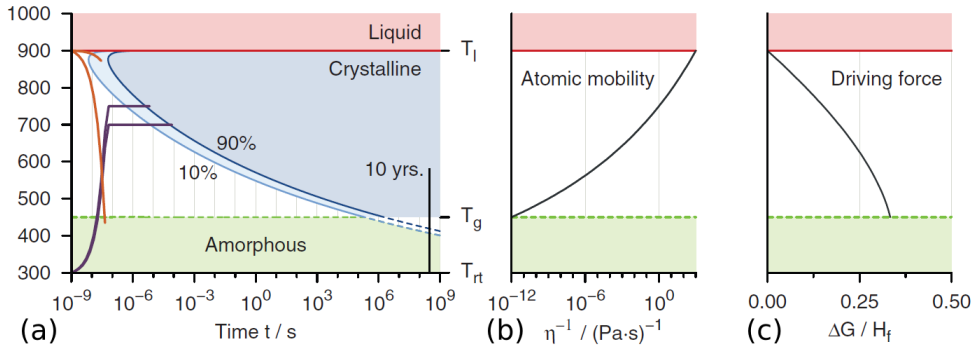

Figure 1.6: Time-temperature-transformation (TTT) diagram for a PC material taken from Reference [8]. The phase transformation of a fixed volume of PC material is reported depending on the time spent at a certain temperature. The two orange lines on the graph indicate two different constant rate quenching processes while the two purple lines indicate two annealing processes starting at room temperature.

quenching of the liquid below T_g it is possible to avoid crystallization and result in the formation of the amorphous phase. This is illustrated in Figure 1.6a, reported from Ref. [8], in which the phase transformation is shown in terms of a time-temperature-transformation (TTT) diagram. The corresponding mobility and the driving force for crystallization are reported in Fig. 1.6b and 1.6c, respectively. In the TTT diagram the phase transformation of a fixed volume of PC material is reported, depending on the time spent at a certain temperature. The two orange lines on the graph indicate two different constant rate quenching processes. If the cooling is sufficiently fast (around $10^9 K/s$) crystallization can be avoided slightly below T_m due to the very low driving force for crystallization (Figure 1.6c). With further fast undercooling, the driving force increases but the mobility decreases and if T_g is reached the material becomes amorphous. On the other hand, if the cooling rate is too slow the material will crystallize.

The amorphous phase can crystallize below T_g only for very long times. This time has a very important role in determining the data retention in a memory cell, as it defines the time at which a cell in the RESET state will crystallize losing the stored information. On the TTT graph are also reported in purple two annealing processes starting at room temperature, showing that crystallization time and temperature are dependent.

1.3.2 Crystallization

Two different process contributes to crystallization of an amorphous solid.The first one is the *nucleation*, that initiates the crystallization through the formation of small crystalline nuclei. The second one is the *growth* of those nuclei to a macroscopic size. The so-called *classical nucleation theory* of steady state nucleation has been developed by Volmer, Weber, Becker, Doring, Turnbull and Fisher during the first decades of the 20th century [13, 14, 15, 16], based on the pioneering work of Gibbs [17].

1.3.3 Nucleation

Nucleation can occur in two different ways. In the first and simplest case, called *homogeneous nucleation*, the crystallite germinates inside the amorphous phase, without involving other substances. If instead the amorphous phase is in contact with other substances that act as preferred sites for nucleation, an *heterogeneous nucleation* occurs.

Homogeneous Nucleation

Form Gibbs' thermodynamical theory, clusters of radius r can be formed inside the amorphous phase by thermodynamics fluctuations. Their equilibrium distribution is ruled by the Boltzmann statistic, meaning that the number of clusters of radius r at equilibrium is

$$N^{equ}(r) = N_0 \cdot exp(-\frac{\Delta G_{cluster}(r)}{k_B T}) \tag{1.1}$$

where N_0 is the total number of atoms in the liquid, $\Delta G_{cluster}(r)$ is the reversible work for crystal cluster formation, k_B is the Boltzmann constant and T is the absolute temperature. $\Delta G_{cluster}(r)$ can be written as

$$\Delta G_{cluster}(r) = -\Delta G_{lc,V} \cdot \frac{4}{3}\pi r^3 + 4\sigma\pi r^2 \tag{1.2}$$

where $\Delta G_{lc,V}$ is the Gibbs free energy difference per volume between the crystalline and the amorphous phase and $\sigma > 0$ is the interfacial free energy. $\Delta G_{lc,V}$ is zero at T_m and positive for $T <\mathrm{T}_m$. So Eq. 1.2 is composed of a negative volume term that becomes larger as the temperature T is reduced below

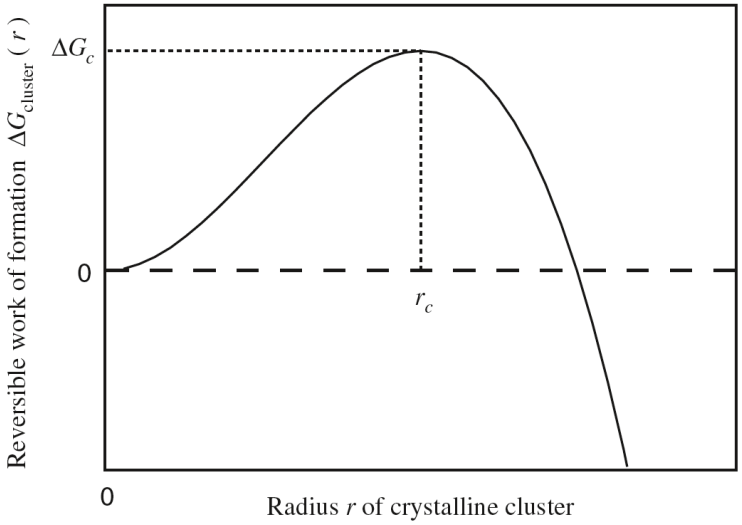

Figure 1.7: Evolution of $\Delta G_{cluster}(r)$ as a function of r corresponding to Eq. 1.2, taken from Chapter 7 of Reference [4]. The curve exhibit a maximum for the $r = r_c$ (critical radius) that corresponds to the critical work for cluster formation ΔG_c.

T_m and a surface term, always positive, that results from the creation of a cluster/liquid interface. The evolution of $\Delta G_{cluster}(r)$ as a function of r is depicted qualitatively in Figure 1.7.

The curve present a maximum at

$$r_c = \frac{2\sigma}{\Delta G_{lc,V}} \tag{1.3}$$

where the *critical radius* r_c is of the order of a few nanometers. The energy of a nucleus of radius r_c may be calculated by substituting r_c to r in 1.3, thus obtaining the *critical work for cluster formation* ΔG_c

$$\Delta G_c = \Delta G_{cluster}(r_c) = \frac{16\pi}{3}\frac{\sigma^3}{(\Delta G_{lc,V})^2}. \tag{1.4}$$

Clusters with radius $r = r_c$ are the so-called *critical clusters*. The evolution to bigger dimensions of clusters with $r < r_c$ is energetically not favorable so they spontaneously decay, while clusters with $r > r_c$ can grow due to the free energy gain. This means that ΔG_c constitutes a barrier against crystallization, the same barrier that impedes immediate crystallization of the amorphous phase when it is undercooled below T_m .

The approach of Gibbs is purely thermodynamic, and on its basis a first kinetic model for nucleation was developed by Volmer and Weber [13, 14]. They

modified Eq. 1.1 by taking into account the fact that it becomes unphysical for $r > r_c$, where the clusters distribution at equilibrium begin to increase with increasing r. To avoid this, $N^{equ}(r)$ was set to zero for $r > r_c$. By considering that the nucleation occurs when a critical cluster gains one more atom, the *nucleation rate* was calculated per unit volume per second

$$I^{equ} = s_c \cdot k \cdot N^{equ}(r_c) = s_c \cdot k \cdot N_0 \cdot exp(-\frac{\Delta G_c}{k_B T}) \tag{1.5}$$

where k is the arrival rate to the crystalline cluster of amorphous phase atoms and s_c is the number of surface atoms of the cluster.

One of the limitation of the Volmer-Weber theory is that a critical cluster that gain one more atom is supposed to grow to macroscopic size while in reality there is still a probability for it to decay. Backer and Doring [13, 14, 15] proposed a different expression for the equilibrium cluster distribution $N^{equ}(r)$ that takes into account that possibility, thus obtaining the following steady state nucleation rate

$$I^{ss} = s_c \cdot k \cdot N_0 \cdot \underbrace{\frac{1}{i_c} \cdot (\frac{\Delta G_c}{3\pi k_B T})}_{\Gamma_Z} \cdot exp(-\frac{\Delta G_c}{k_B T}) = I^{equ} \cdot \Gamma_Z \tag{1.6}$$

where i_c is the number of atoms in the critical clusters and Γ_Z is the so-called Zeldovich factor, which has been found to be usually between 1/100 and 1/10. The weak dependence of Γ_Z on temperature, especially if compared with the exponential term, makes Eq. 1.6 essentially equal to Eq. 1.5 for most practical purposes, but in the case of Eq. 1.6 the kinetic problem has been correctly treated.

Up to the Volmer-Weber model, all the results were obtained by considering a gas as a amorphous phase. In this case the value of the arrival rate k was calculated from the gases theory. The value of the pre-exponential factor of 1.6 for an amorphous material was calculated by Turnbull and Fisher [16], who completed the classical nucleation theory. They distinguished between a diffusion-limited crystallization and a collision-limited crystallization. The former is the case of phase change materials, and the expression for k is

$$k = \frac{6D}{\lambda^2} \tag{1.7}$$

where λ is the average interatomic distance. By using the Stokes-Einstein equation that relates the diffusion coefficient D and the viscosity η it is possible to write

$$\eta D = \frac{k_B T}{3\pi\lambda}, \tag{1.8}$$

and the nucleation rate I^{ss} for the diffusion-limited model can be expressed as a function of η:

$$I^{ss} = s_c \cdot \frac{2k_B T}{\eta\pi\lambda^3} \cdot N_0 \cdot \Gamma_Z \cdot exp(-\frac{\Delta G_c}{k_B T}) \tag{1.9}$$

The pre-exponential factors of I^{ss} can be estimated in both cases by substituting reasonable values for N_0, s_c T and Γ_Z. They result to be $\frac{10^{36}}{\eta}$ for the diffusion-limited case and 10^{39} for the collision-limited case, with an uncertainty of two to four orders of magnitude. This has not a great influence on the overall expression due to the strong dependence of I^{ss} on ΔG_c and σ, both present in the exponential term. The diffusion-limited I^{ss} tends to zero near T_m and T_g and exhibit a maximum for a temperature intermediate between them, as it happens for phase change materials. This is not the case for collision-limited kinetics, where I^{ss} increases continuously as the temperature decreases below T_m .

Heterogeneous Nucleation

The model for heterogeneous nucleation was developed by Volmer and Weber [18]. It is based on the Gibbs' model already described for the homogeneous nucleation, but considering a flat substrate that act as a heterogeneous nucleation site.

In Figure 1.8 is reported the model for heterogeneous nucleation, taken from Chapter 7 of Reference [4]. In this model the crystalline cluster nucleates on the heterogeneous substrate as a spherical cap of radius r. This spherical cap can be considered as the exposed part of a complete sphere of radius r, so that the fraction of the exposed volume can be calculated as a function of the wetting angle θ

$$f(\theta) = \frac{(2 + cos\theta)(1 - cos\theta)^2}{4}. \tag{1.10}$$

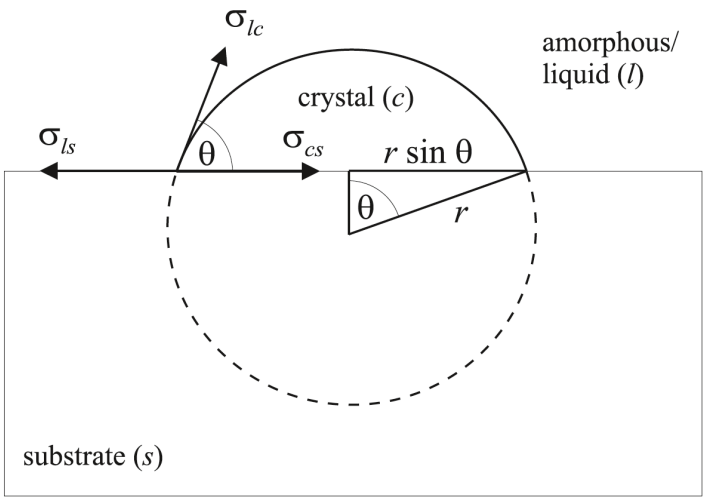

Figure 1.8: Model for the heterogeneous nucleation taken from Chapter 7 of Reference [4]. The crystalline cluster is a spherical cap which correspond to the exposed part of a sphere of radius r. In the schematic picture are also reported the wetting angle θ and the crystal-substrate, amorphous-substrate and amorphous-crystal interfacial energies (respectively σ_{cs}, σ_{ls} and σ_{lc}).

It was demonstrated by Volmer and Weber that the free energy for cluster formation $\Delta G_{cluster}$ is reduced if

$$\sigma_{cs} - \sigma_{ls} < \sigma_{lc} \tag{1.11}$$

where σ_{cs}, σ_{ls} and σ_{lc} are the crystal-substrate, parental phase-substrate and parental phase-crystal interfacial energies, respectively. In this case, $\Delta G_{cluster}$ for the heterogeneous nucleation is the $\Delta G_{cluster}$ for the homogeneous nucleation multiplied by the factor $f(\theta)$

$$\Delta G_c^{het} = \Delta G_c^{het} \cdot f(\theta). \tag{1.12}$$

The critical radius r_c remains unchanged, and the whole model for homogeneous nucleation is still valid with the only difference of a lower $\Delta G_{cluster}$. However, the parent phase atoms that can act as nucleation sites are not all the atoms in the parent phase but only those interfaced with the substrate, so their number is decreased. If ϵ is the fraction of parent phase atoms that are in contact with the substrate on the total, the ratio of homogeneous and heterogeneous

nucleation rates is

$$\frac{I^{ss,het}}{I^{ss,hom}} = \epsilon \cdot exp(\frac{\Delta G_c}{k_B T} \cdot [1 - f(\theta)]). \tag{1.13}$$

The heterogeneous nucleation rates have been observed to be much higher than the homogeneous ones, implying that θ must be small.

1.3.4 Growth

When a cluster has reached its critical radius it grows to a macroscopic size. This growth is interface-controlled by the addition of new parental phase atoms in the crystalline cluster [13]. The crystal growth velocity is

$$u = \gamma_s \cdot \lambda \cdot k \cdot [1 - exp(-\frac{\Delta G_{lc,atom}(T)}{k_B T})](T < T_m) \tag{1.14}$$

where $0 < \gamma_s < 1$ is the fraction of sites on the interface where a new parent phase atom can be incorporated, λ is the average interatomic distance, $\Delta G_{lc,atom}(T)$ is the Gibbs free energy between the parent phase and the crystalline phase per atom and k has the same meaning and value as for nucleation. For diffusion-limited kinetics, by substituting k as in Section 1.3.3 and using Eq. 1.8 the crystal growth velocity is

$$u = \gamma_s \cdot \frac{2k_B T}{\eta \pi \lambda^2} \cdot [1 - exp(-\frac{\Delta G_{lc,atom}(T)}{k_B T})](T < T_m) \tag{1.15}$$

As for the nucleation rate, the growth velocity u is zero at $T =$T$_m$, negligible at $T =$ T$_g$ and exhibit a maximum in the temperature range between T$_g$ and T$_m$ .The growth rate maximum is usually located at a higher temperature than the nucleation rate maximum.

1.3.5 Johnson - Mehl - Avrami - Kolmogorov (JMAK) formalism

The so-called JMAK (Johnson-Mehl-Avrami-Kolmogorov) model is an alternative to the classical crystallization theory for describing the crystallization kinetics. While the classical nucleation theory allows the calculation of the cluster nucleation and growth rates, as well as their size distribution, the JMAK model

is a mean to calculate the crystalline fraction in terms of crystal nucleation and growth rates.

The model is based on the JMAK equation, which gives the volume fraction of the transformed material as a function of time ($x(t)$) under isothermal annealing conditions:

$$x(t) = 1 - exp\left(-kt^n\right) \tag{1.16}$$

where t is time, k is an effective rate constant and n is the so called Avrami coefficient. The value of k depends on temperature through the Arrhenius equation

$$k(T) = \nu exp\left(\frac{E_A}{-k_B T}\right) \tag{1.17}$$

where ν is the frequency factor, E_A is the activation energy, T is the absolute temperature and k_B is the Boltzmann constant. The value of $ln\left[-ln\left(1-x\right)\right]$ plotted as a function ln(t) is the so-called JMAK plot. In literature, the JMAK theory has been often used to interpret isothermal annealing of PC materials, and the activation energy E_A has been usually determined through Kissinger analysis [19]. The Kissinger method is based on the measurement of the variation of the crystallization temperature T_x for different heating rates dT/dt, which are related to the activation energy through the equation

$$ln\left(\frac{1}{T_x^2}\cdot\frac{dT}{dt}\right) = -\frac{E_A}{k_B T_x} + C \tag{1.18}$$

so that it is possible to deduce the activation energy as the slope of the linear interpolation of the plot of $ln\left(\frac{1}{T_x^2}\cdot\frac{dT}{dt}\right)$ versus $\frac{1}{k_B T_x}$. However, even if this method is widely used, it is based on the assumption of an Arrhenius-like temperature dependence for crystallization. This is not the case when the crystallization is controlled by the nucleation rate, which is non-Arrhenius [20].

Eq. 1.16 can be applied under the conditions that nucleation occurs randomly and uniformly with a time independent rate and that growth is interfaced-controlled and with a size independent rate. The use of Eq. 1.16 should not be legitimate without fulfilling those conditions, which are usually not verified for GST, and as a consequence the values reported in literature for E_A and ν differ significantly one from each other. However, due to its simplicity the Kissinger method will be used in Chapter 3 and 4 of this thesis for quantitative comparisons between materials.

Required property of PC material	Specification
High-speed phase transition	Induced by nanosecond laser or voltage pulse
Long thermal stability of amorphous state	At least several decades at room temperature
Large optical change between the two states	Considerable difference in refractive index or absorption coefficient
Large resistance change between the states	Natural consequence of the phase transformation
Large cycle number of reversible transitions	More than 100,000 cycles with stable composition
High chemical stability	High water-resistivity

Table 1.1: Properties that characterize PC materials [7].

1.4 Phase change materials

Materials to be used in PCM should meet several strict requirements. They should possess the properties of a fast crystallization, a large optical and electrical contrast between the amorphous and crystalline phases, a melting temperature sufficiently low to limit the electric power needed for amorphization and a high stability of the amorphous phase to grant good retention performances. Moreover, those properties must not decay with cycling between the states. The crucial properties of phase-change alloys are summarized in Table 1.1, taken from Reference [7].

1.4.1 Ge:Sb:Te compounds

As already described in Section 1.1, from the material point of view the greatest discovery for phase change memories was done in the 1980s by Yamada and his coworkers. They identified the materials belonging to the $GeTe - Sb_2Te_3$ pseudo-binary line in the Ge:Sb:Te ternary phase diagram as the ones with the best properties. In Figure 1.9 the Ge:Sb:Te phase diagram is represented, with several PC materials and the $GeTe - Sb_2Te_3$ pseudo-binary line. In particular, the $Ge_2Sb_2Te_5$ compound (simply called GST) became a standard for optical storage devices that have been developed during the 1990s. It was chosen for its high retention time, fast transformation speed and large optical contrast between crystalline and amorphous phase. Thus, GST was chosen as the active

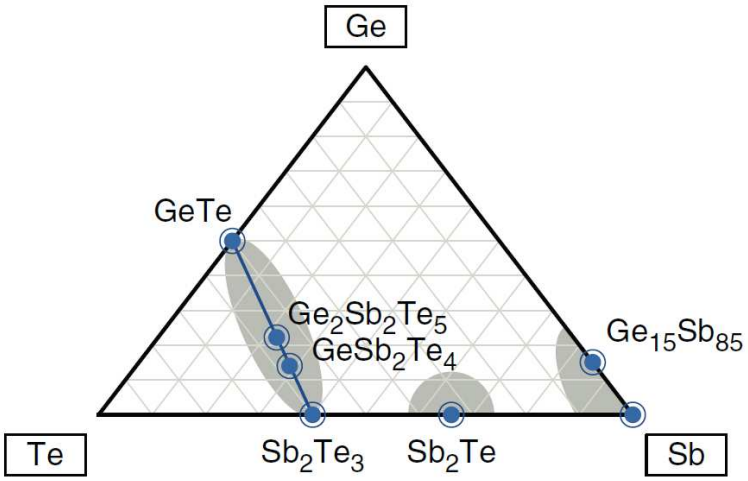

Figure 1.9: PC materials reported on the ternary Ge:Sb:Te phase diagram, with the $GeTe-Sb_2Te_3$ pseudo-binary line put in evidence (taken from Ref. [8]).

material to be first employed in PCM due to the wide number of studies already performed on it. However, the study of alternative phase change materials that can offer better properties for PCM is very active and rich, both for its scientific interest and the industrial development. For example, in 2011 Cheng and coworkers studied compounds along the $GeTe-Sb$ line. They demonstrated that Ge-rich $Ge_2Sb_1Te_2$ (the so-called *golden composition*) can offer better properties than GST in terms of crystallization speed and data retention [21]. It has been also recently shown that GeTe compound can be a good candidate for embedded PCM due to its higher crystallization temperature and better retention time compared to GST [22]. The main properties of $Ge_2Sb_2Te_5$ and GeTe are compared in Table1.2

Phase change materials that belong to the $GeTe - Sb_2Te_3$ pseudo-binary line are characterized by a few typical structural motifs indicating a common bonding mechanism that could account for their properties. In general, ternary compounds exhibit a rocksalt-like structure in their crystalline phase where the anion sublattice is occupied by atoms of Te and the cation sublattice is randomly occupied by Ge, Sb or vacancies [7].

The constant feature for all crystalline Ge:Sb:Te phase change alloys is the presence of a more or less distorted octahedral-like coordination resulting from a Peierls distortion. In addition, some materials are characterized by a consid-

Properties	$Ge_2Sb_2Te_5$	GeTe
Crystallization temperature T_x [22]	145 °C	185°C
Activation energy E_A (thin films) [23]	2.3 eV	2.0 eV
Activation energy E_A (devices) [24]	3.13 eV	3.2 eV
Crystalline phase [25]	Rocksalt cubic (with vacancies)	Rhombohedral
Lattice parameters [25]	a = 6.01 Å	a = 4.16 Å, c = 10.69 Å
Density (amorphous phase) [25]	5.86 g/cm^3	5.60 g/cm^3
Density (crystalline phase) [25]	6.13 g/cm^3	6.06 g/cm^3

Table 1.2: Comparison between the main properties of $Ge_2Sb_2Te_5$ (GST) and GeTe.

erable number of vacancies (for example, 20% for $Ge_2Sb_2Te_5$ [25] and 25% for $Ge_1Sb_2Te_4$ [7]). The amorphous phase differs considerably from the crystalline one by the absence of a long range order, but a local order still exists in the amorphous structure of PC materials. It has been investigated both experimentally and through ab-initio calculations.

In the following section the amorphous and crystalline structure of GeTe and GST compounds will be described.

1.4.2 Structure of crystalline and amorphous $Ge_2Sb_2Te_5$ and GeTe

Both GeTe and GST are characterized by two different crystalline phases.When amorphous $Ge_2Sb_2Te_5$ (GST) is heated, it crystallizes at around 150°C in a metastable crystalline phase with a fcc rocksalt structure. The crystalline structure of $Ge_2Sb_2Te_5$ (GST) has been described in 2000 by Yamada and coworkers [26] as it is shown in Figure 1.10. The structure is a NaCl rocksalt structure with an octahedral-like atomic arrangement, where the Te atoms occupy one lattice site and the Ge and Sb atoms randomly occupy the second lattice site. The Te sites are all fully occupied, while the Ge/Sb sublattice is characterized by the presence of around a 20% of vacancies so that the structure is characterized by local distortions. If cubic GST is heated above around 200°C it transforms in an hexagonal phase [6].

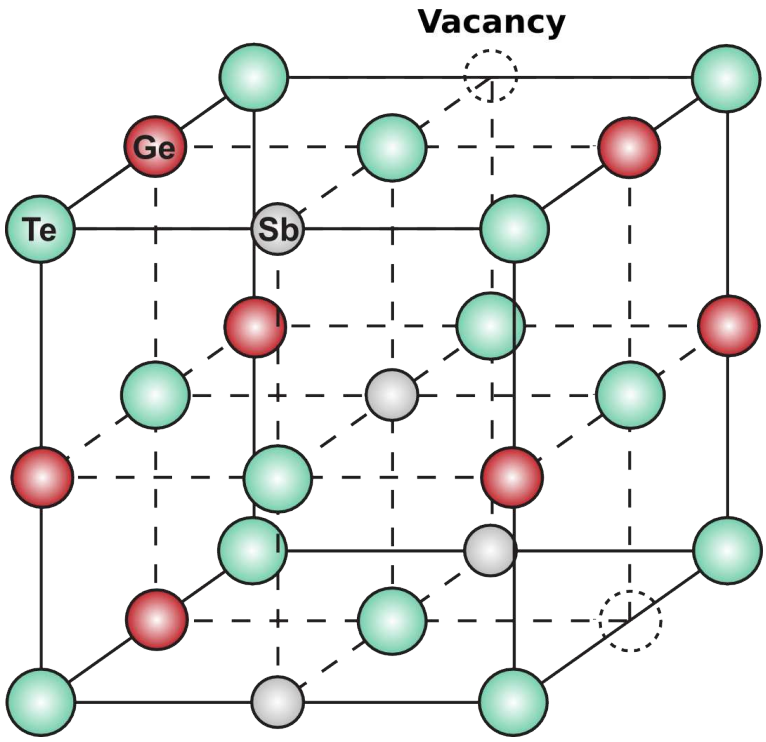

Figure 1.10: Structure of GST in its crystalline metastable phase. One sublattice is occupied by Te atoms (light blue) while the other is randomly occupied by Ge or Sb atoms (dark blue) or vacancies (around 20%). The cubic lattice parameter is 6.03 Å [26].

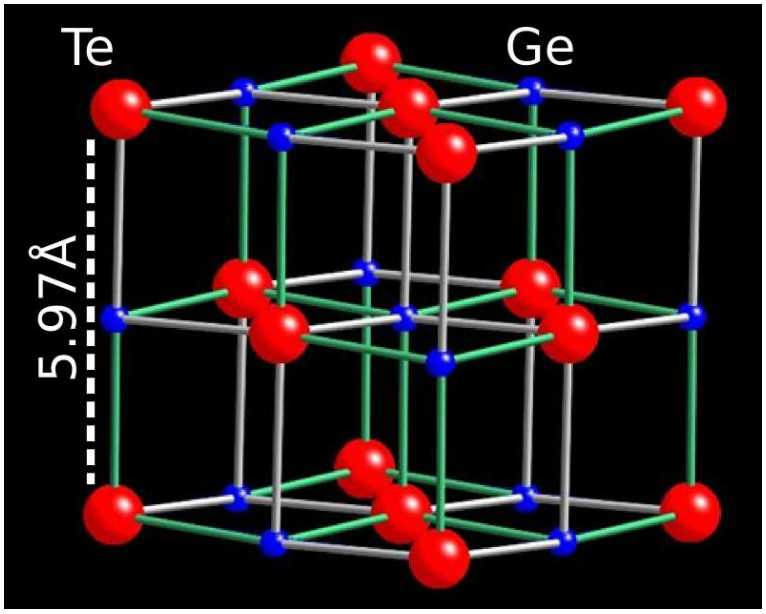

Figure 1.11: Structure of crystalline GeTe in its rhombohedral phase. The structure can be described as a rocksalt-like structure, distorted by a relative shift of the sublattices along the [111] direction. It is characterized by long (3.127 Å) and short (2.87 Å) Ge-Te bonds shown respectively in white and green.

Amorphous GeTe crystallizes at 180°C into a rhombohedral phase (space group R3m) that is the stable crystalline phase at room temperature [25]. Above around 430°C this phase transforms into a cubic fcc rocksalt structure (space group Fm3m) where Ge occupies one sublattice and Te the other sublattice. The low temperature rhombohedral phase can be described as a slightly distorted rocksalt structure obtained by a relative shift of both sublattices along the [111] direction, so that each atom form three short bonds and three long bonds with its nearest neighbors. The structure is represented in In Fig.1.10, and it can be easily observed that each atom is in a distorted octahedral environment.

The structure of the amorphous GeTe and GST phases have been widely studied in literature [27, 28] but in the following the subject will be treated only briefly. The short and medium range order has been studied in literature mainly through X-ray scattering and measurement of the pair distribution function method (see Chapter 2) that allow to determine the local atomic environments. It has been observed that a local chemical ordering takes place in the amorphous phase by an alternation of Te and Ge(or Sb) atoms which is a

precursor of the order in the crystalline phase. The first Te-Ge distance has been confirmed to be around 2.6Å, but the Ge coordination number is still debated. Some studies through extended X-ray absorption fine structure (EXAFS) and X-ray absorption near-edge spectroscopy (XANES) conclude that germanium is tetrahedrally coordinated [29]. They were further supported by X-ray fluorescence and Raman scattering experiments [30, 31, 32]. However, further studies with X-ray diffraction data and reverse Monte Carlo simulations indicate for GST bond angles around 90°and no homopolar bonds, while only for GeTe the presence of both homopolar Ge-Ge bond and a deviation in bond angles from 90°was observed [27, 28, 33]. In conclusion, the chemical alternation of Te and Ge(Sb) atoms is confirmed and germanium is found to coexist in both tetrahedral and distorted octahedral environments.

For both GeTe and GST, the density of the crystalline phase is higher than the one of the amorphous phase, so the volume is reduced after crystallization, and the density change for GeTe is relatively higher than for GST. Amorphous GeTe has a density of 5.60 g/cm^3, while for the crystalline GeTe it is 6.06 g/cm^3. The density of amorphous GST is 5.86 g/cm^3 and the one of crystalline GST is 6.13 g/cm^3[25].

1.5 Goals and outline

For PCM to be competitive it is fundamental to develop memory devices with good retention properties, high cyclability, high transformation speed, low power consumption and most of all high integration density, meaning cells of reduced dimensions. Those requirements can be fulfilled both through device and layout architecture improvements and through an optimization of the used PC materials. As an example, in the field of embedded memories for automotive systems the operating temperatures are close to the crystallization temperature of $Ge_2Sb_2Te_5$ (GST), so this material is unable to fulfill the requirements on data retention and alternative materials must be used. Good PC materials candidates should have the properties listed in Table 1.1 and they must be able to maintain these properties even when dimensions are reduced and the material

gets more and more confined in the cell structure.

In the last years, possible alternatives to GST have been found in using different compounds, as GeTe, or in doping GST with N. The fast transition speed and good retention properties of GeTe makes it suitable for embedded applications. Right before the beginning of this thesis work in has been shown that C and N doping improves drastically the data retention of GeTe and lowers the current needed for amorphization. However, up to now the effects of doping on the structure of GeTe are still not clear, in particular on the stabilizing effect on the amorphous phase. Moreover, the effect of confinement on PC materials is still an open subject even for standard GST. It is also important to underline that in a memory device the active layer is always in contact with different interface materials that can eventually influence its properties, especially for reduced dimensions.

For those reasons, the aim of this thesis is to study PC materials properties in three directions. First, the effect of C and N doping on the structure of amorphous GeTe has been investigated and some interesting results on the stability of the amorphous phase have been obtained. Second, the effect of three-dimensional confinement has been studied on very small nanoclusters of GST, deposited by sputtering with a new technique and characterized through X-Ray diffraction. Third, the effect on the crystallization temperature of interfacing GST and GeTe thin films with different materials has been studied through reflectivity and X-ray diffraction measurements.

In Chapter 2 the study on the effect of doping on GeTe will be discussed. From X-ray scattering experiments performed at the synchrotron SOLEIL (Saclay) on amorphous powders of GeTe, C-doped GeTe and N-doped GeTe pair distribution function (PDF) will be obtained. The PDF is proportional to the probability of finding two atoms at a certain distance. This quantity provides useful information on the local structure of a material, which is the only exploitable one for the amorphous phase. The experimental results will be interpreted and discussed thanks to ab-initio simulations.

The effect of confinement on GST is the subject of Chapter 3. The deposition of nano-sized clusters of GST with an average size of around 5.7 nm

($\pm$ 1 nm) in a matrix of Al_2O_3 will be described. At the moment, those clusters are the smallest GST clusters ever deposited by sputtering, and with the narrowest size distribution. X-Ray diffraction measurement performed at the ESRF synchrotron (Grenoble) in order to observe the crystallization of clusters will be be reported and the discussions and conclusions will be focused on the interpretation of the observed crystallization temperature.

In Chapter 4, the effect of interface layers on the crystallization of phase change material will be investigated. This subject has not been largely treated in literature up to know, so it is a new and very interesting field of research. First, the measurements of the crystallization temperature of GST and GeTe thin films embedded in three different materials (Ta, TiN and SiO_2) through reflectivity measurements will be reported. In the following, the study will be focused on GeTe only and structure properties of the crystalline phase such as the grain size and texture will be investigated through X-Ray diffraction analysis. Some hypothesis will be presented on the nature of crystallization in presence of different interfaces to support the conclusions on the obtained results.

Chapter 2

Effect of doping on the structure of amorphous GeTe

2.1 State of the art on doping effects in phase change materials

As already stated in the first Chapter, PCM must fulfill many requirements in order to be competitive on the market. Those requirements include having a good data retention and a low reset current, so that the data are preserved at least 10 years at room temperature and the power required for programming the cell in the RESET state is low. The data retention depends on the time required for the metastable amorphous phase to crystallize, so it can be improved by employing PC materials with a more stable amorphous phase and a higher crystallization temperature T_x . The RESET current depends on the resistivity of the crystalline phase because the reamorphization process requires to heat the material by Joule effect through the programming current pulse, and a more resistive material can be heated by lower current pulses. These goals can be achieved by exploring new Ge-Sb-Te compound, but another possibility to increase both the resistivity of the crystalline phase and the retention in the amorphous state is opened by doping [1]. The effect of introducing a dopant element in PC materials has been widely investigated during the last two decades. The most studied dopant is Nitrogen (N), but many other doping elements have been studied lately, including Boron (B), Silicon Dioxide (SiO_2) and, more recently, Carbon (C).

The effect of N doping has been studied since late 90s, when it was observed that cyclability for optical disks was improved by adding nitrogen into a Ge-Sb-Te recording layer [34, 35]. When phase change electrical memories started to be intensively studied, after year 2000, nitrogen-doped GST (NGST) gained interest as a PCM device material due to its high crystallization temperature, high retention time and high resistivity [36, 37]. NGST has been successfully integrated into PCM devices [38, 39] and even in memory arrays [40]. The literature about N-doped GST is quite vast but it will not be treated further here, apart from a results on the structure of NGST reported in section 2.6.

[1] The term *doping* is conventionally used in this context to indicate the addition to the PC material of elements in a concentration of several percents.

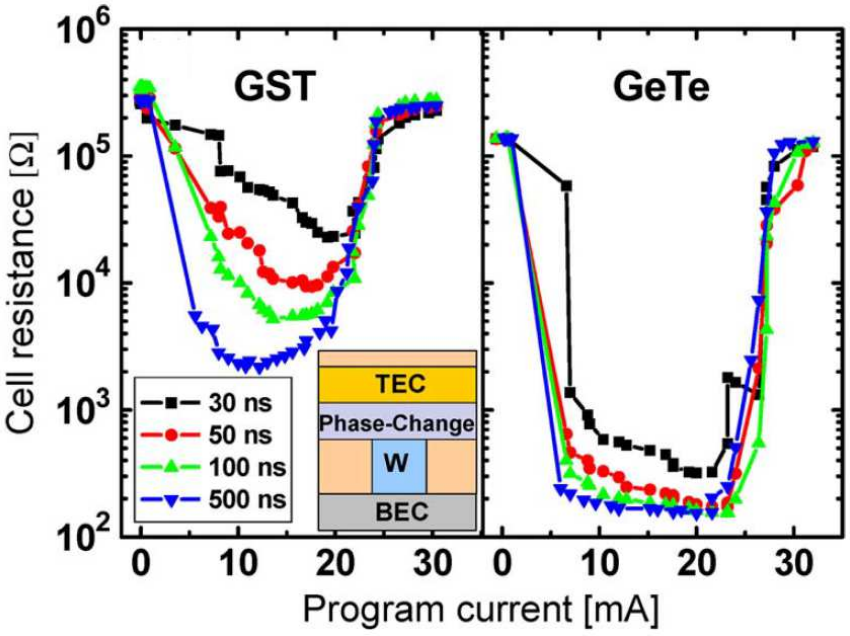

Figure 2.1: Low field cell resistance as a function of progam current for GST and GeTe cells for various programming pulse times [24]. It can be noted that the SET operation for the GeTe cell is faster and the difference in the resistance of the amorphous and crystalline phases is higher.

As already stated in section 1.4, during the last years the GeTe compound has been identified as a possible good candidate for embedded PCM due to its higher crystallization temperature and better retention time than undoped GST [22]. Moreover, GeTe PCM cells are characterized by a rapid SET operation compared to GST cells (see Fig.2.1) and have demonstrated high cyclability [24]. However, the required RESET current is the same for GST and GeTe. In order to increase the resistivity of the crystalline cell and improve further the properties of good retention and high T_x , N-doped GeTe has been studied. N-doped GeTe (hereafter called GeTeN) with various percentages of N has been successfully integrated into memory devices, with beneficial effects compared to standard GeTe such as an even faster crystallization and a higher retention time. The best performances were obtained for a N concentration of 2% [41], as shown in Fig.2.2. An increase of the resistance of the crystalline phase for GeTeN (N=8.4%) compared to undoped GeTe and an increase of the crystallization temperature for GeTeN (N=9.81%) have also been observed [42, 43].

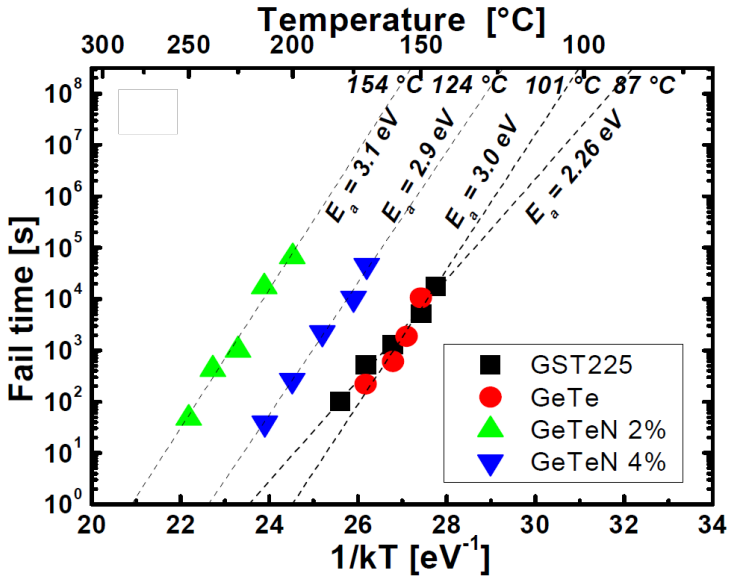

Figure 2.2: Calculation of the activation energy E_A by interpolation of the fail times as a function of $1/kT$. In order to obtain the fail time, a PCM cell is written in the RESET state and the fail time is defined as the time at which the resistance of the cell is reduced by one half.

More recently, it has been shown that also C-doping can have a great impact on the performances of GeTe. GeTeC devices with doping percentages of 4 and 10% showed an improved data retention in temperature compared to undoped GeTe, indicating that the amorphous phase stability is improved by C-doping [44]. As can be seen in Fig.2.3 and Table 2.1 [45], the crystallization temperature of GeTeC is much higher than that of undoped GeTe and the effect of C-doping is even stronger than the one of N-doping. For example, for GeTeC (C=10%) $T_x \approx 325$°C , to be compared with $T_x \approx 275$°C of GeTeN (N=10%). Moreover, the retention time, the activation energy E_A and the crystal resistivity increase with doping while the reset current decreases, as shown in Fig.2.4.

Doped phase change materials are thus promising candidates in order to fulfill some requirements on PCM as the high data retention at elevated temperatures or the low reset current. However, even if their good performances have been demonstrated, a deeper understanding of the effects of doping on the structure of GST and GeTe was lacking. Clarifying this subject can lead to a better material engineering. The open questions, at least when this study has been performed, include the impact of dopants on the amorphous structure and their

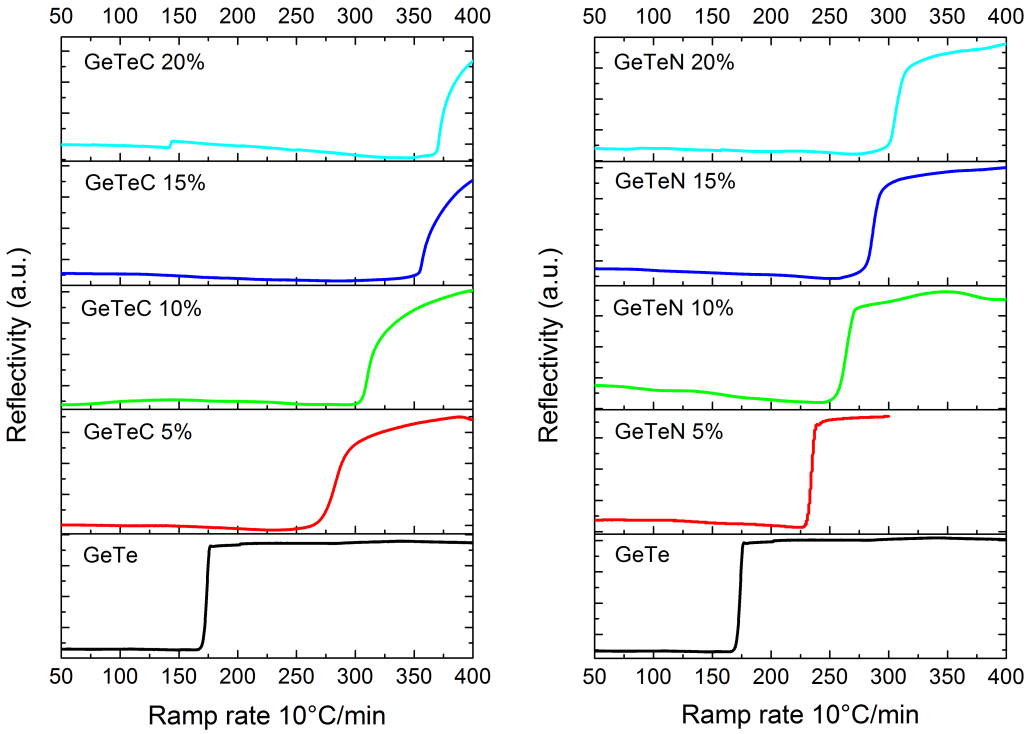

Figure 2.3: Reflectivity measurements of C and N doped GeTe films (150 nm thick) [45]. In both cases T_x increases with increasing doping concentration and the effect is stronger for C doping.

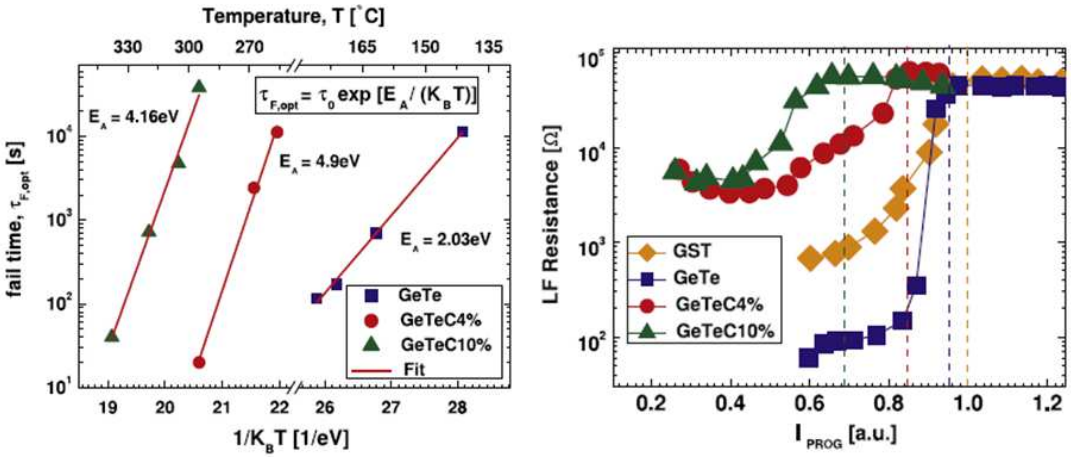

Figure 2.4: Activation energy (left) calculated for undoped and C-doped GeTe and low electric field resistance as a function of the programming current (right) for a GST, undoped GeTe and C-doped GeTe cell [44]. The activation energy increases and the RESET current decreases with doping.

Material	T_x [°C]
GeTe	175
GeTeC 5%	280
GeTeC 10%	320
GeTeC 15%	365
GeTeC 20%	380
GeTeN 5%	235
GeTeN 10%	265
GeTeN 15%	290
GeTeN 20%	310

Table 2.1: Crystallization temperatures T_x of C and N doped GeTe films (150 nm thick), taken as the midpoint of the rising steps of the reflectivity curves reported in Fig.2.3 [45].

location in the crystalline structure. This is essential for understanding if the structure of the materials remains stable after many cycles of crystallization and reamorphization.

In the following, experimental results obtained through X-ray scattering on the structure of amorphous C-doped and N-doped GeTe will be presented. Ab initio simulations have also been performed in order to have a better understanding of the experimental results. The results presented in this chapter have been published in Ref. [46].

2.2 Theory of the Pair Distribution Function (PDF) g(r)

The amorphous phase is characterized by the absence of the long-range periodic order that can be found in the crystal phase, but a short and medium-range order is still present (see section 1.4.2). The determination of the Pair Distribution Function (PDF) g(r) allows to have an insight on these local orders, describing the correlations between pairs of atoms. In the following, the theory at the basis of the PDF determination will be described [47, 48].

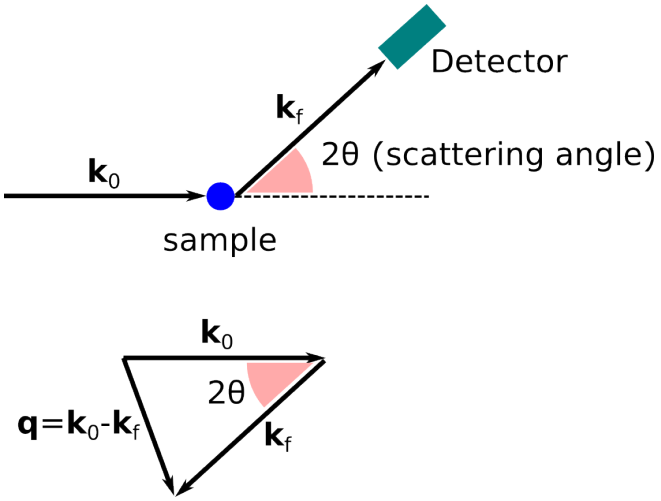

Figure 2.5: Schematic representation of an X-ray incident beam scattered by a point-like sample. The incident wavevector is $\mathbf{k}_0$, the scattered wavevector is $\mathbf{k}_f$ and the momentum transfer is $\mathbf{Q} = \mathbf{k}_0 - \mathbf{k}_f$.

Let us consider a X-ray incident beam on a point-like sample containing N atoms as depicted in Fig.2.5. The incident beam is characterized by a wavevector $\mathbf{k}_0$ of modulus $2\pi/\lambda$ and an energy E_0. The scattered beam is characterized by a wavevector $\mathbf{k}_f$ and an energy E_f. The momentum transfer is $\mathbf{Q} = \mathbf{k}_0 - \mathbf{k}_f$ and the energy transfer is $\hbar\omega = E_0 - E_f$. The double differential cross-section is defined as the number of photons (or neutrons) scattered per unit of time into the solid angle interval $[\Omega, \Omega + d\Omega]$ and into the energy interval $[E_f, E_f + dE_f]$. For X-Ray scattering, the incident beam energy is of the order of several keV so that the maximum energy transfered between the incident photon and the sample is negligible compared to the incident energy and $\mathbf{k}_0 \approx \mathbf{k}_f$. As a consequence, the modulus of Q is simply $4\pi sin\theta/\lambda$, with 2θ being the scattering angle, as shown in Fig.2.5. In scattering experiments no analysis of the out-coming photon energy is performed, so that all the photons in the solid angle $d\Omega$ are measured whatever their energy, resulting in a cross-section

$$\frac{d\sigma}{d\Omega} = \int_{-\infty}^{E_0} \frac{d^2\sigma}{d\Omega dE_f} \hbar d\omega \tag{2.1}$$

The general expression of $\frac{d\sigma}{d\Omega}$ is

$$\frac{d\sigma}{d\Omega} = \left\langle \sum_{i,j}^{N} f_i(\mathbf{Q}) f_j(\mathbf{Q}) e^{i\mathbf{Q}\cdot\mathbf{r}_{ij}} \right\rangle \tag{2.2}$$

where $f_i(\mathbf{Q})$ is the atomic form factor of atom i at the position $\mathbf{r}_i$ and $\mathbf{r}_{ij} = \mathbf{r}_j - \mathbf{r}_i$. In the equation, i can be equal to j. The notation $\langle\rangle$ in Eq. 2.2 denotes an average on all possible positions of the scattering centers due to thermal agitation. In order to understand the meaning of Eq. 2.2, let us first consider the case of a monoatomic sample where all atoms have the same form factor $f(\mathbf{Q})$, so that

$$\frac{1}{N}\frac{d\sigma}{d\Omega} = f^2(\mathbf{Q}) \left\langle \frac{1}{N} \sum_{i,j}^{N} e^{i\mathbf{Q}\cdot\mathbf{r}_{ij}} \right\rangle = f^2(\mathbf{Q}) \cdot S(\mathbf{Q}) \tag{2.3}$$

where the so-called *structure factor* $S(\mathbf{Q})$ is defined as

$$S(\mathbf{Q}) = \left\langle \frac{1}{N} \sum_{i,j}^{N} e^{i\mathbf{Q}\cdot\mathbf{r}_{ij}} \right\rangle \tag{2.4}$$

where i can be equal to j. The structure factor $S(\mathbf{Q})$ is a dimensionless quantity and tends to 1 when $\mathbf{Q}$ tends to ∞. In a crystal, due to periodicity, $S(\mathbf{Q})$ consists of peaks for $\mathbf{Q}$ vectors belonging to the reciprocal lattice. In a disordered system such as a liquid or a glass, the scattering is isotropic and the structure factor only depends on the modulus of $\mathbf{Q}$. It exhibits broad oscillations as it will be seen on Fig.2.6. In the isotropic case, $S(Q)$ can be written as

$$S(Q) = \left\langle \frac{1}{N} \sum_{i,j}^{N} \frac{sin(Qr_{ij})}{Qr_{ij}} \right\rangle = 1 + \frac{1}{N} \sum_{i \neq j}^{N} \frac{sin(Qr_{ij})}{Qr_{ij}} \tag{2.5}$$

where r_{ij} is the interatomic distance between atoms i and j. Considering that also $f(\mathbf{Q})$ depends only on the modulus of $\mathbf{Q}$, Eq. 2.4 can be written as

$$\frac{1}{N}\frac{d\sigma}{d\Omega} = f^2(Q) \cdot S(Q) \tag{2.6}$$

which can be rewritten as

$$\frac{1}{N}\frac{d\sigma}{d\Omega} = F(Q) + f^2(Q) \tag{2.7}$$

where $F(Q) = f^2(Q)[S(Q) - 1]$ is the so-called *interference function*. It is then possible to describe the structure of the sample in the real space by means of the *pair distribution function* $g(r)$, which can be obtained by Fourier transformation from the structure factor $S(Q)$ as

$$g(r) = 1 + \frac{1}{2\pi^2 r \rho_0} \int_0^{\infty} Q[S(Q) - 1] sin(Qr)\, dQ \tag{2.8}$$

where $\rho_0 = \frac{N}{V}$ is the atomic number density of the sample. The pair distribution function $g(r)$ tends to zero for $r \to 0$ and tends to 1 for $r \to \infty$. It can be demonstrated that

$$g(r) = \frac{1}{N} \frac{\left\langle \sum_{i \neq j}^{N} \delta(r - r_{ij}) \right\rangle}{4\pi r^2 \rho_0} \tag{2.9}$$

In Eq. 2.9 the meaning of the function $g(r)$ is clearly stated. It is proportional to the probability of finding two atoms at a distance r. It should be also underlined that $4\pi r^2 \rho_0 \cdot g(r)\, dr$ is the average number of atoms between r and $r + dr$. It is possible to obtain the structure factor $S(Q)$ starting from $g(r)$ by means of an inverse Fourier transformation

$$S(Q) - 1 = \frac{4\pi\rho_0}{Q} \int_0^\infty r\,[g(r) - 1]\, sin(Qr)\, dr \tag{2.10}$$

In a polyatomic system constituted of n distinct chemical species denoted α, β, etc. it is necessary to define *partial pair distribution functions* $g_{\alpha\beta}(r)$ and *partial structure factors* $S_{\alpha\beta}(Q)$. In the formalism developed by Faber and Ziman [49] one defines

$$g_{\alpha\beta}(r) = \frac{1}{N c_\alpha c_\beta} \frac{\left\langle \sum_{i_\alpha \neq j_\beta} \delta\left(r - r_{i_\alpha j_\beta}\right) \right\rangle}{4\pi r^2 \rho_0} \tag{2.11}$$

$$S_{\alpha\beta}(Q) = 1 + \frac{1}{N c_\alpha c_\beta} \left\langle \sum_{i_\alpha \neq j_\beta} \frac{sin\left(Q r_{i_\alpha j_\beta}\right)}{Q r_{i_\alpha j_\beta}} \right\rangle \tag{2.12}$$

where c_α and c_β are the concentration of atoms for the species α and β so that $\sum_\alpha^n c_\alpha = 1$, N is the total number of atoms, i_α is an atom of species α, i_β is an atom of species β and $\rho_0 = \frac{N}{V}$ as in the monoatomic case. The sum on i_α runs from 1 to $N_\alpha = c_\alpha N$ and the sum on j_β runs from 1 to $N_\beta = c_\beta N$. The partial pair distribution function $g_{\alpha\beta}(r)$ is proportional to the probability of finding an atom of species α at a distance r from one atom of species β. The partial structure factor and the partial pair distribution function are related to each other though the relations

$$S_{\alpha\beta}(Q) = 1 + \frac{4\pi\rho_0}{Q} \int_0^\infty r\,[g_{\alpha\beta}(r) - 1]\, sin(Qr)\, dr \tag{2.13}$$

$$g_{\alpha\beta}(r) = 1 + \frac{1}{2\pi^2 r \rho_0} \int_0^\infty Q\,[S_{\alpha\beta}(Q) - 1]\, sin(Qr)\, dQ \tag{2.14}$$

It is possible to generalize Eq. 2.7 obtained in the monoatomic case as

$$\begin{aligned}\frac{1}{N}\frac{d\sigma}{d\Omega} &= \sum_{\alpha,\beta} c_\alpha c_\beta f_\alpha(Q) f_\beta(Q) S_{\alpha\beta}(Q) - \sum_\alpha c_\alpha c_\beta f_\alpha(Q) f_\beta(Q) + \sum_\alpha c_\alpha f_\alpha^2(Q) \\ &= \sum_{\alpha,\beta} c_\alpha c_\beta f_\alpha(Q) f_\beta(Q) S_{\alpha\beta}(Q) + \sum_\alpha c_\alpha f_\alpha^2(Q) - \left[\sum_\alpha c_\alpha f_\alpha(Q)\right]^2\end{aligned} \tag{2.15}$$

By defining

$$\left\langle f^2 \right\rangle = \sum_\alpha c_\alpha f_\alpha^2(Q)$$

and

$$\langle f \rangle = \sum_\alpha c_\alpha f_\alpha(Q)$$

it is then possible to rewrite the cross-section in Eq. 2.15 as

$$\frac{1}{N}\frac{d\sigma}{d\Omega} = \langle f \rangle^2 S(Q) + \left\langle f^2 \right\rangle - \langle f \rangle^2 \tag{2.16}$$

where the *total structure factor* $S(Q)$ is defined as the weighted sum of the partial structure factors $S_{\alpha\beta}(Q)$

$$S(Q) = \frac{\sum_{\alpha,\beta} c_\alpha c_\beta f_\alpha(Q) f_\beta(Q) S_{\alpha\beta}(Q)}{\left[\sum_\alpha c_\alpha f_\alpha(Q)\right]^2} \tag{2.17}$$

It is then possible to define a *total pair distribution function* $g(r)$ by Fourier transformation in analogy with the monoatomic case (Eq. 2.8)

$$g(r) = 1 + \frac{1}{2\pi^2 r \rho_0} \int_0^\infty Q\left[S(Q) - 1\right] sin(Qr)\, dQ \tag{2.18}$$

However, due to the Q dependence of the atomic form factors, $g(r)$ has no direct physical meaning. In particular it cannot be expressed as a weighted sum of the partial pair distribution functions $g_{\alpha\beta}(r)$.

The total structure factor can be deduced from the measured scattered intensity as a function of the scattering angle 2θ , after several experimental corrections (see appendix A.2.2). It is important to underline that through the experiment it is possible to measure only the total structure factor $S(Q)$ and not the partial ones. The atomic form factors increase with the electron number in the atom (in the limit $Q = 0$ $f_\alpha(0) = Z_\alpha$, the number of electrons). From Eq.

2.17 it can be deduced that, in presence of heavy elements, the contribution of light elements to the total $S(Q)$ will be relatively small, especially if they are in low concentration. This will be the case in the following for all partial terms involving C or N in carbon and nitrogen doped GeTe.

It is indeed possible to compute through ab initio simulations either all the partial pair distribution functions $g_{\alpha\beta}(r)$ or the partial structure factors $S_{\alpha\beta}(Q)$. The latter can then be summed according to Eq. 2.17 to obtain a calculated total structure factor $S_{calc}(Q)$ which can be directly compared to the measured one $S_{exp}(Q)$. In order to compare experiments and calculations in r, the Fourier transform of $S_{calc}(Q)$ and $S_{exp}(Q)$ must be calculated according to Eq. 2.18, leading to $g_{calc}(r)$ and $g_{exp}(r)$ respectively. However, $g_{calc}(r)$ cannot be directly obtained by summing calculated $g_{\alpha\beta}(r)$ as already remarked above.

2.3 Description of the samples

Amorphous thin films 200 nm thick of GeTe, C-doped GeTe containing 9.5 and 16.3 at. % of C and N-doped GeTe containing 4 and 10 at. % of N were deposited by sputtering on a Si (100) substrate as described in appendix B. The Ge and Te concentrations in the films were measured by Rutherford Back Scattering (RBS) and the N and C dopant concentrations by Nuclear Reaction Analysis (NRA). In all the studied samples, there is a small excess of Ge corresponding to $Ge_{52}Te_{48}$, but in the following we will refer to the material as GeTe for simplicity. The atomic number densities deduced from the measured mass densities of all the samples are reported in table 2.2.

To perform the X-ray scattering experiments, the films have been gently scratched in order to obtain a powder and the samples have been prepared by putting about 1 mg of that powder inside a borosilicate glass capillary (700 μm diameter). The packing fraction was of the order of 10%.

Material	Mass density [g/cm^3]	Atomic number density [atoms/Å^3]
GeTe	5.38	0.0327
GeTeC9.5%	5.16	0.0342
GeTeC16.3%	5.12	0.0363
GeTeN4%	5.285	0.03328
GeTeN10%	5.22	0.0347

Table 2.2: Measured mass densities and atomic number densities for $Ge_{52}Te_{48}$, undoped and doped with carbon or nitrogen, expressed in g/cm^3 and atoms/Å^3, respectively. The mass densities have been measured by X-ray reflectivity (XRR).

2.4 X-Ray scattering measurements and results

The X-Ray scattering experiments were performed on beamline CRISTAL at the SOLEIL Synchrotron (Saclay, France) at an incident energy of E=45.4793 keV ($\lambda = 0.4441$Å) in transmission geometry. The transmitted scattered intensity was collected by a 2D image plate detector. A photo and a schematic representation of the experimental setup are shown in appendix A.2.2 in Fig.A.4. The capillaries filled with powder were installed on a small goniometer which was rotating during the measurements in order to average possible non uniformity of the powder in the capillary. For each sample the coefficient of transmission was determined. The empty capillary signal has been measured to be used for subtraction. Considering the distance D $\approx$ 21cm between the sample and the detector, scattering by air is not negligible. Thus, the air signal has been determined by measuring the scattered intensity without sample or capillary.

The intensity as a function of 2θ has been obtained for each sample by integrating the diffracting rings over a vertical sector of the 2D image and by correcting the obtained intensity as explained in details in appendix A.2.2. The resulting intensity as a function of 2θ can easily be transformed through the relation $Q = 4\pi sin\theta/\lambda$ in a function of Q, $I(Q)$, which is proportional to the cross section $\frac{1}{N}\frac{d\sigma}{d\Omega}$. The total structure factor $S(Q)$ can be obtained from $I(Q)$ through Eq. 2.16 after adequate normalization. The pair distribution function $g(r)$ is then calculated from $S(Q)$ through Fourier transform (see Eq. 2.18)

over a range of Q, that in our case has been chosen between 0.1 and 12 $Å^{-1}$, and by using the densities of Table 2.2.

The S(Q) and g(r) of the undoped GeTe sample are shown in Fig.2.6. They both corresponds very well to those reported in Ref.[27]. From ab initio simulations, [33] it is known that the first peak of $g(r)$ (at about 2.6 Å) is due to the contributions of mostly Ge-Te bonds with only a few Ge-Ge bonds. The Te-Te bonds give the principal contribution to the second peak of $g(r)$ (around 4.1 Å). In Fig. 2.7 the g(r) of amorphous GeTe is compared to that of crystalline GeTe measured under the same experimental conditions. In crystalline GeTe, the contribution to the first peak is due to the short and long Ge-Te distances in the rhombohedral structure while the second peak is due to Ge-Ge and Te-Te second neighbours (see Fig.1.11).

In Fig.2.8 the first two peaks of the pair distribution functions obtained for the GeTeC (a) and GeTeN (b) samples are reported and compared to undoped GeTe. In all cases, the first peak at around 2.6 Å remains unchanged, indicating that the first distances are not affected by doping, while there is an effect on the second peak. A new peak appears at around 3.5 Å in the doped samples and the intensity of the peak at around 4.1 Å is reduced. If one observes the differences between the samples doped with different dopants concentrations it is clearly visible that the effects increase as a function of doping and are more marked for the GeTeC samples than for the GeTeN samples.

It is important to recall that through the experiment it is possible to measure only the total functions and not the partial ones, as already underlined in section 2.2. The contribution of the various elements to the factors $\langle f \rangle^2$ and $\langle f^2 \rangle$ of Eq. 2.15 is proportional to the concentration of each element and to its atomic number Z. Thus, the contributions of bonds involving C or N is negligible due to the low atomic number and weak concentration of C and N atoms compared to Ge and Te atoms. For instance, in C-doped GeTe containing 16.3 at. % of C the contribution of pairs involving C (Ge-C, Te-C and C-C) to the measured g(r) is much smaller (respectively, 1.6%, 2.8% and 0.04%) than that of Ge-Ge (12.5%), Ge-Te (44.1%) and Te-Te (38.8%) pairs. Only the Ge-Ge, Ge-Te and Te-Te bonds contribute to the total pair distribution function determined

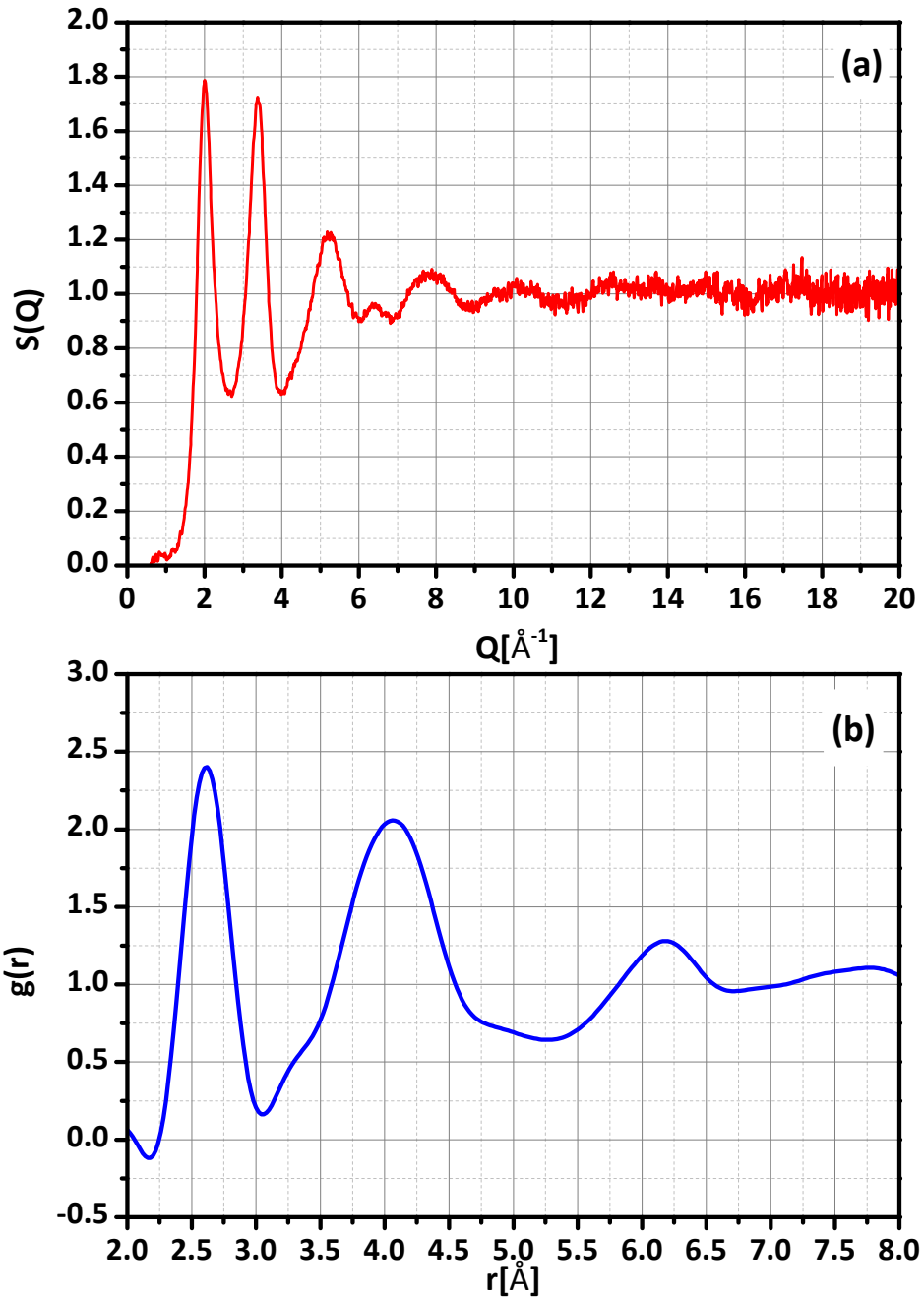

Figure 2.6: Measured (a) $S(Q)$ and (b) $g(r)$ for undoped amorphous GeTe. It can be noted that $S(Q)$ tends to 1 for high Q.

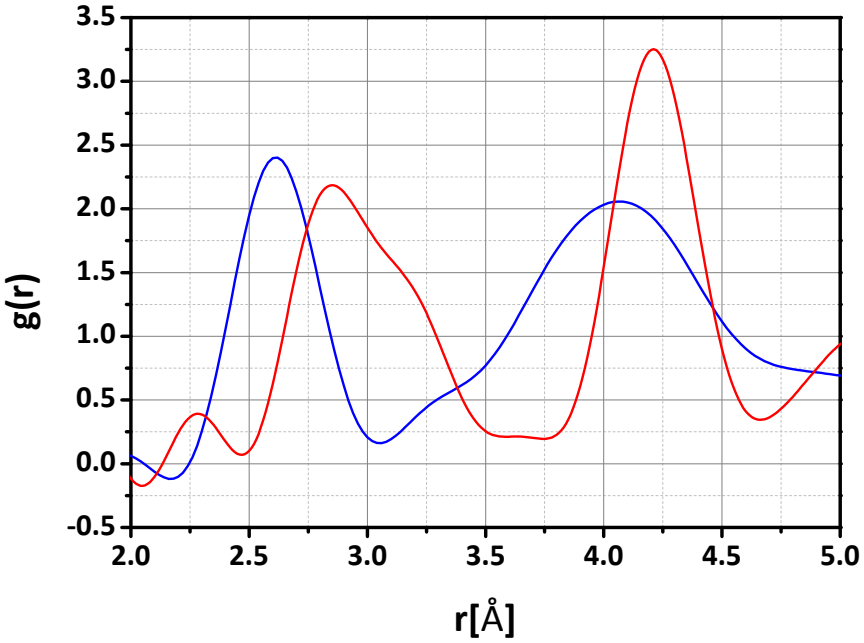

Figure 2.7: Comparison between the measured g(r) of amorphous (blue) and crystalline (red) undoped GeTe.

experimentally and one can conclude that the new peak appearing for the doped samples is not due to bonds directly involving C or N.

2.5 Ab initio simulations

Considering that only the total pair distribution functions can be measured experimentally, it is impossible to deduce the origin of the peak of g(r) that appears for doped samples. In order to go further in the analysis, ab initio molecular dynamics simulations were performed for both GeTeC and GeTeN by Dr J-Y. Raty of the University of Liège. The simulations were done on 210 atom boxes (92 Ge, 86 Te, 32 C for the C-doped sample and 97 Ge, 92 Te, 21 N for the N-doped sample) corresponding to $Ge_{52}Te_{48}$ doped with 15 at. % C and 10 at. % N. The initial positions of Ge and Te atoms were those found in a previous simulation of amorphous GeTe [50]. Then C (or N) atoms were introduced by randomly substituting Ge and Te atoms. The electronic properties were com-

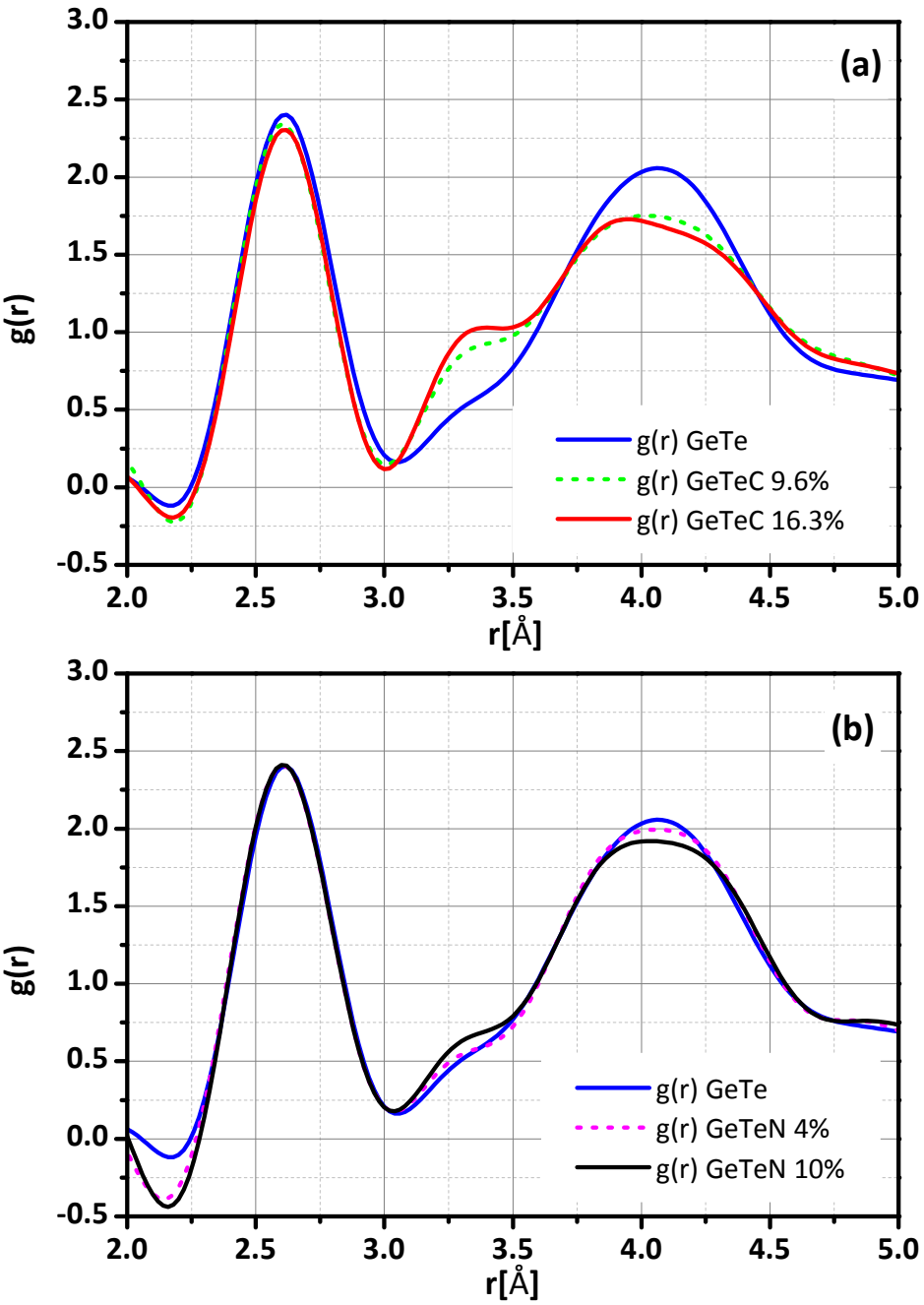

Figure 2.8: Measured $g(r)$ for (a) undoped GeTe and GeTeC (C=9.6% and 16.3%) and (b) undoped GeTe and GeTeN (N=4% and 10%). In both cases, the first peak is constant with doping while the intensity of the second peak of the undoped sample decreases with increasing doping contents. A new peak appears at around 3.5 Å in the doped samples. These effects increase as a function of doping and are stronger in the GeTeN case.

puted within density functional theory (DFT) implemented in the VASP code, using PAW potentials and the PBE-GGA exchange correlation as described in Ref.[51]. The liquid system was simulated at 3000 K for 3 ps, and then thermalized at 1073 K for 10 ps. It was cooled down to the final temperature of 300 K with a 30 K/ps ramp. The density was adjusted to minimize the effective stress on the simulation box. The refined atomic densities are 0.033 atoms/$\mathring{A}^3$ for undoped GeTe, 0.0343 atoms/$\mathring{A}^3$ for GeTeC15% and 0.0337 atoms/$\mathring{A}^3$ for GeTeN10%, close to what measured experimentally. The amorphous structural data were gathered by averaging relevant quantities over a 10 ps trajectory at 300 K.

From the simulation it is possible to obtain all the partial pair distribution functions $g_{\alpha\beta}(r)$ and so it is possible to evaluate the contribution of each atomic pair, including the ones involving light elements that could not be observed experimentally. The total stucture factors $S_{calc}(Q)$ have been obtained from weighted partial structure factors as described in Eq. 2.17. The pair distribution functions $g_{calc}(r)$ have been then calculated from $S_{calc}(Q)$ though Fourier transform as described in Eq. 2.18, using the same window $0.1< Q <12$Å as for the experimental data, and the results are shown in Fig.2.9. For undoped GeTe, the calculated $g_{calc}(r)$ is in good agreement with literature [28, 33, 52]. In the calculated $g_{calc}(r)$ the first peak remains almost constant with doping, the second peak decreases with doping and a new peak appears around 3.3Å for the doped samples. The effects of C and N doping on the amorphous structure of GeTe are comparable.

By comparing the simulated and experimental $g(r)$ in Fig.2.9, a shift in the peak positions can be observed. The existence of this shift is already known from literature [53, 54]. Besides, in the experimental $g(r)$ the effect of N doping is weaker than the one of C doping. However, apart from those two differences, the good agreement between the evolution as a function of doping for the simulated and measured total pair distribution functions allows to conclude that the *ab initio* simulation takes properly into account the effect of dopants on the amorphous structure of GeTe.

The next step is to analyze the information that can be obtained from a visual

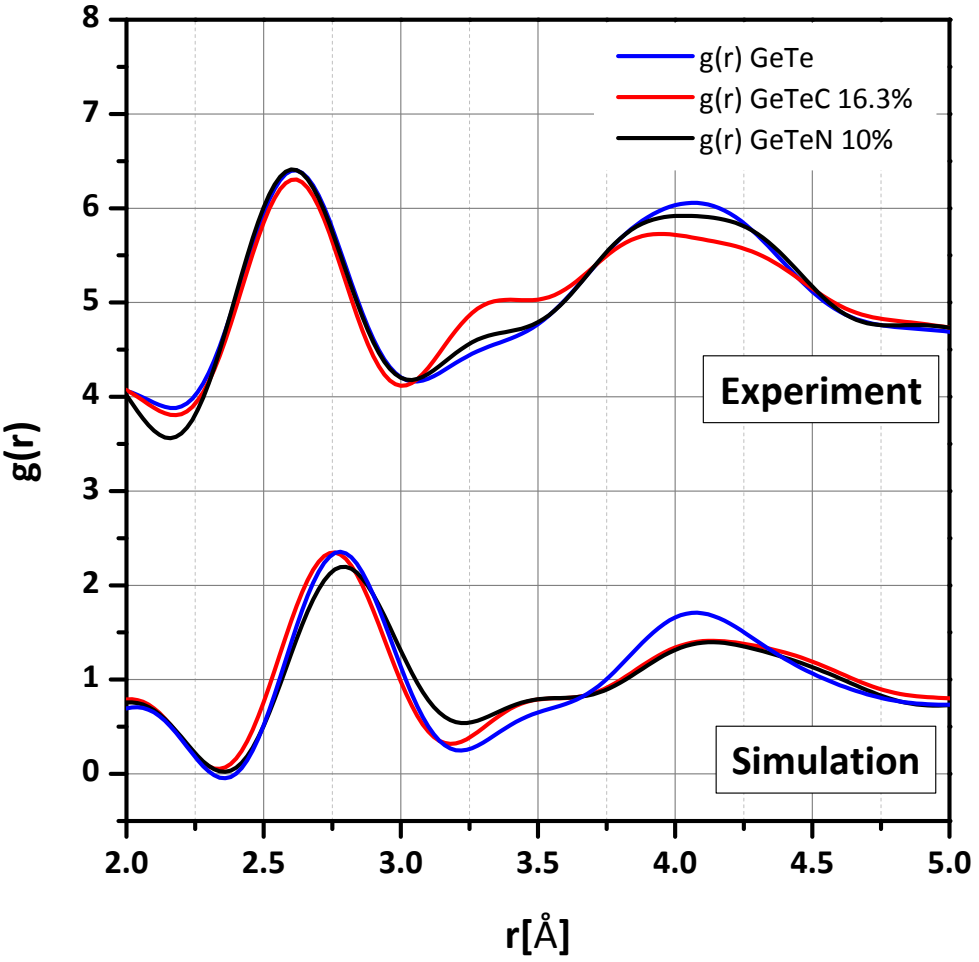

Figure 2.9: Comparison between measured and calculated $g(r)$ for undoped GeTe, GeTeC (C=16.3% in the experiment and C=15% in the simulation) and GeTeN (N=10% both in the experiment and in the simulation). Even if an already known shift between peaks positions can be observed, the evolution of the simulated and measured pair distribution functions with doping are in good agreement. The effect of N-doping is stronger in the calculated $g(r)$ than in the measured one.

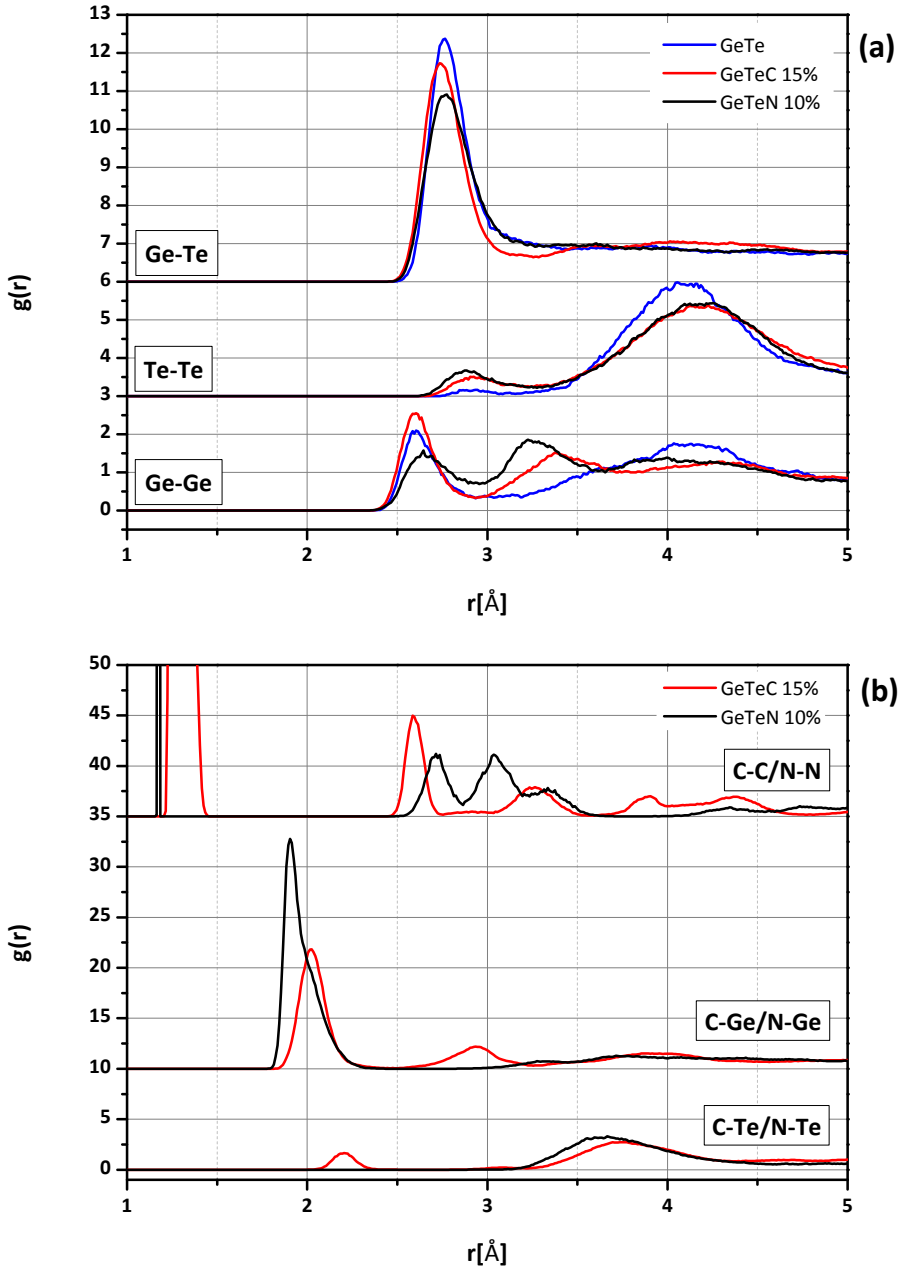

Figure 2.10: Partial pair distribution functions for (a) Ge-Ge, Te-Te, and Ge-Te pairs in doped and undoped samples and (b) pairs involving C or N. Curves are shifted for clarity. A new peak appears in the range 3.1-3.5 Å in the Ge-Ge partial pair distribution function for both C doped and N doped samples, while it is absent in the undoped sample. A difference between partial contributions involving C and the ones invloving N is the absence of Te-N bonds at small distances (less than 3.2 Å).

inspection of the simulation boxes and from the calculated partial pair distribution functions in order to understand the local atomic arrangements. The partial pair distribution functions calculated for GeTe, GeTeC15% and GeTeN10% are shown in Fig.2.10. For simplicity, in Fig.2.10(a) the pair contributions due to Ge-Ge, Ge-Te, and Te-Te pairs in doped and undoped samples are reported, shifted for clarity, while the pairs involving C or N are reported in Fig.2.10(b). From Fig.2.10(a) it is evident that the contributions to the first peak are given by a few Ge-Ge bonds, at an average distance of 2.63 Å for GeTe and GeTeC samples and 2.65 Å for the GeTeN sample, and mostly by Ge-Te bonds at an average distance of 2.74 Å in GeTeC and 2.76 Å in GeTe and GeTeN. For both doped and undoped GeTe the most probable Te-Te distance is rather large (around 4.1 and 4.2 Å), with only a few Te-Te bonds about 2.95 Å. This corresponds to a tendency for a strong chemical order due to the alternation of Ge and Te atoms that is the precursor of the rhombohedral crystalline GeTe structure [55] and this tendency is maintained in presence of doping. The most relevant result is the appearance of a new peak at around 3.39 Å in the Ge-Ge partial pair distribution function for both C doped and N doped samples, while it is absent in the undoped sample.

Let us focus first on the analysis of the C-doped sample. From Fig.2.10(b) the presence of C-C bonds at a very short distance (1.31 Å) can be noticed. These bonds were not present in the initial state of the system and correspond to a p-type of bonding. By observing the snapshot of the final state of the simulation box for GeTeC reported in Fig.2.11, C chains of various lengths ($2-5$ atoms) can be observed, without any branching. Observing Fig.2.10(b) it is also possible to notice many C-Ge bonds that contribute to the partial pair distribution function at an average distance of 2.05 Å. Also a few C-Te bonds are present, with a contribution at around 2.23 Å, but they are much less frequent than C-Ge bonds.

The analysis of bond angle distribution shows that Ge atoms for undoped GeTe are either in a tetrahedral environment (about 25%-35%) or in a strongly distorted octahedral environment. In C-doped GeTe, the bond angle distribution becomes broader making the distinction between tetrahedral and octahedral environment less clear. The inspection of the model structure (Fig.2.11) com-

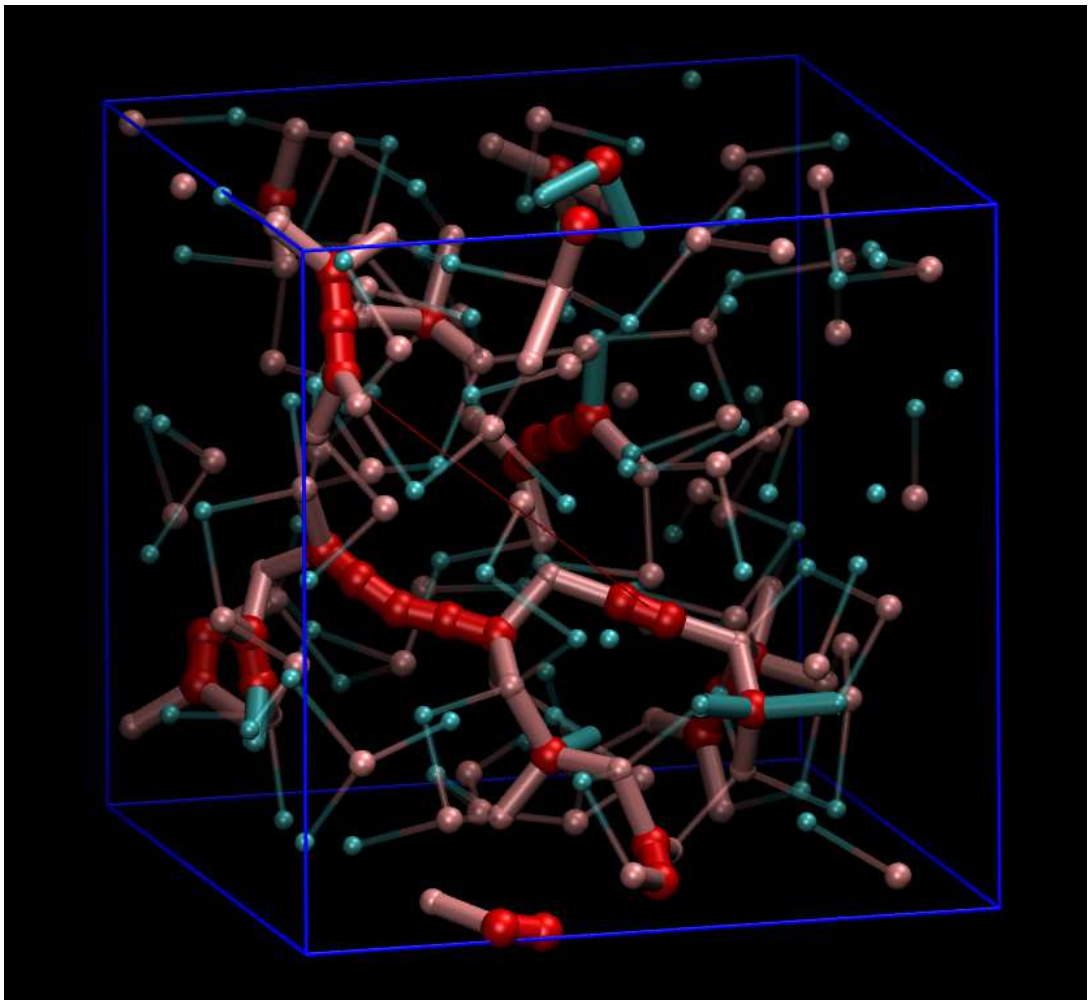

Figure 2.11: Snapshot of the final state of the simulation box for GeTeC. Ge atoms are represented in pink, Te atoms in light blue and C atoms in red. The inspection of this box combined with a bond angle analysis around C atoms, reveals the presence of a mixture of tetrahedral ($C-TeGe_3$, $C-Ge_4$ and $C-Ge_2Te_2$), triangular ($C-C-Ge_2$ and $C-C-GeTe$), and linear (C chains) bonds.

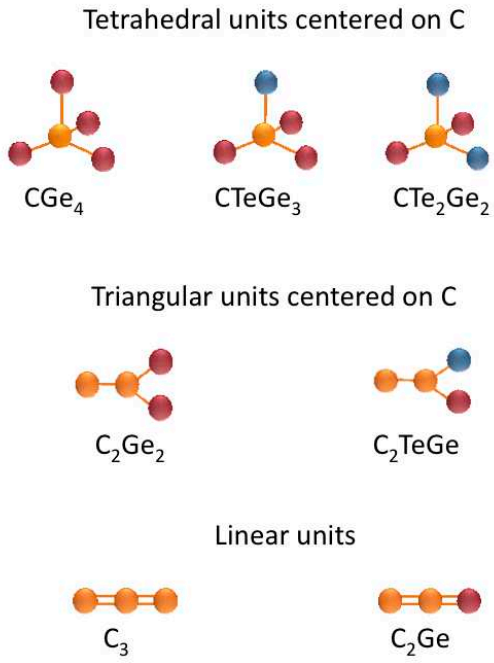

Figure 2.12: Summary of the carbon environments in the C-doped GeTe sample. $C-TeGe_3$, $C-Ge_4$ and $C-Ge_2Te_2$ tetrahedra can be found, as well as $C-C-Ge_2$ and $C-C-GeTe$ triangular environments.

bined with a bond angle analysis around C atoms reveals the presence of a mixture of tetrahedral (sp3), triangular (sp2), and linear (sp) C-Ge bonds. The $C-TeGe_3$ tetrahedra are the majority (3 are present) and one $C-Ge_4$ and one $C-Ge_2Te_2$ tetrahedra can also be found, in agreement with the relative ratio of C-Ge and C-Te bonds. Eleven $C-C-Ge_2$ and one $C-C-GeTe$ triangular environments are also present. A schematic representation of the environments involving carbon is depicted in Fig.2.12. Two Ge atoms belonging to the same tetrahedral unit centered on a carbon atom result to be separated on average by 3.39 Å and that is the same distance for two Ge of a $C-C-Ge_2$ triangle. This Ge-Ge distance is induced by the presence of C and it can be clearly seen in Fig.2.10(a), where a new peak appears at 3.39 Å in the Ge-Ge partial pair distribution of GeTeC. In the r-range from 3.2 to 3.6 Å the Ge-Te and Te-Te partial pair distribution are only slightly affected by C doping.

Let us now analyze the N-doped sample. By comparing with GeTeC, the first striking difference that can be noticed is the absence of Te-N bonds at small distances (less than 3.2 Å) for GeTeN while there are a few Te-C bonds

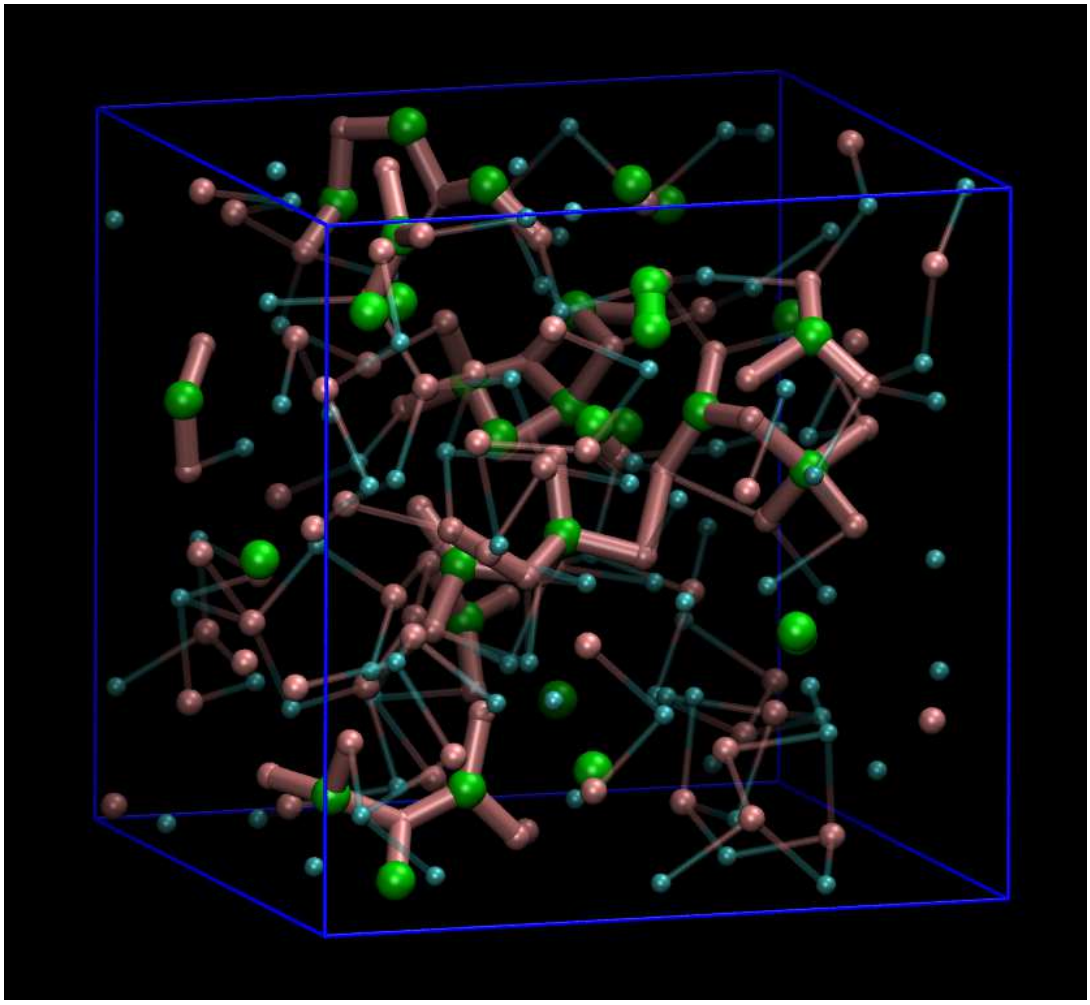

Figure 2.13: Snapshot of the final state of the simulation box for GeTeN. Ge atoms are represented in pink, Te atoms in light blue and N atoms in green. $N-Ge_3$ pyramidal environments, $N-Ge_4$ tetrahedral environments and N_2 molecules can be found.

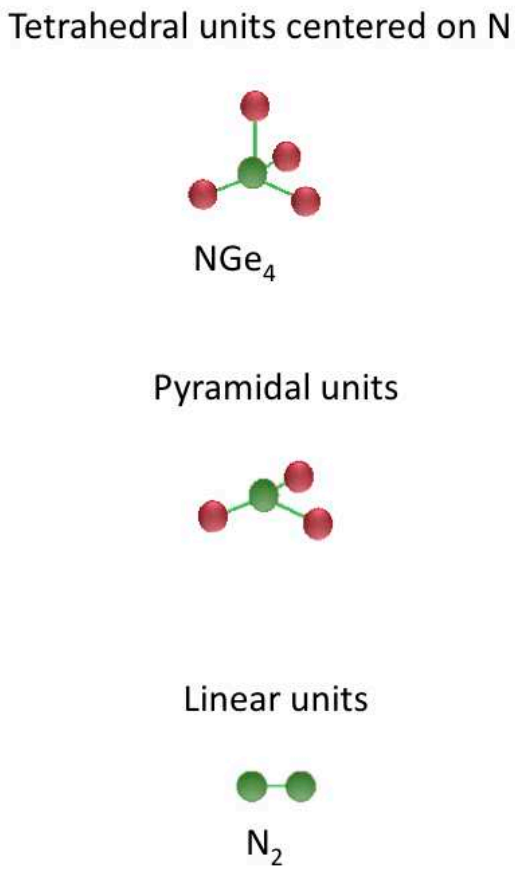

Figure 2.14: Summary of the nitrogen environments found in the N-doped GeTe sample. $N-Ge_4$ tetrahedra, $N-Ge_3$ pyramids and N_2 molecules have been observed.

at around 2.23 Å in GeTeC. The only bonds involving N that can be found in GeTeN for r $<$ 3.2Å are Ge-N and N-N bonds. In the snapshot of the final state of the simulation box for GeTeN reported in Fig.2.13, 8 $N-Ge_3$ pyramidal environments, 9 $N-Ge_4$ tetrahedral environments and 2 molecules of N_2 can be found. The observed environments for N-doped GeTe are reported in Fig.2.14. It should be noticed that during the simulated annealing procedure, the initial configuration was taken from a liquid sample equilibrated at a very high temperature (3000 K), so that any kind of possible bond was present in the structure, including Te-N bonds. However, due to the low N concentration, no N_2 molecule was present in the liquid. It is thus striking to find that all the Te-N bonds have been disrupted upon cooling and statistically unlikely N_2 molecules have formed.

2.6 Discussion

The two main conclusions of this work are that, on one hand, the strong chemical order between Ge and Te characteristic of amorphous GeTe is maintained in presence of C or N doping elements and that, on the other hand, dopants deeply modify the structure of the amorphous phase by introducing new environments. A common feature of the C and N doping is the appearance of tetrahedral units centered on C or N. In C-doped amorphous GeTe, triangular environments around C and short C chains (containing between 2 and 5 C atoms) can also be found, while in N-doped GeTe NGe_3 pyramids and N_2 molecules are also present. One major difference between N and C doping is the fact that C can form short bonds with Te, although in smaller proportion than C-Ge and C-C bonds, while short N-Te bonds are absent in N-doped GeTe. The same conclusion has been recently obtained in Ref. [56] through X-ray absorption spectroscopy and X-ray photoemission spectroscopy (XPS). The fact that C is bonded preferably to Ge has also been found by ab initio simulations in the case of C-doped GST in studies performed at the same time as the study reported in this thesis [57, 58]. In N-doped GST, ab initio simulations show that N is bonded in majority to Ge, to Sb in a less extent and marginally to Te [59].

In C-doped GeTe, two Ge atoms belonging to the same tetrahedral or triangular unit are separated by 3.4 Å. This Ge-Ge distance, that did not exist in undoped amorphous GeTe, appears as a new peak in the Ge-Ge partial pair distribution function and is also visible in the calculated total g (r). From these ab initio simulations, it can be concluded that the additional peak observed around 3.3 Å in the measured pair distribution function of GeTeC (C=9.5%) and GeTeC (C=16.3%) is mainly due to this new Ge-Ge distance present in tetrahedral and triangular units centered on carbon. The contribution of Ge-Te and Te-Te distances to the total g (r) in this r-range is much less than that of Ge-Ge distances because of the small number of C-Te bonds compared to C-Ge bonds. In N-doped GeTe two Ge atoms belonging to the same tetrahedral or pyramidal unit are separated by 3.25 Å. They generate a new peak in the Ge-Ge partial pair distribution function and in the calculated total g (r).The effect on

the measured g (r) of GeTeN (N=10%) is smaller than predicted by the calculation. One explanation could be that the sample contains more N_2 molecules than the simulation box so that the relative abundance of NGe_4 and NGe_3 units is reduced in the sample. Information from literature on the presence of N_2 molecules in N-doped amorphous GeTe is contradictory at the present time. N_2 molecules have been found by X-ray absorption and XPS experiments in Ref.[60] but not in [56].

It is worth noting that the samples studied experimentally in this work are as-deposited amorphous samples, while the simulation results are collected on an amorphous state obtained by a rapid quench of the liquid phase (the so called melt-quenched amorphous). The structure of these two amorphous states could differ. This question has been addressed in literature in the case of N-doped GeTe by ab initio simulations [54]. The conclusion of this study is that the difference in the local structure between as deposited and melt-quenched amorphous phase is only the number of tetrahedral environments.

One can wonder whether the structural changes observed in doped GeTe can be related to the enhanced crystallization temperature and activation energy of C and N-doped GeTe. The presence of C or N makes the Ge environments, on average, slightly more tetrahedral. According to the ideas developed in Ref.[50], this structural change would increase the average number of constraints so doping could indeed increase the stability of the amorphous state. This idea led to a study of the vibrational properties of C and N-doped amorphous GeTe by combining Fourier Transform Infrared spectroscopy (FTIR) experiments and computation of the vibration modes from the ab initio simulations presented in section 2.5. The main conclusion of this study (Ref.[61], submitted for publication) is that the inclusion of C and N creates high frequency, localized modes, and at the same time decreases the density of low frequency acoustic-like modes. In Ref.[61] it is shown that this kind of effects corresponds to an increased stability of doped amorphous GeTe. Besides, in the case of C-doped GeTe the presence of C chains could be an obstacle for the crystallization of the GeTe matrix, provided that these C-C bonds disappear in the crystalline phase, since breaking a C-C bond is an extremely endothermic process.

2.7 Conclusions and perspectives

In conclusion, the addition of carbon or nitrogen in GeTe has been observed to deeply modify the structure of the amorphous phase. Both dopants induce the formation of new environments and bonds, resulting in a more stable amorphous structure , which could explain the increase of the crystallization temperature and activation energy induced by doping. In parallel to the work described in this chapter, the effect of carbon doping on the properties of GST has been observed experimentally very recently [62]. In that case ab initio simulations [57, 58] have preceded the experimental study. The conclusion of all these works is that carbon doping enhances the stability of the amorphous GST phase, like in the case of C-doped amorphous GeTe studied in this thesis.

An enhanced stability of the amorphous phase would produce an increase of the retention time, beneficial for PCM. Such an increase is indeed observed in PCM containing C on N doped GeTe [44, 41]. However, understanding its origin requires further studies since other effects could contribute as well. From the device point of view, the capability of the material to maintain its properties after many phase transformations is an imperative requirement. Therefore, starting from the understanding of the amorphous structure of C and N doped amorphous GeTe, the next step must be the study of the crystalline phase. At the moment it is unclear if the doping elements remain in the crystalline phase, at substitution or interstitial sites, or if they segregate, for instance at the grain boundaries. In the latter case one can wonder if they are incorporated again in the amorphous phase upon reamorphization.

Little is known on the crystalline structure of C and N doped GeTe. One result is that the crystalline phase is cubic at room temperature for C and N content above 10% [60, 63]. In the case of crystalline N-doped GST (NGST) distortions of the crystal lattice and reduction of the grain size have been observed [34, 64]. The conclusion was that the N atoms occupy tetrahedral interstitial sites in the NGST crystalline structure and that a Ge_3N_4 phase is formed near the grain boundaries, thus reducing the grain size. Moreover, the presence of some N_2 molecules was also observed. The molecular nitrogen is believed to

exist at interstitial and vacancy sites, and more likely at grain boundaries [37].

Further studies are required in order to localize the dopants in the crystalline phase. Characterization techniques such as X-ray photoemission spectroscopy and Fourier transform infrared spectroscopy will be useful to provide a detailed comparison of the amorphous and crystalline phases and to investigate the evolution between them. Finally, local analysis via transmission electron microscopy could be useful to study amorphous and crystalline phase in both thin films and integrated materials.

Chapter 3

Confinement of phase change materials: $Ge_2Sb_2Te_5$ nanoclusters

3.1 Introduction

One of the open questions about the competitiveness of PCM is at which extent their dimensions can be reduced. Their theoretically very high scalability is one of their most promising properties, as it can make them become competitive with Flash memories. In terms of devices, the scaling of the memory cell is limited by architectural and geometrical issues and by material scaling possibilities. Thus, it is important to investigate the effect of shrinking size on the phase change materials properties and characteristics. First, it is of the uttermost importance to establish if there is a limit size under which the phase transformation can no longer occur. Moreover, as it will be discussed further in the following sections, the effect of reduced dimensions on the mechanisms of crystallization is still an open question. This confinement effect can be studied at different extents: the first approach is to investigate the effect of reducing thickness of PC thin films on the phase change mechanism. A further step consists in investigating confined nanostructures of PC materials, such as nanowires and nanoclusters. In this chapter, an overview of the results obtained on confined structures will be presented. A new method for the deposition of PC nanoparticles of diameter below 10 nm will be introduced and results obtained on $Ge_2Sb_2Te_5$ (GST) particles embedded in Al_2O_3 will be presented. The results presented in this chapter have been published in Ref. [65].

3.1.1 Effect of shrinking size in one dimension: thin films

Many studies regarding the scalability of PCM deal with the thickness dependence of the amorphous to crystalline phase transition in PC thin films, meaning the effect of confining the material in only one dimension. In the following, a review of the main results from literature on GST will be presented. First, evidences of the influence of thin films thickness on the crystallization temperature T_x will be shown, then the crystallization mechanisms will be discussed and at the end some interesting results on multilayers will be reported.

In literature, the crystallization behavior of a PC material has been investigated by several experimental methods, as for example optical measurements

[66], electrical measurements [67], Transmission Electron Microscopy (TEM) [68], Differential Scanning Calorimetry (DSC) [69] or X-Ray Diffraction (XRD) [70]. All the quantities measured by these methods are directly proportional to the quantity of crystalline matter in the sample, except the case of resistivity measurements where the value of resistivity decreases only when a crystalline path between electrodes is formed. There is no generally admitted definition of the crystallization temperature T_x and different criteria are used. For example, it can be defined as the temperature at which the first derivative of a reflectivity curve with respect to temperature has a maximum value, or as the point at which the resistance of a sample is reduced by a factor of 2, or as the peak point in a Differential Scanning Calorimetry experiment. The experimental conditions are different for all these techniques, and considering that crystallization is ruled by kinetic theories, the value of T_x depends on the thermal history of the sample and thus on these conditions. This means that the value of T_x depends on both the experimental conditions and on the criteria used to define it.That said, under the same experimental conditions, it is widely assumed that a PC material film at least 100 nm thick should be characterized by a crystallization temperature T_x that is independent form the surrounding layers and can be considered as its *bulk* crystallization temperature.

In 2007, Wei et al. measured the amorphous to fcc rocksalt phase transition temperature, the crystallization speed and activation energy (Kissinger method) for thin films of GST of various thicknesses (5, 10, 15, 20 and 30 nm) sandwiched by 50 nm of $ZnS - SiO_2$ [67]. The crystallization temperature T_x increases as the film thickness d is reduced below 20 nm, as can be seen in Table 3.1, while the crystallization speed decreases (as shown in Figure 3.1). No thickness dependence of parameters has been found for films thicker than 20 nm. The estimated crystallization activation energy increases with decreasing thickness, from 2.86 eV for 20 nm thick films to 4.66 eV for 5 nm thick films, and a linear relationship has been found between $\ln[T_x]$ and the thickness d of the GST thin films. Moreover, the Avrami coefficient n (described in section 1.3.5) has been measured and it has been found that $n > 1.5$ for $d \geq 20$ nm, while $1 < n < 1.5$ for $d = 10$ nm and $n < 1$ for $d = 5$ nm. This suggests that the nucleation and

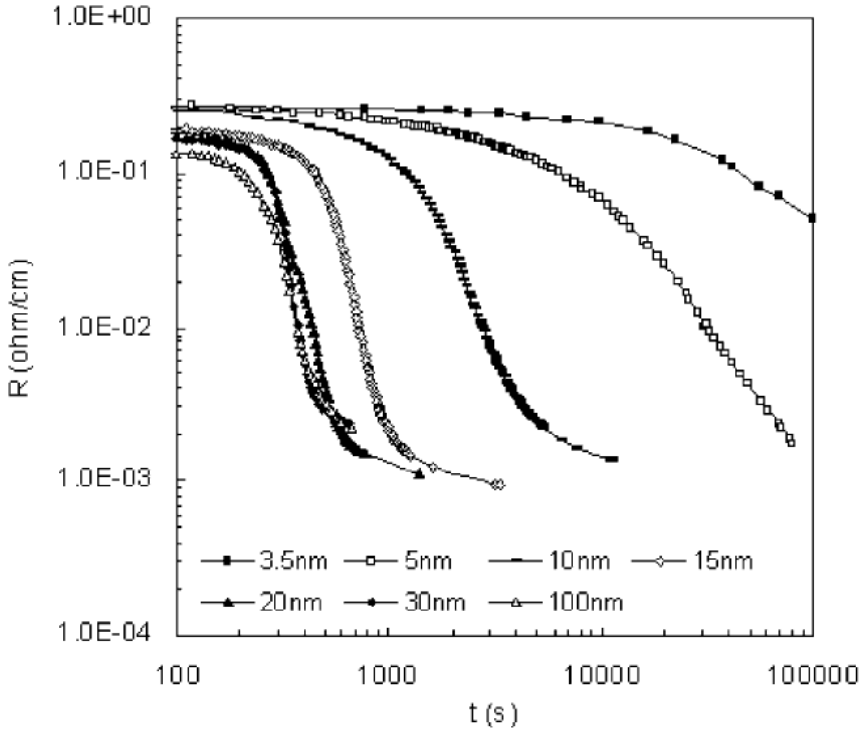

Figure 3.1: Resistivity as a function of time at room temperature for thin films of GST of different thicknesses pre-annealed at 143.5°C (from Ref.[67]). The incubation time τ, defined as the time elapsed before the onset of crystallization, and the transition time from the highest to lowest resistivity increase with decreasing film thickness, meaning that the crystallization speed is reduced for small thicknesses.

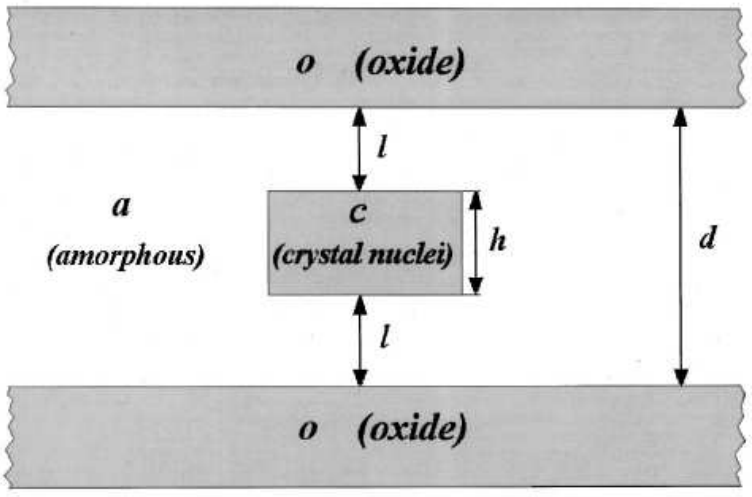

Figure 3.2: Model used Ref.[71] to interpret the thickness-dependent variation of T_x . A cylindric crystalline nucleus is embedded in the amorphous phase, sandwiched between two oxide interfaces.

Heating rate (°C /min)	5 nm	10 nm	15 nm	20 nm	30 nm
0.5	157	149	141	138	138
1	159	153	147	142	142
3	164	157	152	148	148
10	166	160	155	154	154
20	170	164	160	157	157

Table 3.1: Crystallization temperatures as a function of heating rate and GST film thickness from Ref.[67].

growth mechanisms change by decreasing thickness.

In order to explain the thickness-dependent increase of T_x for thin films of Si with oxide interfaces a model has been proposed by Zacharias [71] and it has been be applied to PC materials. In this model, based on homogeneous nucleation, an effective interfacial energy between the oxide capping layer and the surface of a growing crystalline cylindrically shaped nucleus in the amorphous matrix (see Fig.3.2) is introduced. This effective interfacial energy is a function of the distance between the nucleus surface and the oxide. By calculating the Gibbs free energy for the nucleus, the crystallization temperature T_x can be expressed as an exponential function of the phase change film thickness d

$$T_x = T_{ac}\left[1 + \left(\frac{\gamma_{oc} - \gamma_{ac} - \gamma_{oa}}{\gamma_{ac}} e^{-d/4l_0}\right)\right] \tag{3.1}$$

where γ_{ac}, γ_{oc}, and γ_{oa} are defined as the interfacial free energies per unit area between the amorphous and crystalline phases (ac), between the oxide capping layer and the crystalline phase (oc), and between the oxide capping layer and the amorphous phase (oa), respectively. T_{ac} is the bulk crystallization temperature and l_0 can be interpreted as an average screening or bonding length which is related to the range of interatomic forces typical for the materials o and c. The values reported in Table 3.1 can be fitted by Eq. 3.1, as reported in Ref.[67].

Another study on the effect of reducing thin film thickness over the crystallization temperature T_x has been published by Raoux and coworkers [70]. The value of T_x has been measured for films of various thicknesses (from 1 to 50 nm) and different materials (GST, N-doped GST, $Ge_{15}Sb_{85}$, Sb_2Te and Ag- and

In-doped Sb_2Te). All the samples were deposited on Si and capped with 10 nm of Al_2O_3 . They have been characterized through X-Ray diffraction during in-situ annealing with a heating rate of 1°C /s. The transition temperature T_x , corresponding to the amorphous to fcc rocksalt structure transformation, is similar to that of the bulk (close to 155°C) for all films with thicknesses above 10 nm. T_x increases with decreasing thickness below 10 nm for all the considered materials, but at a different extent for each composition. The value reported for T_x is 342°C for a 5 nm thin GST film and 380°C for a 2 nm thin GST film, where the phase transition proceeds directly from the amorphous to the hexagonal phase. It can be noted that the variation of T_x with thickness for the GST films capped with Al_2O_3 of Ref. [70] is much higher than for the GST films of Ref. [67] capped with $ZnS - SiO_2$. It is also worth noting that the so called *bulk* crystallization temperature is 155°C in Ref.[70] and 142°C in Ref.[67] for the same heating rate. This could come from the different experimental methods (resistance measurements in Ref.[67] and X-ray diffraction in Ref.[70]). Other possibilities are that the composition of the material is not exactly the same (there can also be an inclusion of undesired doping elements) or that the different interface materials still influence T_x in films of 30-50 nm thickness (see Chapter 4). The thickness dependence of T_x in Ref. [70] have been interpolated using Eq. 3.1 [71] as it is shown in Fig.3.3. On the other side, the transition from the cubic phase to the hexagonal phase occurs at the same temperature for all film thicknesses, around 450°C . The thinnest GST film that shows evidence of Bragg peaks is 2 nm thick, so the authors of Ref. [70] conclude that this thickness is the size limit for the existence of a phase change transformation for GST.

In 2009, Simpson et al. measured the crystallization temperature of thin films of GST of thicknesses between 2 nm and 10 nm encapsulated by TiN or $ZnS - SiO_2$ [72]. In the case of TiN an increase of T_x with decreasing thickness has been obtained, similar to the trend observed in Ref.[70] for GST encapsulated in Al_2O_3 , while for encapsulation with $ZnS - SiO_2$ T_x is decreasing with thickness. The latter result is in contradiction with what observed in Ref. [67] and reported in Table 3.1. Both in Refs. [72] and [67] the variation of T_x with

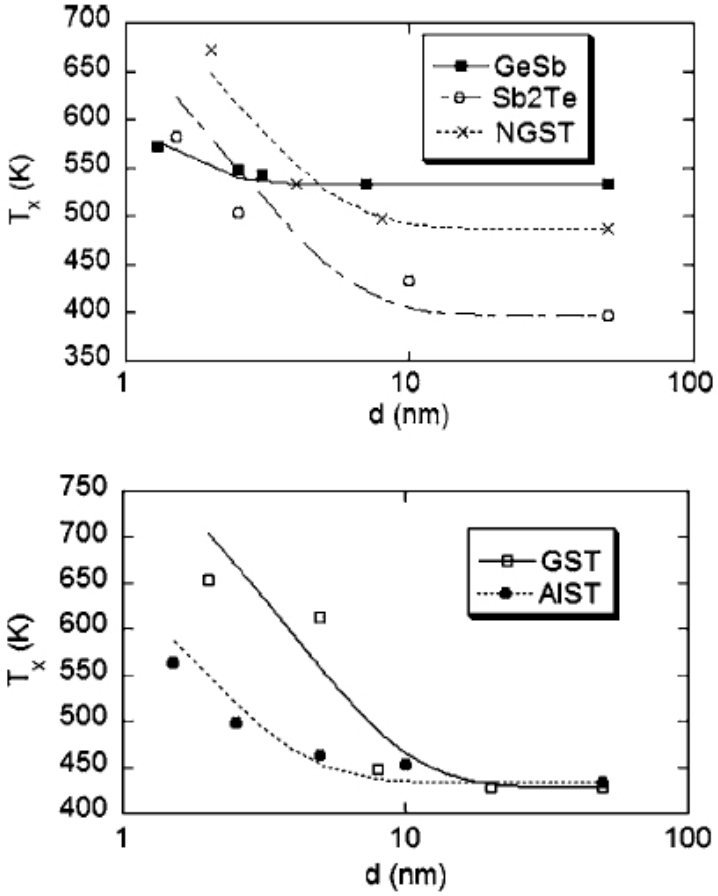

Figure 3.3: Crystallization temperature T_x as a function of film thickness for various PC materials: GST, N-doped GST (NGST), $Ge_{15}Sb_{85}$ (GeSb), Sb_2Te and Ag- and In-doped Sb_2Te (AIST) deposited on Si and capped with Al_2O_3 , fitted using Eq.3.1, as presented in Ref.[70].

decreasing thickness for GST interfaced with $ZnS - SiO_2$ is small, but in Ref. [72] T_x increases with decreasing thickness while the opposite trend is observed in Ref. [67]. The authors of Ref. [72] proposed the existence of a correlation between the mechanical stresses induced by the cladding material and the change in T_x . One difficulty with this interpretation is that, even in the case where the stress in the cladding layer is known, the evaluation of the level of strain induced in the embedded layer is delicate [73]. Other recent studies indicate that compressive and tensile stress inhibit the rocksalt to hexagonal phase transition when the GST film thickness is thinner than 10 nm [74].

From all these results it is evident that the effect of confinement on phase change cannot be separated from the effect of interaction between the interface material and the PC material itself. The influence of interface materials on crystallization of an amorphous compound had been studied also out of the PCM context. For example, in 1969 Oki et al. reported that a $10 - 30$ nm film of Ge crystallizes at different temperatures if interfaced with a metal [75]. In a study on Pb/Ge multilayer samples in 1987 [76] a decrease of T_x with decreasing Ge thin films thickness has been observed, and it has been suggested that the crystallization is interfacially initiated and strongly affected by the Pb layer texture. In late 1990s, the effect of the interface layer on crystallization mechanism of PC materials has been extensively studied by Ohshima [66, 77]. The aim of those studies was to understand the effect of the interface dielectrics commonly used as capping layers for optical devices due to their optical good properties. Those kinds of dielectrics include SiO_2, Si_3N_4, Ta_2O_5, ZnS and $ZnS - SiO_2$. The PC materials are thin films of 30 nm with variable composition in the $Sb_2Te_3 - GeTe$ pseudobinary system (named $Ge - Sb - Te$ materials). The results indicate that the crystallization temperature, the crystallization activation energy and the nucleation process are affected by the different dielectric interfaces. The effect of the dielectric films is to accelerate the nucleation in Si_3N_4 and Ta_2O_5 capped samples, to inhibit the nucleation in SiO_2 capped sample, and to generate nuclei even during the grain growth process in ZnS and $ZnS - SiO_2$ capped samples. The author suggests that these variations may depend on the surface reactivity and chemical affinity of the film materials [66]. This conclusion has been

supported by a further study on $Ge-Sb-Te$ film interfaced with Si_3N_4 or $ZnS-SiO_2$, where a difference in the crystalline structure and in the grain growth process has been evidenced between the two different samples [77]. The films interfaced with Si_3N_4 crystallize in a fcc structure and the grain grow gradually until the fcc to hexagonal transition, while for the films interfaced with $ZnS-SiO_2$ the structure was a mixture of fcc and hexagonal structure and the grains grew abruptly at around 250°C .

In 2009, Jang et al. investigated GST/SiO_2 multilayered films with layer thicknesses of $[10.42\text{ nm}/10.42\text{ nm}]\times 5$ (named M10) and $[5.93\text{ nm}/5.64\text{ nm}]\times 10$ (named M5) [78]. Sheet resistance measurements show that the phase-change characteristics are affected by the bilayer thickness, as can be seen in Fig.3.4. In particular, the crystallization temperature seems to be slightly higher for multilayer films than for a single-layered GST thin film of 100 nm. Compared to the single-layered GST thin film, the temperature region between the amorphous to fcc transition and the fcc to hexagonal transition is reduced and it decreases further as the bilayer thickness of the multilayered structure decreases. A similar reduction was observed in Ref.[70] for GST with Al_2O_3 capping, but in that case the amorphous to fcc transition temperature increased while the fcc to hexagonal transition temperature remained unchanged, while in Ref.[78] the amorphous to fcc transition temperature increases only slightly and the fcc to hexagonal transition occurs at lower temperatures. The difference between the two studies is again the capping material, that can have a different influence on the two transitions. Moreover, in Ref.[78] it is reported (without quantitative data) that the GST film is highly strained for thin multilayers due to the different thermal expansion coefficients of GST and SiO_2.

In conclusion, results from literature on the variation of T_x with thickness are often unclear and ambiguous, and sometimes even contradictory. The interface materials play certainly an important role in determining the amorphous to fcc and the fcc to hexagonal transition temperatures, and can maybe have different influences over the two of them. Another important issue to be taken into account is the possibility of interdiffusion from the capping layer through the PC material, resulting in a doping effect instead of an interface effect. Size reduction

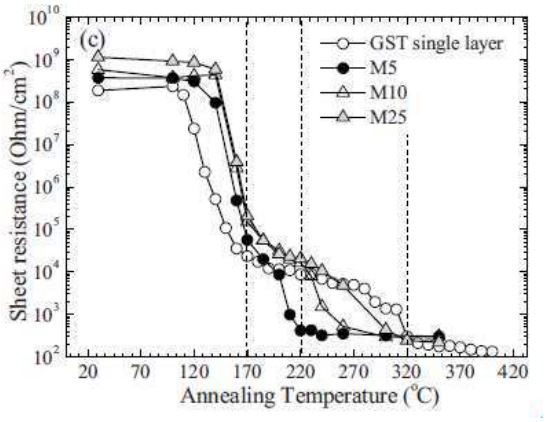

Figure 3.4: Sheet resistance of multilayered films of GST/SiO_2 as a function of annealing temperature, as reported in Ref.[78]. The label M25, M10 and M5 indicate different bilayer thicknesses (M5 corresponds to the thinnest sample, M25 the thickest one). The dotted lines correspond to ex situ annealing temperatures used for further analysis in Ref.[78].

effects have been reported for thin films but while in some cases the variation of T_x is extremely high, in other cases it is very small and not even consistent in different publications (as for the $ZnS-SiO_2$ interface in Ref.[72] and [67], as discussed above). The greatest variations of T_x have been reported for Al_2O_3 [70] and TiN [72] interfaces, but there are no further studies in literature for those materials. Some attempts to identify a relation between surface reactivity and chemical affinity of films and a change in the crystallization mechanisms with different interface materials have been done [66]. However, the physical and chemical influence of different capping layers on the phase change mechanism it is still unknown.

3.1.2 Effect of shrinking size in two and three dimensions: nanostructures

As it was discussed in the previous section, reducing the thickness of PC material thin films can have a great impact on crystallization mechanism. This has been observed through the variation of some important phase change properties such as crystallization temperature or activation energy, which depend also strongly on the interface materials. However, the studies reported in the previous section deal only with the effect of confining the PC materials in one dimension. To go

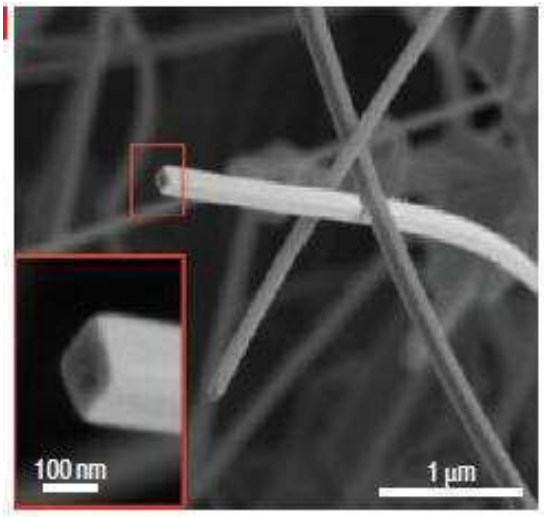

Figure 3.5: Scanning Electron Microscopy (SEM) image of as-grown GST nanowires from Ref.[81].

further, systems of nanostructures can be investigated. For example, nanowires with length much higher than their diameter can be used to study the effect of confinement in two dimensions.

In 2006, GeTe and Sb_2Te_3 nanowires have been obtained through vapor-liquid-solid (VLS) technique [79, 80]. A Scanning Electron Microscopy (SEM) image of as-deposited GST nanowires taken from Ref.[81] is reported in Figure 3.5. Interesting results about scaling effects on physical parameters have been obtained with GST nanowires of different thicknesses, from 20 to 190 nm, fabricated through VLS process [82] on a SiO_2 /Si substrate with no capping. This means that the influence of the interface layers that has such a great impact in the thin film case is reduced for such nanowires. Two Pt electrodes are directly written onto the crystalline as-deposited nanowires which can then undergo the SET and RESET operations many times. So nanowires are not only an important system for investigating crystallization at a nanoscale size, but they can also be directly employed as memory devices, even if a new device architecture needs to be developed [81]. Electrical characterizations of reamorphized nanowires show a decrease of the recrystallization time at fixed temperature, an increase in the nucleation rate and a decrease in the activation energy for decreasing diameter (Figures 3.6a, b and c, respectively).

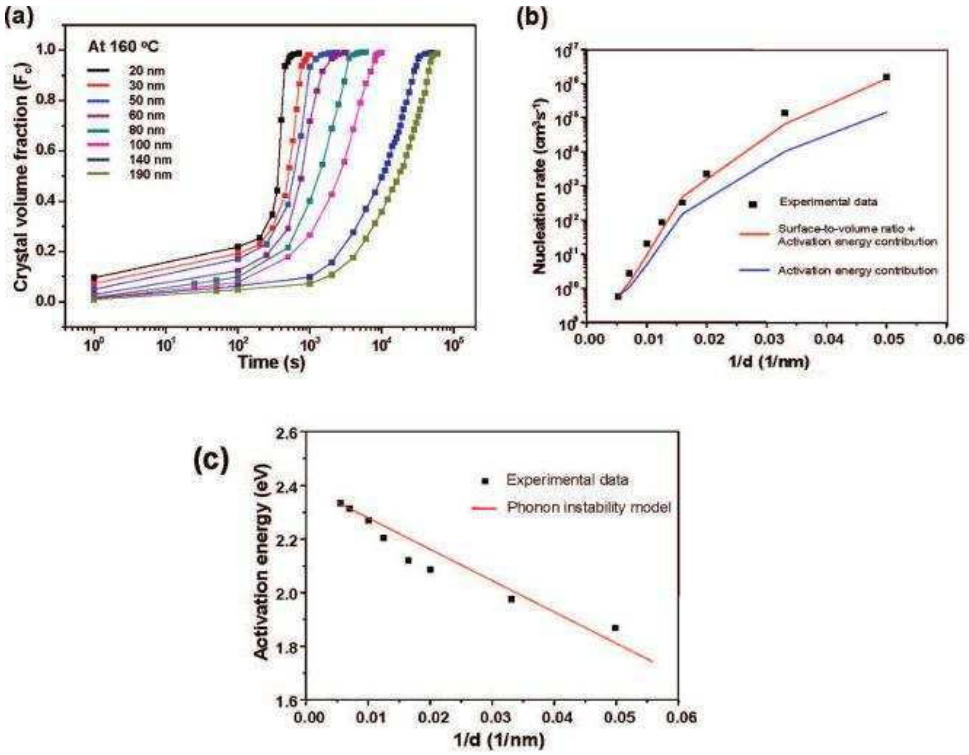

Figure 3.6: Measured values for the (a) recrystallization time at fixed temperature, (b) nucleation rate and (c) activation energy as a function of nanowires diameter as reported in Ref.[82].

The high surface-to-volume ratio of nanowires seems to lead to enhanced heterogeneous nucleation that can be responsible for the observed size-depending effects. These results are in contrast with the increase of the crystallization temperature with decreasing thickness reported for thin films in section 3.1.1, but nanowires differ significantly from thin films from many points of view. Their surface-to volume ratio is different and nanowires of Ref.[81] are uncapped while a capping layer is usually deposited for thin films. Moreover, thin films are amorphous as-deposited and it is not possible to reamorphize them after crystallization. So in the amorphous to crystalline transition for thin films the starting point can be only an as-deposited amorphous phase. For nanowires, on the other side, crystallization of a melt-quenched amorphous phase has been studied, so it may be hazardous to directly compare thin films and nanowires results.

It is possible to go even further in investigating the effects of confinement on phase change material by studying PC clusters. Due to the 3D confinement, clusters are the ideal model for investigating the size effects in memory cells where both size and interface effects play a role. Indeed, in clusters the interface effects are enhanced due to the large surface/volume ratio. Moreover, for isolated clusters in a matrix, the plastic relaxation may be limited by confinement, which can thus enhance strain effects.

Some attempts to obtain PC nanoclusters have been reported [83, 84, 85, 86, 87, 88, 89, 90]. The techniques used to fabricate the clusters vary from electron beam lithography to laser ablation and chemical synthesis. For GST nanoclusters made by electron beam lithography with size range from 20 nm to 80 nm, no significant change in the amorphous to fcc phase crystallization temperature has been observed [83]. Smaller clusters (15 nm average diameter) obtained with diblock copolymer transform directly into the hexagonal phase [84]. The growth of GST clusters using laser ablation has been reported, with discrepancies in the reported crystallization behavior. The first results [85] with large size distribution (from 4 nm to 30 nm) indicate that, for 15 nm size-selected clusters, amorphous particles with irregular shape are obtained when the annealing is below 200°C , while crystalline particles are observed when the

annealing is above 300°C . One peculiar observation is the fact that, contrary to bulk or thin films, the hexagonal and fcc phases are formed when annealing is performed at 300°C whereas the pure fcc phase is only observed when annealing is performed above 400°C . A second report, with similar size distribution, indicates clusters with a mixture of amorphous and fcc phase for all temperatures from 100°C up to 500°C [86]. Using a similar growth technique, a third report indicates mostly amorphous as-prepared particles transforming into a mixture of hexagonal and fcc phase after annealing at 100°C , and in a mostly fcc phase after annealing at 200°C [87].

The main conclusion from these studies is that both the cubic fcc and amorphous phases can be observed in nanometric GST clusters. However, the observation of an unambiguous phase transition from an amorphous to a crystalline structure, at a definite temperature, has not yet been achieved. Moreover, in these studies the effect of the cladding material on the phase change properties of clusters has not been addressed. In order to investigate these aspects, GST clusters with size below 10 nm and small size distribution are needed. In the case of GeTe nice results have been obtained using chemical synthesis [88, 89, 90]. Small particles with size ranging from 1.75 to 3 nm show a T_x more than 150°C above that of the bulk, [89] while the increase for 8.7 nm clusters is only 67°C [90]. However, results are difficult to compare to thin films measurements due to the different fabrication methods and to the possibility of carbon contamination of the nanoparticles which could contribute to the observed increase of T_x (see Chapter 2). The chemical synthesis of GST clusters has not been reported up to now. No consistent information have been obtained up to now on the crystallization temperature of PC nanoparticles beyond 10 nm of diameter synthesized by sputtering, which is the deposition method commonly used for thin films deposition.

In conclusion, information in literature about size effect on PC materials rely on studies of thin films, nanowires and clusters. Thin films show a strong dependence of the crystallization mechanism on the interface materials and often exhibit an increase of T_x with decreasing thickness, while nanowires free from capping materials show a decreasing T_x with decreasing diameter. However,

as explained above, it is difficult to interpret the differences observed between films and nanowires without further studies, for example on capped nanowires. Nanoparticles are characterized by a high surface to volume ratio and by a strong influence of capping layers. In the following section the use of a new method for the growth of GST nanometric clusters by sputtering (section 3.2) and their characterization through X-ray diffraction (section 3.3) will be described.

3.2 Clusters deposition

In this section the fabrication and deposition of GST nanometric clusters with average size below 10 nm, embedded in alumina, is described. The process has been done by R. Morel and A. Brenac (INAC/SP2M, CEA Grenoble) [91]. The clusters are prepared in a UHV chamber equipped with a sputtering-gas phase condensation cluster source and two additional standard sputtering guns. The deposition apparatus is depicted in Fig.3.7. The cluster source itself consists in a magnetron sputtering head installed in a liquid nitrogen cooled insert. The stoichiometric $Ge_2Sb_2Te_5$ solid target is DC sputtered in a 0.1 mbar cold argon atmosphere, which makes the sputtered vapor condensate into nanometer-sized clusters. The clusters drift along the gas flow lines and are expelled through an iris diaphragm in the vacuum, forming a beam which is directed onto the sample in a deposition chamber. This chamber is equipped with an additional magnetron that is used for the sputter deposition of GST thin films (using the same target as the one used for clusters), and a second one for the deposition of Al_2O_3 underlayers and capping layers. All depositions are made at room temperature. The clusters size distribution, given by a time of flight mass spectrometer (TOF) , is shown in Figure 3.8a. The average cluster size is 5.7 nm, and the width of the distribution is $\pm$ 1 nm at half maximum. The morphology of the clusters was controlled by Transmission Electron Microscopy (TEM): a low density layer of clusters was deposited on an ultra-thin carbon grid, and protected by a 1 nm Al_2O_3 layer. The TEM image is reported in Figure 3.8b. The distribution of the clusters on the surface is random, as expected from the deposition technique. The particles are spherical. The fact that no atomic planes

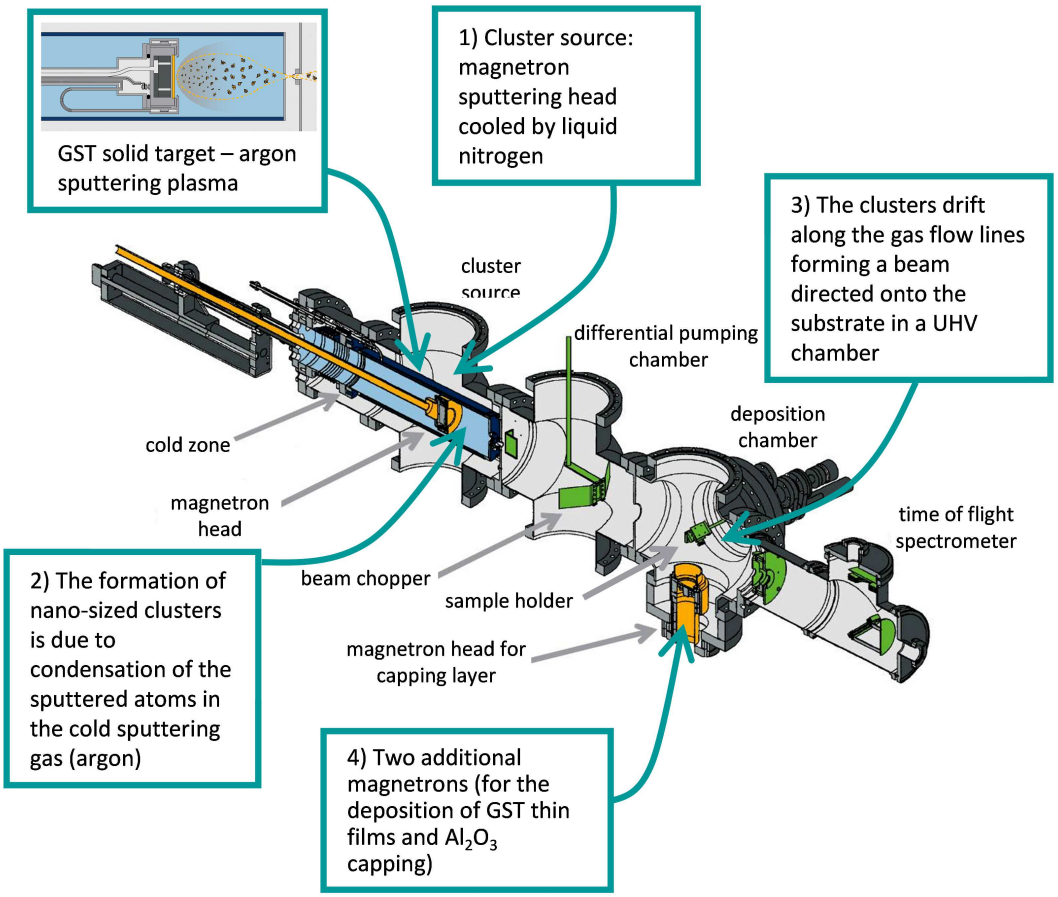

Figure 3.7: Schematic drawing of the apparatus used to deposit the nanocluster samples as long as the thin film samples used for comparison. The deposition procedure is briefly illustrated.

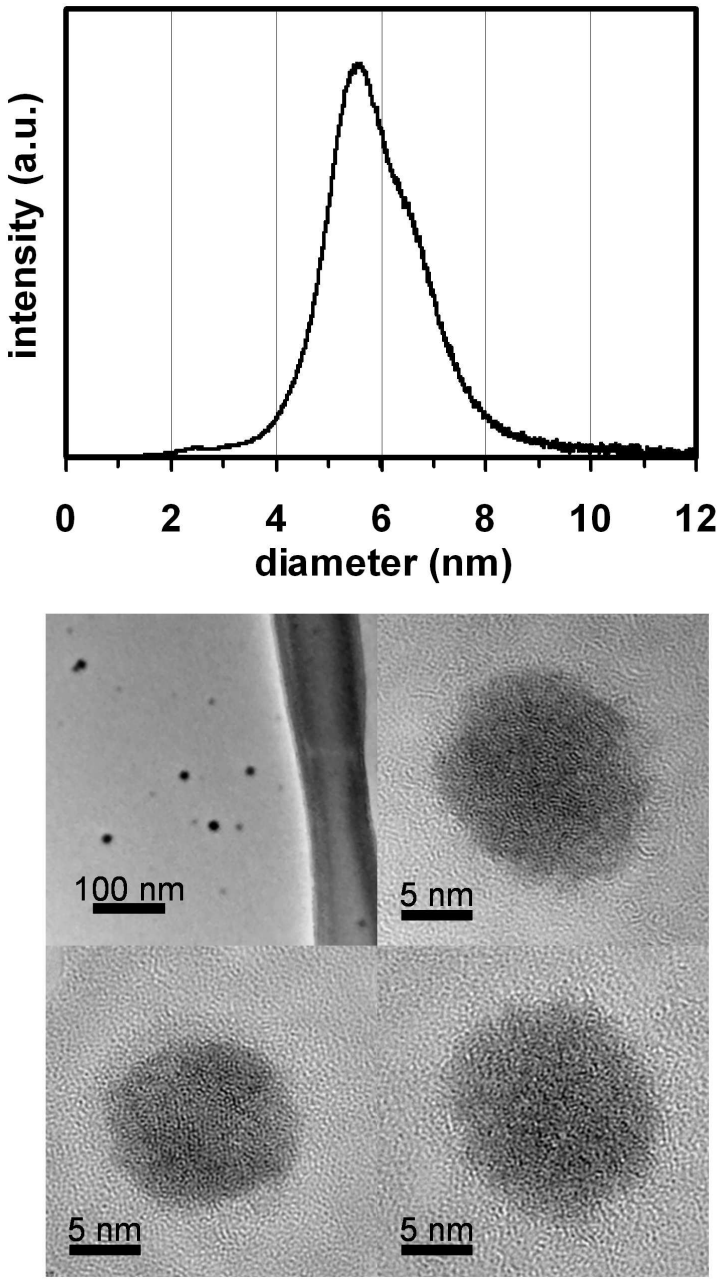

Figure 3.8: (a) TOF size distribution which shows that the nanoclusters have an average diameter of 5.7 nm with a narrow size distribution (± 1 nm at half maximum) (b) TEM images of GST as-deposited clusters which indicate that the particles are spherical and amorphous. These images have been made on a low density dedicated sample and the clusters state and shape have been checked over clusters with the largest diameter. (By courtesy of M. Audier, LMGP CNRS, Grenoble INP-Minatec

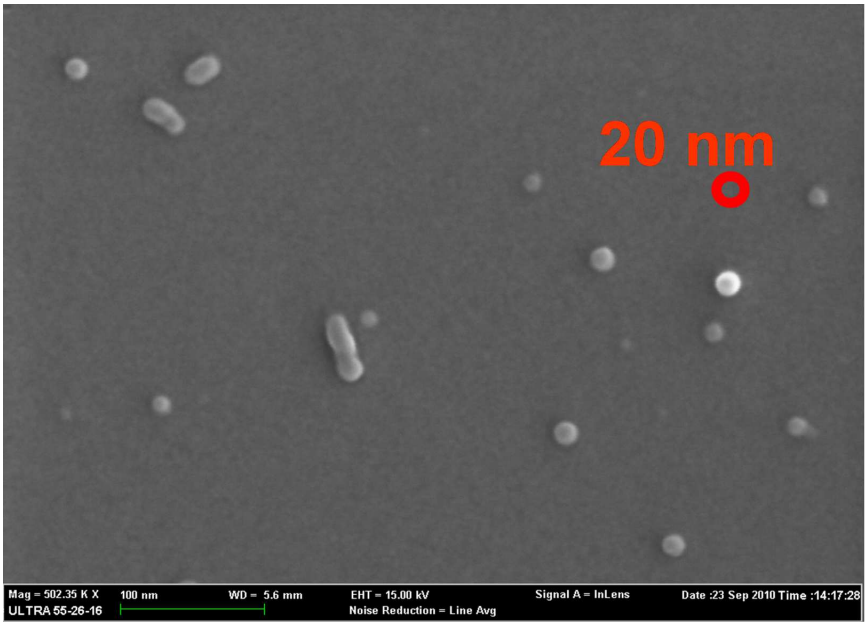

Figure 3.9: Scanning Electron Microscopy (SEM) image of GST deposited clusters. The red circle has a diameter of 20 nm. No trace of particles coalescence can be seen.

are visible for the clusters and that the contrast is similar for all particles is a first indication that the as-deposited clusters are amorphous, as will be demonstrated with the X-ray diffraction analysis. In Figure 3.9 a Scanning Electron Microscopy (SEM) image of the same sample shows no sign of coalescence of the deposited particles.

Two types of GST samples have been prepared in order to perform the X-ray diffraction (XRD) measurements. The GST clusters samples consist in 4 GST clusters layers deposited on Si. First a layer of 6 nm of Al_2O_3 has been deposited on the Si substrate. Then a layer of GST clusters with an equivalent mass of 0.07 monolayer of particles has been deposited, covered with a 3 nm Al_2O_3 layer. Then, three other layers of GST clusters have been deposited, each one covered by 3 nm of Al_2O_3 , and at the end a 6 nm Al_2O_3 layer has been deposited. The final structure, shown in Fig. 3.10a, is 6 nm Al_2O_3 / (GST clusters layer / 3 nm Al_2O_3) $\times$ 4 / 6 nm Al_2O_3 . The average distance between clusters is two cluster diameters. This structure has been chosen in order to avoid sintering effects during annealing. The GST film samples consist in 10 nm GST thin film sandwiched between two 10 nm thin Al_2O_3 films, deposited on a Si substrate.

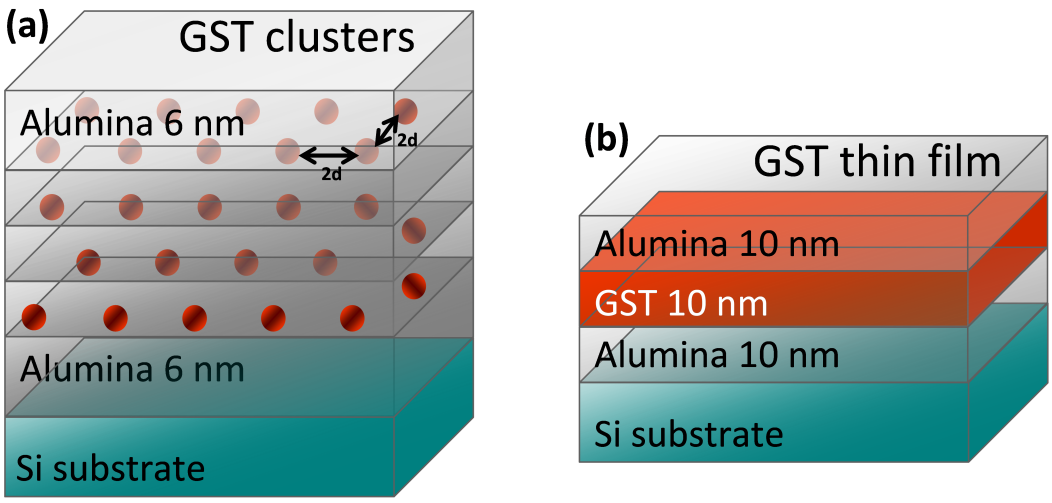

Figure 3.10: (a) GST clusters sample: 4 layers of clusters capped with Al_2O_3 are deposited on an Al_2O_3 substrate and capped again with Al_2O_3 . The average distance between clusters in a layer is about 2 cluster diameters. (b) GST film sample: 10 nm thick film of GST sandwiched between two 10 nm thin Al_2O_3 films. Both the clusters and film samples are deposited on a substrate of Si.

Their schematic representation is reported in Figure 3.10b. The GST quantity in clusters samples is five times less than the one in film samples. A 20 nm Al_2O_3 thin film on a Si substrate, hereafter called blank sample, was also grown for background signal measurement in the X-ray diffraction experiments. Thin films and clusters compositions were measured with Rutherford Backscattering Spectroscopy (RBS) and Particle-Induced X-ray Emission (PIXE). For thin films the content is Ge:Sb:Te = 23:24:53 ($\pm$3), very close to the $Ge_2Sb_2Te_5$ = 22:22:56 target composition. For the clusters the composition is 28:27:45 ($\pm$3), which indicates a slight Te depletion as often reported for very thin films and clusters [70, 83, 86, 92]. Within experimental accuracy, the GST clusters composition is found identical before and after annealing.

3.3 X-Ray Diffraction study

In order to qualitatively locate T_x and observe the crystallized state in clusters a first set of clusters samples was annealed under vacuum ($10^{(} - 3$) bar) at 200°C and 300°C , while a film sample was annealed at 200°C . The tempera-

ture was ramped at + 10°C /min, held at the set point temperature for 30 min, and ramped down to ambient temperature. X-ray diffraction on those samples, hereafter referred to as ex situ samples, has been performed at room temperature. For a second set of clusters and thin films samples the X-ray diffraction spectra were recorded as a function of the temperature, during the annealing process. Those samples will be referred to as in situ samples. X-ray diffraction measurements were performed using synchrotron radiation on the BM02 CRG-D2AM beamline (ESRF Grenoble, France) with a photon incident energy of 17.8 keV (λ =0.69654 $\mathring{A}$) and using a 2D CCD camera detector. The detailed description of the experimental setup is reported in appendix A.2.2. The incident angle was 4° and the position of the CCD camera allowed for measurements in a 2θ range from 8° to 26°. As it is reported in details in appendix A.2.2 about the data treatment description, the contribution of the Si substrate and deposited Al_2O_3 are very intense compared to the GST signal. These background contributions need to be subtracted from the measured diffracted signal. For this purpose, the blank sample (Si + Al_2O_3) has been measured. The 2D image obtained for the as-deposited GST film sample, after removing the background, shows only faint traces, with no diffraction rings. This is a first confirmation that the as-deposited GST film is amorphous. The 2D image of the 200°C ex situ annealed thin film sample, again after background subtraction, shows diffraction rings which can be indexed as a fcc structure with a (111) texture (Figure 3.11a).

Concerning the as-deposited clusters, the X-ray diffraction 2D image shows no diffraction rings. For the 200°C annealed clusters, supposing a cubic structure, the (111) and (222) diffraction rings are not observed but a weak signal is visible for the (200) and (220) diffraction rings (Figure 3.11b), which are the two most intense reflections expected in a powder diffraction pattern from the bulk fcc phase. The intensity is constant over all the measured rings portions. A diffuse scattering from the Si substrate is still present at the corners of image Fig.3.11b, showing that the background subtraction is not perfect[1].

[1]This could be related to the fact that the relative contributions of the Al_2O_3 signal and Si signal are not the same in the blank sample and in presence of GST. This problem could

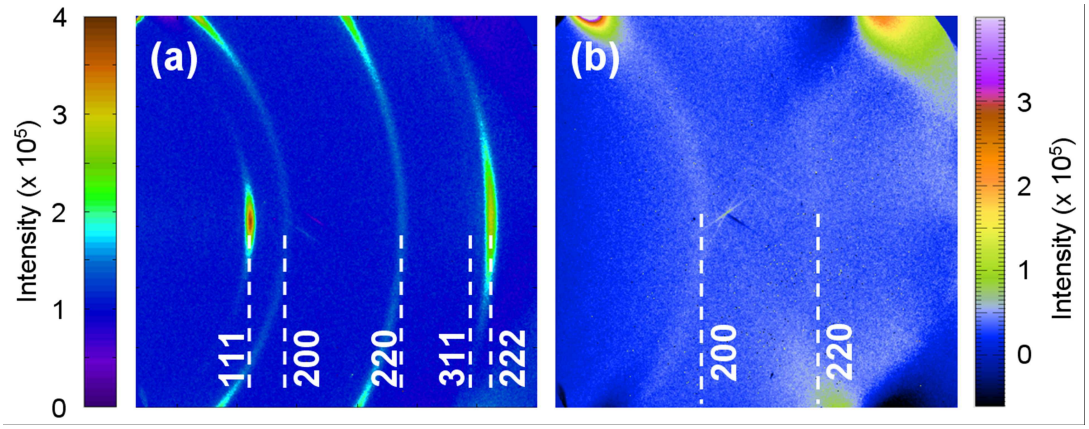

Figure 3.11: (a) X-ray 2D diffraction images for 200°C ex situ annealed GST thin film. (b) Same measurements for 200°C ex situ annealed clusters. In both cases, the 2D image of the blank sample (Si+Al_2O_3) has been subtracted.

The 2D images give information about the samples texture and traces of Bragg peaks can be detected directly on them, but the evidence of the phase transformation and the position for the diffraction lines are more clearly observed by measuring the angular integrated intensity, in particular for clusters. The intensity as a function of 2θ has been obtained by integrating over the entire 2D images for each sample, excluding only a border of 100 pixels on each side, thus losing information on texture in the film case. The background integrated intensity has always been subtracted. The angular integrated intensity for the film sample is shown in Figure 3.12. For the as-deposited film the clear observation of two broad maxima at $2\theta = 12.9°$ and 21.6° allows to conclude that as-deposited clusters are amorphous. Their positions, corresponding to $Q = 4\pi\sin\theta/\lambda$ =2.03Å^{-1} and 3.38 Å^{-1}, match the first two maxima of the GST amorphous structure factor reported in literature [27] (see Chapter 2). For the annealed film the peaks positions indexed in the fcc cubic structure indicate a lattice parameter of 6.01 ± 0.01 Å that closely matches the one reported for bulk GST, 6.0117(5) Å [25]. It should be noticed that due to the texture and the finite angular range the relative integrated intensity for the peaks is not the one expected for a powder pattern. Such intensity is reported in Table 3.2 as calculated considering the lattice parameter for GST given in Ref. [25].

not be solved after the experience took place.

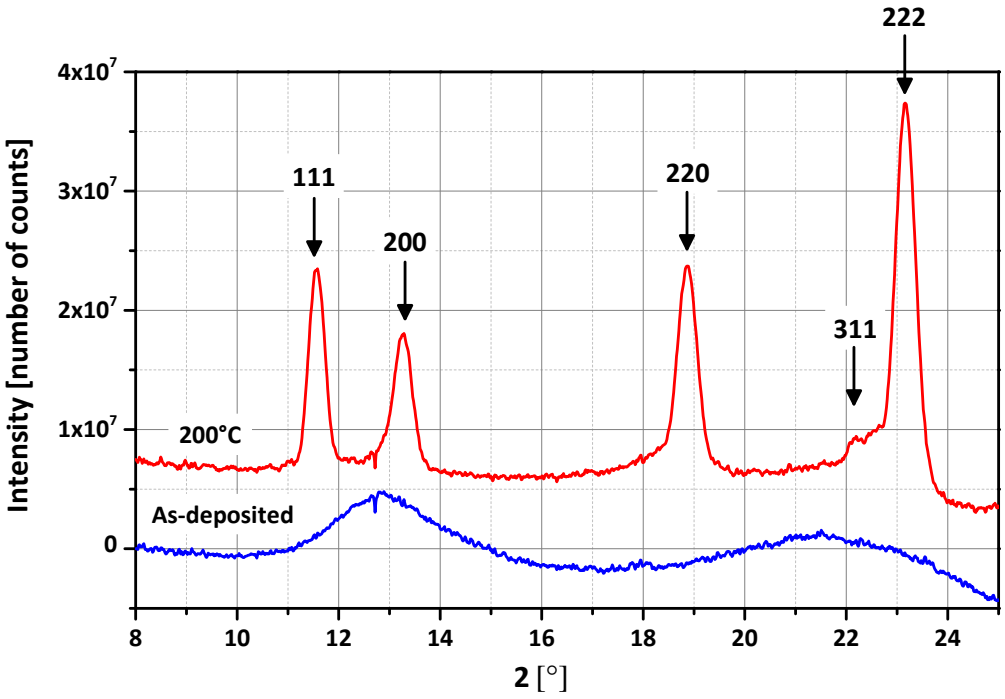

Figure 3.12: X-ray diffraction spectra at room temperature for as-deposited and 200°C ex situ annealed GST film, after background subtraction, with curves shifted for clarity. Arrows indicate bulk GST fcc peak positions calculated assuming the lattice parameter of GST a=6.0117 Å reported in Ref.[25].

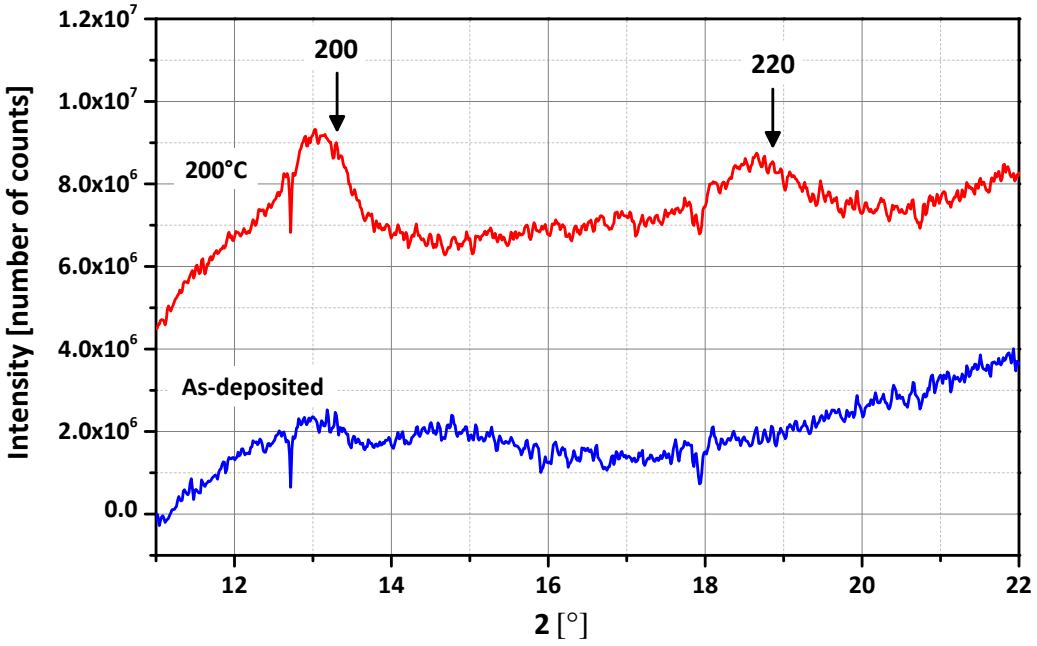

Figure 3.13: X-ray diffraction spectra at room temperature for as-deposited and 200°C ex situ annealed GST clusters after background subtraction. Curves are shifted for clarity. Arrows indicate bulk GST fcc peak positions calculated assuming the lattice parameter of GST a=6.0117 Å reported in Ref.[25].

hkl	$2\theta[^\circ]$	$d[\mathring{A}]$	I_{rel}
111	11.518	3.47086	4.25
200	13.307	3.00585	61.18
220	18.862	2.12546	100.00
311	22.155	1.81260	8.62
222	23.154	1.73543	57.35

Table 3.2: Peak positions and relative intensities for the fcc GST phase as expected from a powder pattern. They have been estimated in a $\theta - 2\theta$ geometry at the actual experimental wavelength considering the lattice parameter a=6.0117 Å reported in Ref [25].

The angular integrated intensity obtained for ex situ clusters samples is reported in Fig. 3.13. The as-deposited sample shows no clear trace of the amorphous broad maxima that can be identified for the as-deposited film sample, as can be understood in view of the smaller quantity of GST in clusters samples. As expected, due to the smaller crystallite size, the peaks width for the 200°C annealed cluster samples are larger than for the thin film. Besides, a clear shift of the diffraction lines with respect to their position in the crystalline thin film is observed.The fcc lattice parameter for the crystalline clusters calculated from the (200) and (220) peaks position is 6.11 Å ± 0.02.

In order to measure T_x more precisely the 2D X-ray diffraction spectra for as-deposited thin films and clusters were recorded as a function of the temperature, with in situ annealing using a domed oven stage. More details on the experimental setup and data treatment can be found in appendix A.2.2. These measurements are challenging due to the temperature dependent spurious signal from the oven dome that reaches more than 10^9 counts, two orders of magnitude higher than the film signal and even three orders of magnitude higher than the clusters signal. Nevertheless, the crystallization of the amorphous as-deposited clusters could be observed. The temperature was increased by 10°C steps after which X-ray diffraction spectra were recorded for 26 min.

The change in the thin film (220) diffraction peaks from 150°C to 180°C is plotted in Figure 3.14. Despite the deterioration of the signal over noise ratio in presence of the dome covering the oven, it is clear that the peak intensity

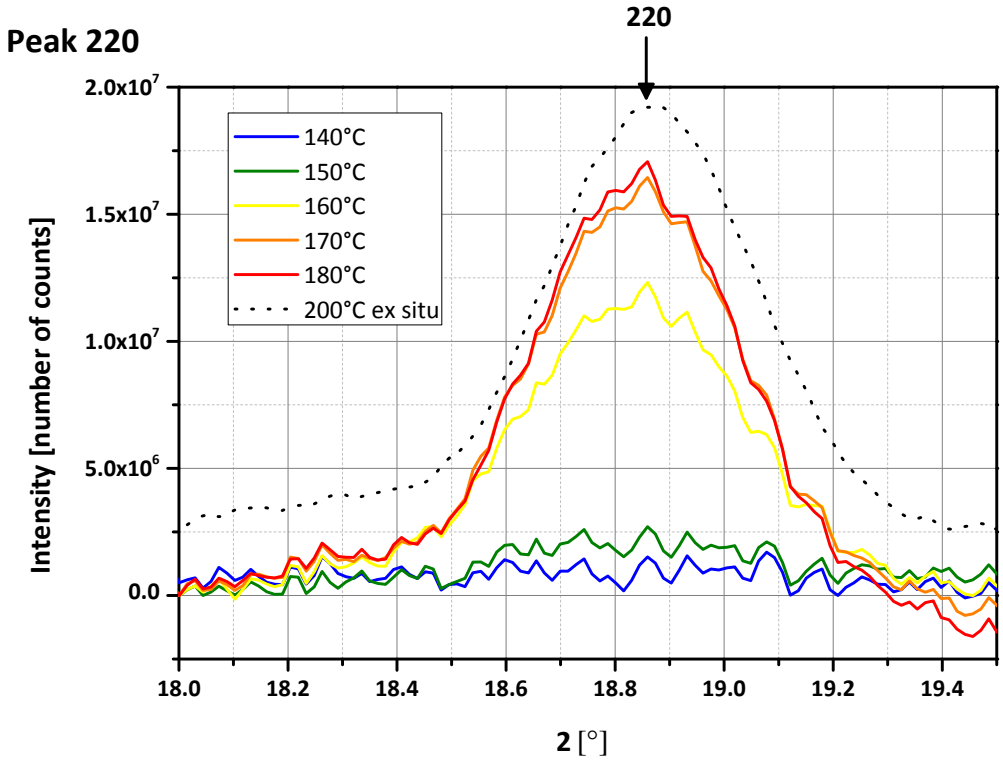

Figure 3.14: (220) diffraction peak for in situ annealed GST thin film at different temperatures. The dotted line is the peak, measured at room temperature, of the thin film annealed ex situ at 200°C (shifted for clarity). The arrow indicates the calculated bulk GST peak position.

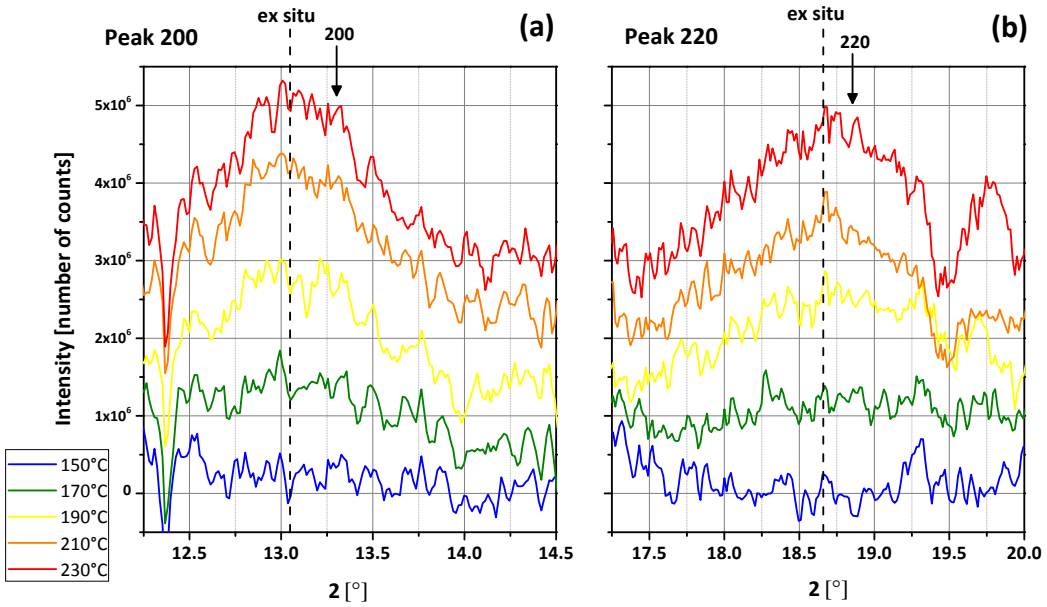

Figure 3.15: X-ray diffraction spectra for in situ annealed GST clusters at different temperatures. (a) (200) diffraction peak and (b) (220) diffraction peak. Curves are evenly shifted to ease viewing. Dotted lines indicate the peak position, measured at room temperature, of the 200°C ex situ annealed clusters.

measured at 180°C is comparable with that measured at room temperature for the sample annealed ex situ at 200°C . At 150°C no signal is recorded above background level, while at 170°C the crystalline peak is close to its final amplitude. It can be observed that the (220) peak position at 180°C is slightly below that of the ex situ annealed thin film measured at room temperature, which can be explained by the GST thermal dilatation [93, 94]. Considering a coefficient of thermal expansion for $Ge_2Sb_2Te_5$ of $\alpha_T = 1.81 \cdot 10^{-5} K^{-1}$ [94] and the relation $d = d_0(1 + \alpha_T \cdot \Delta T)$ for the thermal expansion of the interatomic distances, 2θ is expected to vary of 0.05° between the room temperature and 200°C .

The (200) and (220) diffraction peaks for in situ annealed clusters are shown in Figure 3.15. Despite the high noise level and remaining contribution from the oven dome at 2θ=19.5°(Fig. 3.15b), the parallel rise in the amplitude for the two peaks is visible. In order to make a more quantitative analysis the area of the peaks has been integrated as a function of temperature[2]. Considering the

[2]Integration is restricted to the left part of the 220 peak in order to avoid the remaining spurious signal of the dome.

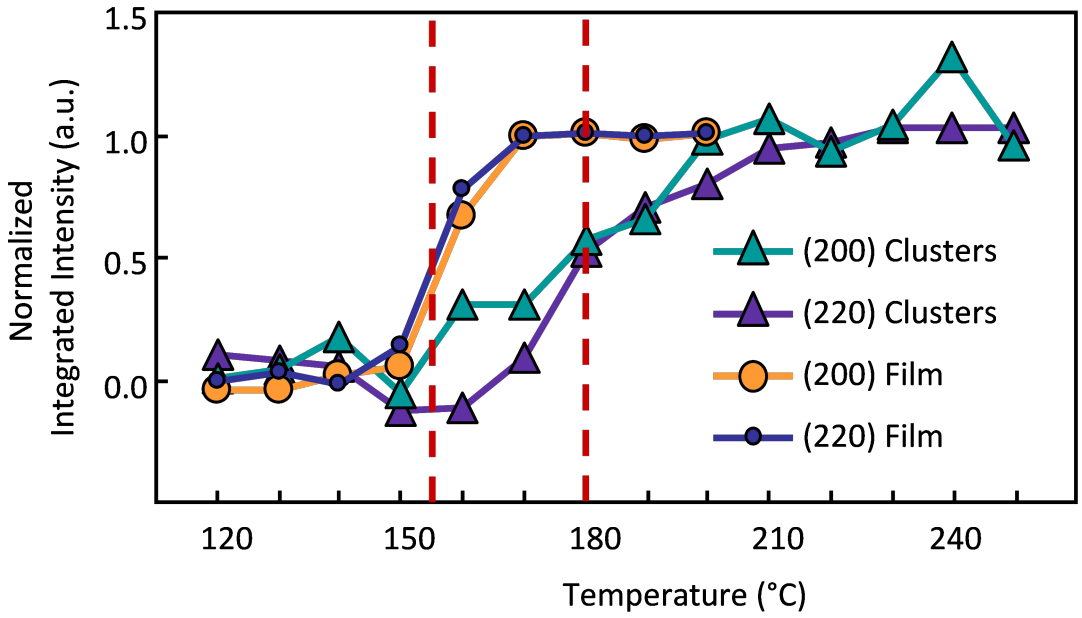

Figure 3.16: Normalized integrated intensities for (220) and (200) diffraction peaks for GST clusters and for GST film as a function of temperature. The normalized integrated intensities have been obtained through the relation $I_{norm} = I/I_{max}$ where I is the measured integrated intensity at a given temperature and I_{max} is the maximum value of the integrated intensity (which correspond to complete crystallization). The dotted lines indicate the crystallization temperatures.

different values of the peak maxima for film and clusters samples, the obtained integrated intensities have been normalized through the relation $I_{norm} = I/I_{max}$ where I_{norm} is the normalized integrated intensity and I_{max} is the maximum value of the integrated intensity (which corresponds to complete crystallization). All these intensity are measured at a given temperature. I_{norm} corresponds to the crystalline fraction, thus allowing a direct and clearer comparison between clusters and film. The crystallization temperature is defined as the temperature corresponding to the midpoint of the rise step of I_{norm}. The results are shown in Figure 3.16.

For the thin film the rise is almost parallel for the (220) and the (200) peaks. No crystallization occurs at temperature lower than 140°C . The value of T_x is 155°C and the crystallization is completed at 170°C . For the clusters, crystallization starts at around 150°C , T_x is close to 180°C and the rise in amplitude is more gradual, spanning from 150°C up to 200°C .

3.4 Discussion

The most important result obtained from the ex situ cluster samples is the confirmation that the nanoparticles are able to switch from the amorphous to the crystalline fcc phase when annealed. So, even for particles with a diameter as small as 5 nm, the phase change mechanism still takes place. This result is positive for the future developments of Phase Change Memories.

A second key observation regarding the annealed crystalline clusters is that the lattice parameter obtained from the measurements is larger than that of the annealed fcc thin films, the latter being very close to the one expected for the GST fcc cubic phase. For thin films, Scherrer analysis gives a lower limit for the crystallite size [95] close to the layer thickness and a small inhomogeneous strain of 0.006. These films are close to complete relaxation. On the other hand, the shift in the crystalline clusters peaks position indicates that the lattice parameter for the fcc clusters (6.11Å) is 1.7% larger than that of the crystallized thin film (6.01Å), which can be attributed to a large tensile strain due to the interaction with the oxide matrix[3]. At the phase change transition, the GST density decreases by 5% [25, 94]. In thin films, the stress resulting from the volume change can be relaxed along the two space directions that are not stuck to the surrounding layers, whereas clusters are bound to the surrounding matrix in all three dimensions. Upon crystallization, the deformation must be accommodated one way or another. This can be for instance via the creation of voids [96, 97] or vacancies [98] or strain. In the present case, the observed homogeneous tensile strain is very close in absolute value to the reduction in size that would be expected for freestanding clusters during the amorphous to crystalline phase change. Indeed, the variation of the lattice parameter estimated for clusters compared to the thin film $\frac{\Delta\ a}{a} \approx 1.7\%$ corresponds to a relative volume variation $\frac{\Delta\ V}{V} = (\frac{\Delta\ a}{a})^3 \approx 4.9\%$. This suggests the scenario represented schematically in Fig.3.17. When an amorphous cluster switches to the crystalline phase the strong interaction with the embedding alumina, which is a far more rigid

[3]In crystalline clusters, there are only two peaks that can be analysed. A Sherrer analysis with no inhomogeneous strain leads to a grain size in agreement with the clusters diameter. Therefore, inhomogeneous strain effects in clusters will not be considered.

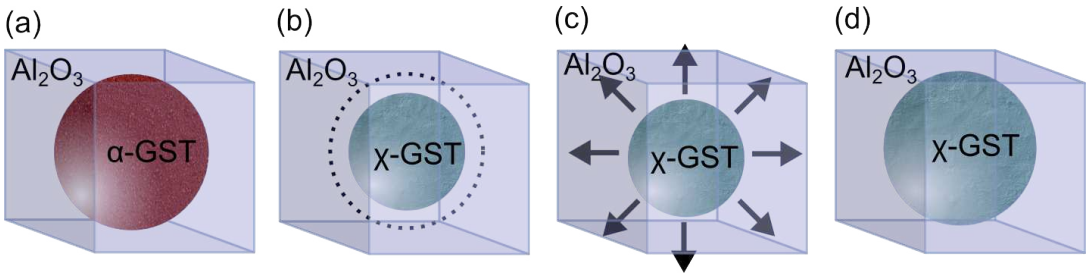

Figure 3.17: The Al_2O_3 matrix surrounding the cluster forces its volume to remain equal to the one of the amorphous phase even after crystallization. The cluster in its amorphous phase occupies a certain volume (a). When crystallization occurs, the cluster volume tends to reduce of around 5% (b), but the embedding Al_2O_3 matrix exerts a tensile strain over the cluster (c) thus forcing the cluster to keep the volume corresponding to the amorphous phase, with the effect of increasing the lattice parameter of the crystalline cluster (d).

material than GST, forces it to keep the volume that it had in the amorphous phase.

As already stated, there are no clear reported values of the crystallization temperature for GST nanoclusters of such small diameter in literature. Nevertheless, it seems quite natural to compare our results with those reported in Ref. [70] on GST thin films embedded in Al_2O_3 , which is the same cladding material used in this study. The T_x obtained for the thin film in this work (155°C) is in agreement with the value reported in Ref.[70] for a GST film of similar thickness. On the other hand, the T_x in the case of clusters is only 25°C above T_x of the 10 nm thick GST thin film, an effect much smaller than reported in Ref.[70] where a thin film of 5 nm shows a T_x of more than 330°C . However, the different surface to volume ratio can have a deep influence on the crystallization mechanism, making difficult a direct comparison between clusters and thin films scaling properties. Moreover, a film is free to change its volume upon phase transformation while clusters are confined in three dimensions and strained, as shown above. The strain may possibly play a role in promoting or impeding crystallization. However, no data about the deformation or strain of measured films are available in Ref. [70], thus impeding to compare strain effects. In Ref. [72] an effect of stress over crystallization has been addressed, but the variation on lattice parameters due to strain has not been measured so again a comparison is hazardous.

As shown in section 3.1.1, it is very difficult to discuss effects on the crystallization temperature since a wide number of factors plays a role. However, considering that in the present case the GST clusters, the GST film and the Al_2O_3 capping have been deposited in the same apparatus and measured in identical conditions it is possible to try to interpret the observed 25°C variation of T_x between thin film and clusters. It could be related to many different factors including composition effect, different surface to volume ratio, matrix influence, stress or strain effects or an intrinsic size effect. A possible composition effect could arise from the fact that, as compared with the films, the clusters are Te-depleted. For instance the crystallization temperature in Ge-Sb-Te thin films with 10%-20% excess Sb is 15°C higher than for GST films [99]. The crystallization temperature for $Ge_2Sb_2Te_4$ is 175°C [100].Another effect could be the stress resulting from the phase change. From a thermodynamical point of view the elastic energy stored in clusters will reduce the driving force for the phase transition. The kinetics for the phase change will be slowed and, during a temperature scan, the transition temperature will increase. In the case of GST this driving force is 200 MJ/m^3, [101]. An order of magnitude for the elastic energy resulting from the strain is close to 50 MJ/m^3, considering the experimental value of the bulk modulus available in literature [102], so it can induce significant effects. Finally, the increase of T_x could be an intrinsic size effect due to the impact of surface energy as explained through Zacharias model [71], even if the effect is much smaller than what reported in Ref.[70] for GST thin films capped with Al_2O_3 .

As already mentioned at the end of section 3.3, the crystallization of clusters is more gradual than the one of the 10 nm film. This can be due to a dispersion of the crystallization temperatures of clusters. If T_x increases for reduced dimensions due to a size effect, smaller clusters will have a higher T_x so the crystallization temperature dispersion is a consequence of the size distribution. However, it is also possible to have a dispersion of T_x even for clusters of the same size, due for example to oxidation of the clusters at the Al_2O_3 interface which can change the composition and influence T_x . It is also worth noting that, supposing an homogeneous nucleation and considering that the clusters

size is quite close to the critical nucleus diameter (about 2 nm), a dispersion of T_x could occur from cluster to cluster.

3.5 Conclusions and perspectives

In conclusion, nanometric GST clusters were deposited by a sputtering gas-aggregation technique, with a narrow size distribution around 5.7 nm. The obtained results demonstrate that this synthesis technique offers new possibility for the study of well calibrated and isolated clusters of phase change materials, opening the way to a systematic study of nanoparticles deposited by sputtering. It offers the same reduced dimensions and size distribution as chemical synthesis but with the possibility of depositing ternary compounds (this is still very difficult with chemical techniques) and with a much smaller risk of including contaminants. Moreover, this method is close to the physical techniques used for PC film deposition in the fabrication of PCM, thus giving information that can be more directly exported to device fabrication. The as-grown clusters dispersed in alumina are amorphous and transform into a fcc crystalline phase at a well defined crystallization temperature of 180°C . This is the first unambiguous observation of this phase change in GST clusters in the sub-10 nm range. The crystalline clusters show a lattice parameter larger than that of bulk cubic GST, which indicates a tensile stress that can be attributed to the interaction with the alumina matrix. The large increase in T_x observed in thin GST films subjected to large interface stress [72] is not seen in clusters. These results indicate that the scaling effect on the crystallization temperature in phase change material can be small and the role of interfaces in term of stress and interfacial energy effects must be further studied.

All the results reported in this section have been obtained from a single experience at the synchrotron that was done over the first set of GST clusters samples obtained with this deposition method. This experience allowed to learn how to improve the data acquisition and subsequent analysis. For the next experiences the quantity of matter in clusters samples should be increased in order to obtain more intense signals, improve the quality of the data and reduce

the effort for the data treatment that was difficult and time consuming. The blank sample needs to be deposited with the same amount of cladding material as the PC samples in order to avoid errors in subtracting the substrate contribution.

In the near future the same deposition technique will be used to deposit GeTe nanoparticles. Besides, based on the results presented in Chapter 4, the effect of different capping layers as Ta, TiN, W or SiO_2 will be also investigated. Smaller clusters could also be deposited, but their size distribution would be larger. A further step will be the electrical characterization of clusters in order to determine their electrical properties such as threshold voltage, retention time, reset current and cyclability. Doped clusters can also be deposited in order to study the effect of doping at small sizes, and to evaluate the impact of the variability of doping concentration in such small systems. To go further, local order investigations and TEM measurements can be done in addition to XRD measurements in order to completely characterize the structure of clusters.

Chapter 4

Interface effect on crystallization of PC thin films

4.1 Introduction

As already mentioned in section 3.1.1, the material used as a capping layer has been shown to have an influence on the crystallization mechanism of a phase change very thin film. Even for films as thick as 30 nm the same Ge-Sb-Te compound tested under the same conditions crystallizes at a different temperature if interfaced with different materials such as silicon dioxide SiO_2 , silicon nitride Si_3N_4, tantalum oxide Ta_2O_5, zinc sulfide ZnS or $ZnS - SiO_2$ [66], or, even when the value of T_x is unchanged, the crystalline phase and growth rates of the same PC material can be different if capped with Si_3N_4 or $ZnS - SiO_2$ [77]. For film of GST and GeTe of larger thickness, the effect of interfaces is assumed to be absent and the measured T_x is considered as the bulk crystallization temperature.

In this chapter a study on the effect of different interfaces on the crystallization temperature of a PC material thin film will be reported. The value of T_x will be measured through reflectivity measurements (section A.1) and X-Ray Diffraction measurements (XRD) (sections 4.3 and 4.4), and a possible interpretation of the results will be proposed at the end of the chapter (section 4.5). The samples tested though reflectivity consist in thin films of GeTe and GST of various thicknesses encapsulated in three different materials, TiN, Ta or SiO_2 . Those test materials have been chosen as capping layers because they are frequently employed in the fabrication process of devices (TiN and Ta for the electrodes and SiO_2 as insulating material), so they can be eventually integrated in a cell. The structure of the samples, shown in Fig. 4.1, is the same for both GeTe and GST samples. The XRD experiments have been performed on GeTe thin films 100 nm thick only. All the phase change materials and capping layers have been deposited by sputtering as described in appendix B. The measured composition of the GeTe samples is $Ge_{52}Te_{48}$. The experimental procedures and setups are described in details in appendix A.2.

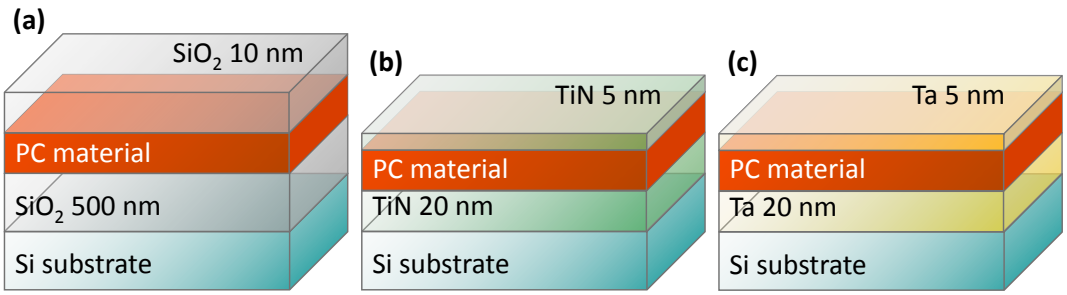

Figure 4.1: Structure of PC material thin films samples used in order to investigate the interface effect on crystallization. The PC material can be either GeTe or GST, of various thicknesses, sandwiched between (a) SiO_2 , (b) TiN or (c) Ta. All the samples have been deposited by sputtering as described in B.

4.2 Reflectivity measurements

The reflectivity as a function of temperature of 100 nm thin films of GST and GeTe sandwiched between TiN, Ta or SiO_2 is shown in Figure 4.2. The heating rate was 10°C /min for all the samples. The amorphous to crystalline phase transition corresponds to an increase in the value of the measured reflectivity. It is evident from Fig. 4.2 that for both GST and GeTe the phase change occurs at similar temperatures when the film is sandwiched between TiN or SiO_2 , while the transition occurs at a higher temperature when the PC material is interfaced with Ta. This is a surprising result. Even if an effect of the encapsulating material on T_x has been observed in literature for films of 30 nm [66] it was very small, while in the present case we observe a difference of more than 20°C even for films 100 nm thick. The crystallization temperatures T_x for the six samples of Fig. 4.2, calculated as the point of maximum derivative of the reflectivity curve, are reported in Table 4.1. The difference between the crystallization temperatures obtained with the TiN or SiO_2 interfaces is small both for GeTe and GST samples, and it is within the uncertainties on the sample temperature in the reflectometer [1]. The resulting values of T_x for GST interfaced with SiO_2 and TiN are close to the T_x reported in literature for

[1] As described in details in appendix A.1, the temperature in the reflectometer is measured on the heating plate. If the thermal contact between the heating plate and the sample is not perfect the actual temperature on the sample can differ from the measured one.

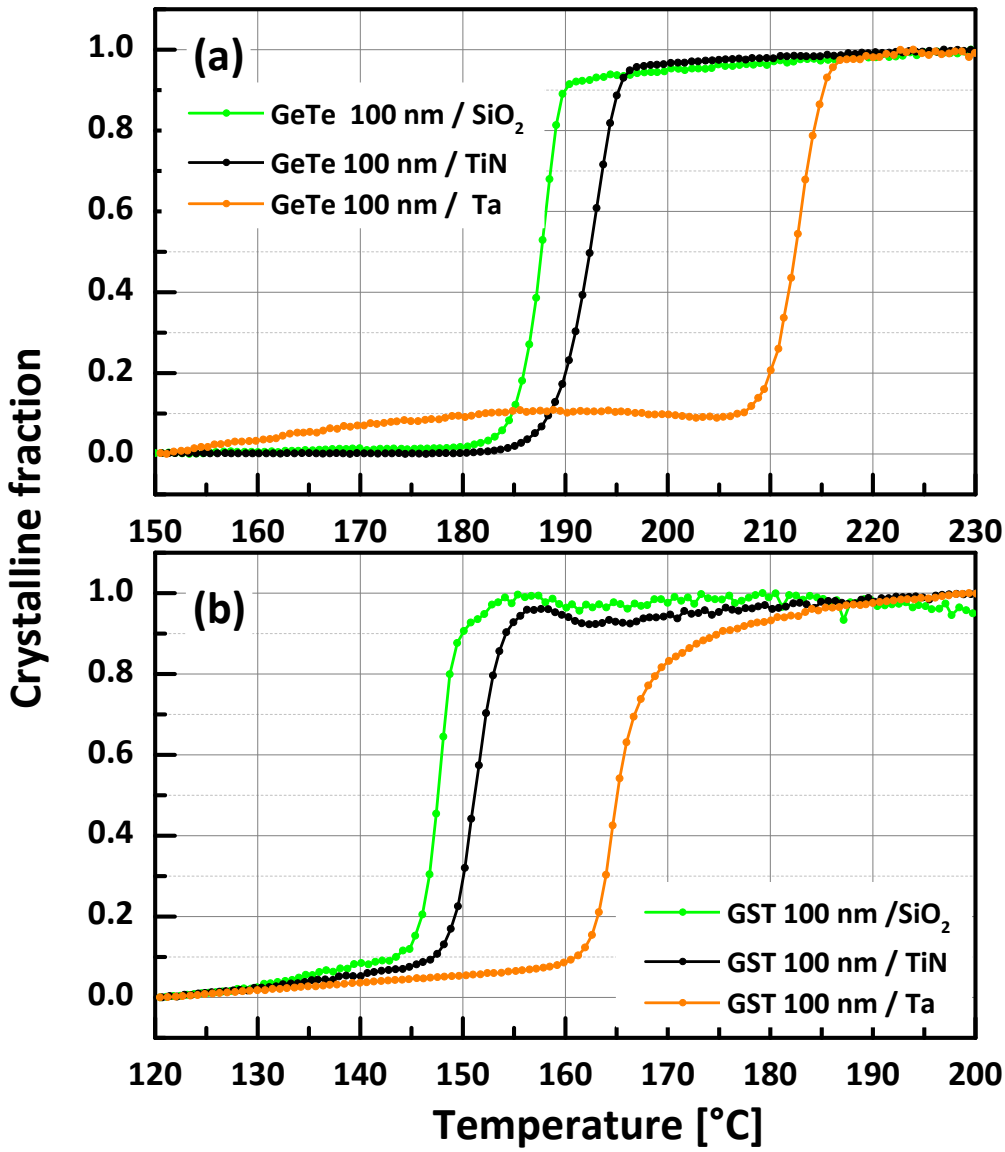

Figure 4.2: Crystalline fraction as a function of temperature obtained from reflectivity measurements for (a) GeTe and (b) GST 100 nm thin films sandwiched between TiN, Ta or SiO_2 heated at 10°C /min. For both GeTe and GST thin films the amorphous to crystalline transition occurs at a higher temperature when the film is sandwiched between Ta.

	GeTe 100 nm T_x [°C]	GST 100 nm T_x [°C]
SiO_2	188	148
TiN	193	152
Ta	213	165

Table 4.1: Crystallization temperatures T_x of GeTe and GST 100 nm thick films sandwiched between TiN, Ta or SiO_2 as obtained from the reflectivity measurements of Fig. 4.2 for a heating rate of 10°C /min.

30 nm thick films of GST interfaced with SiO_2 and ZnS-SiO_2 characterized by transmittance measurements and resistance measurements [66, 67]. They are lower than what reported for TiN interfaced GST measured by EXAFS and ellipsometry in Ref.[72] and for GST interfaced with Al_2O_3 and measured by X-Ray Diffraction [70], but in this last case the heating rate is six times higher than in our experiments. The values of T_x obtained for GeTe films interfaced with SiO_2 and TiN are in agreement with what reported in Refs.[23] and [44] for thin films measured under the same condition as in this work at a heating rate of 20°C /min and 10°C /min, respectively. A T_x of 175°C has been reported in Ref.[103] for resistance measurements on a GeTe film 50 nm thick interfaced with SiO_2 heated at 1°C /s and a T_x of 170°C has been reported in Ref.[104] for a GeTe film 75 nm thick interfaced with polymethyl methacrylate heated at 23°C /min and measured by optical transmission measurements.

The same reflectivity measurement has been repeated on samples of GeTe 30 nm and 10 nm thick interfaced with TiN, Ta or SiO_2 and the results are shown in Fig.4.3. For the 30 nm thick samples the change in reflectivity can be easily identified for each kind of interface, and the difference in T_x observed for the 100 nm thick films between the Ta interfaced samples and the others is still clearly evident. For the 10 nm thick GeTe films the phase transition for the SiO_2 interfaced sample is still evident, but the interpretation of the reflectivity measurement becomes difficult for the TiN and Ta interfaced samples due to the high contribution of the upper layer of TiN or Ta, that could not be subtracted. However, a phase change can still be observed for the TiN interfaced sample. On the other hand, no reflectivity change could be detected for the Ta interfaced

	GeTe 30 nm T_x [°C]	GeTe 10 nm T_x [°C]
SiO_2	191	197
TiN	187	211
Ta	223	>230

Table 4.2: Crystallization temperatures T_x of GeTe films 30 nm and 10 nm thick sandwiched between TiN, Ta or SiO_2 as obtained from the reflectivity measurements of Fig. 4.3 for a heating rate of 10°C /min.

sample in the experimental temperature range up to 230°C . It could be due to the fact that T_x for that sample is above 230°C , but no definitive conclusion can be drawn in view of the difficulties of the reflectivity measurements. The values of T_x for the 30 nm and 10 nm thick GeTe samples are shown in Table 4.2. For the 30 nm thick films, the difference of T_x between the Ta interfaced sample and the others is around 30-35°C , while it was around 20-25°C for 100 nm thick GeTe films. By comparing Tables 4.1 and 4.2 it can be concluded that reducing the film thickness has a weak effect on T_x for the SiO_2 interfaced samples, while T_x seems to increase with deacreasing thickness for the samples interfaced with TiN and Ta. Indeed, the 100 nm and 30 nm TiN interfaced samples have the same T_x , while T_x increases of around 20°C for the 10 nm thick film. The T_x of Ta interfaced GeTe samples increases of around 10°C when the film thickness is reduced to 30 nm and no phase transition can be seen up to 230°C for the GeTe film 10 nm thick.

The activation energy E_A of the GeTe 100 thin film has been calculated for the SiO_2 and Ta interfaced samples by repeating the reflectivity measurement for three other heating rates: 3°C /min, 5°C /min and 20°C /min. The crystallization temperatures T_x obtained for all different heating rates are reported in Table 4.3. The values of E_A obtained by fitting the set of points shown in Fig. 4.4 (as described in section 1.3.5) are of 3.83 eV for Ta interface and 2.58 eV for SiO_2 interface. The activation energy obtained for GeTe interfaced with SiO_2 is close to the values known from literature [23]. E_A is significatively enhanced for the Ta interfaced sample.

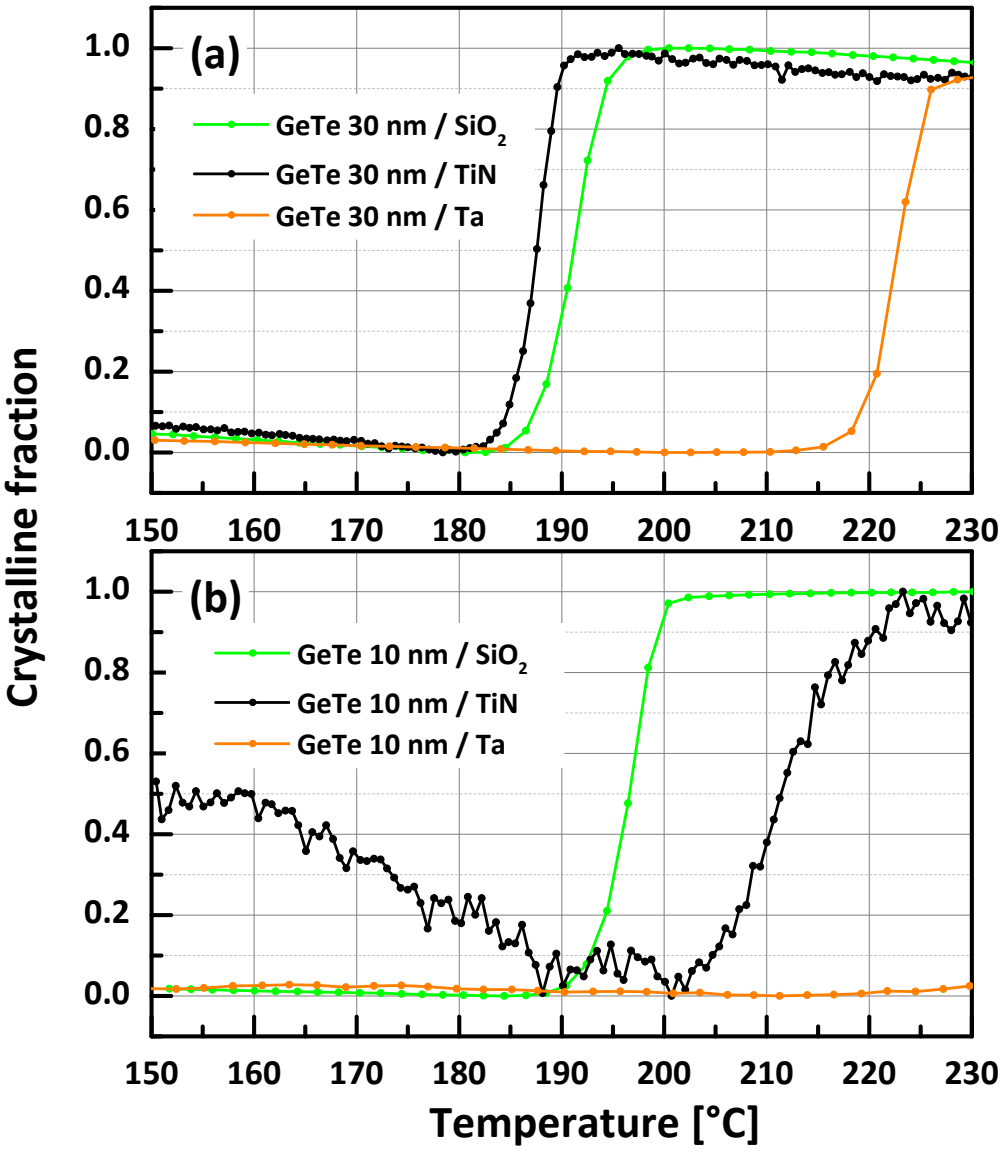

Figure 4.3: Crystalline fraction as a function of temperature from reflectivity measurements for (a) GeTe 30 nm and (b) GeTe 10 nm thin films sandwiched between TiN, Ta or SiO_2 , heated at 10°C /min. For 30 nm thick GeTe films the amorphous to crystalline phase transition occurs clearly at a higher temperature when the PC material is sandwiched between Ta. For 10 nm thick films of GeTe the measurement becomes difficult for samples interfaced with TiN and Ta, while T_x can be still easily identified for the SiO_2 interfaced sample.

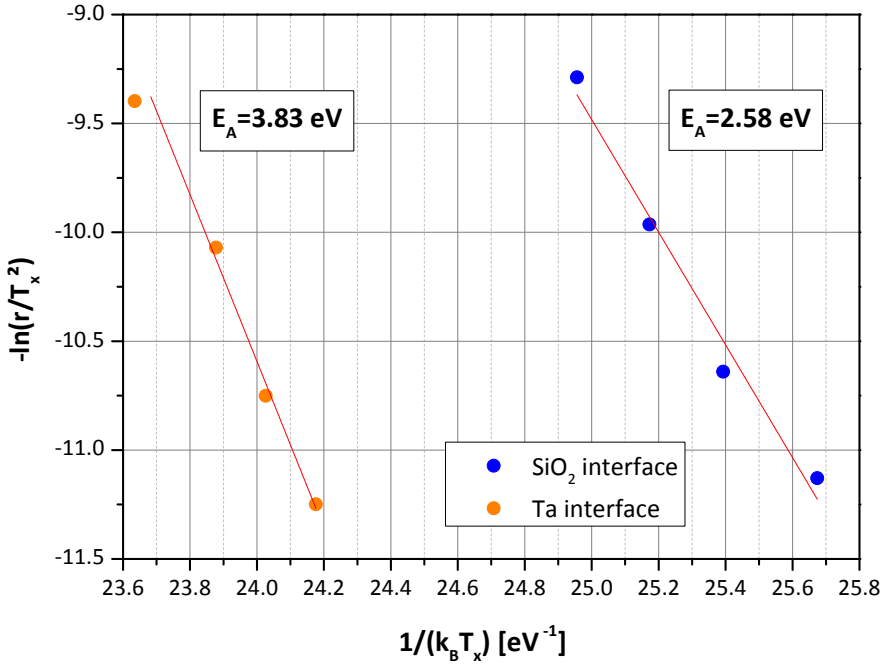

Figure 4.4: Kissinger plot for GST 100 nm thin films sandwiched between Ta or SiO_2 . The absolute value of the line slope corresponds to the activation energy E_A . The points in graph have been calculated from the T_x value obtained for four different heating rates r as reported in Table 4.3

Heating rate	T_x for SiO_2 interface [°C]	T_x for Ta interface [°C]
3 °C /min	179	207
5 °C /min	184	210
10 °C /min	188	213
20 °C /min	191	217

Table 4.3: Crystallization temperature T_x obtained from reflectivity measurements for different heating rates for GeTe 100 nm thin films sandwiched between Ta or SiO_2 .

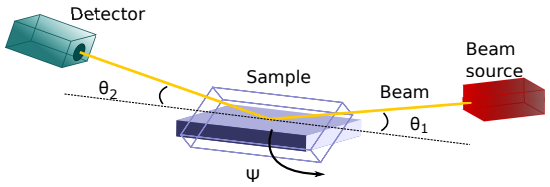

Figure 4.5: Schematic representation of the experimental geometry of the XRD experiment, where θ is the incident beam angle and Ψ is the tilting angle of the sample. A detailed description of the experimental setup is provided in appendix A.2.1

4.3 X-Ray Diffraction measurements

Three as deposited 100 nm thick films of GeTe have been characterized by in situ annealing XRD in order to investigate their crystalline structure. The samples structure is the same as the one used for the reflectivity measurements samples (shown in Fig. 4.1). The XRD experiments have been performed at $\lambda = 1.540598$Å using a PANalytical instrument equipped with a punctual pixel detector in θ-2θ configuration as described in A.2.1. The samples have been annealed under N_2 atmosphere from 100°C to 300°C by steps of 10°C . At each step the temperature was kept constant for 5 minutes before starting the measurement that lasted 1 hour and 25 minutes. Note that in the reflectivity measurement the temperature as a function of time is a ramp and the heating rate is defined as the constant slope of the temperature ramp. For the XRD experiment the temperature as a function of time is a staircase function. In order to compare the XRD results and the reflectivity measurements results, it is useful to define an equivalent heating rate approximated as equal to the step increase divided by the time step (0.11°C /min). Each measurement was performed in

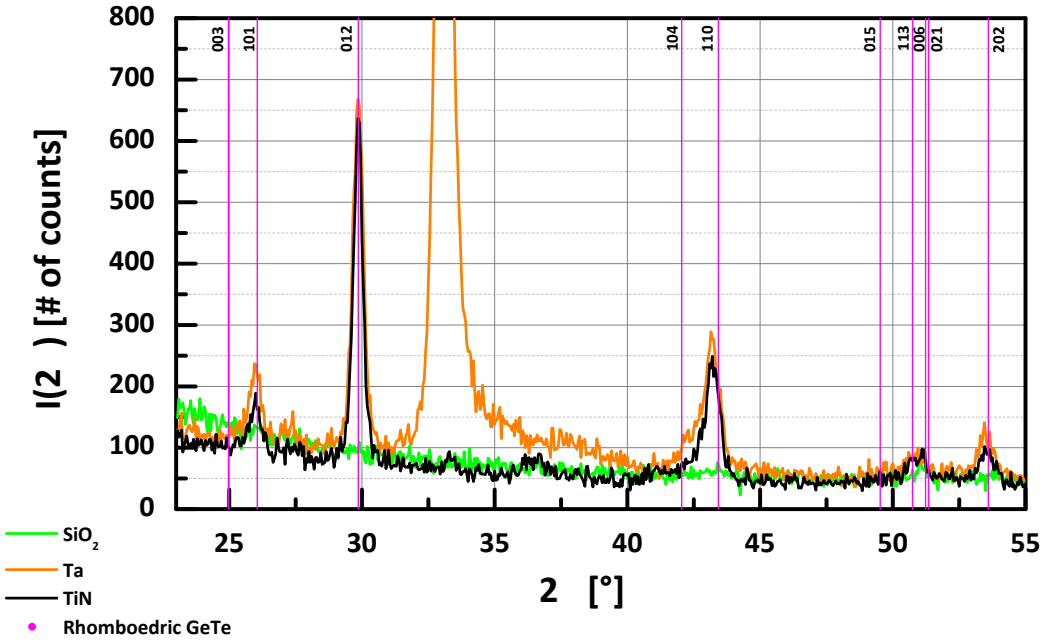

Figure 4.6: Diffracted intensity as a function of 2θ for Ψ =0°of GeTe 100 nm thin films sandwiched between TiN, Ta or SiO_2 measured at 100°C after annealing at 300°C with a heating rate of about 0.11°C /min. The vertical lines correspond to the calculated position of Bragg peaks for rhombohedral GeTe (hexagonal indexation) [25]. No difference in the diffraction spectra can be observed between the Ta and TiN interfaced samples, while no peaks are visible for the sample sandwiched in SiO_2 . The intense peak around 33° is due to Ta.

the range $23° < 2\theta < 55°$ for 4 different values of the tilting angle Ψ, shown in Fig. 4.5, corresponding to 0°, 20°, 40° and 60°. The same measurements have been done also for a descending temperature ramp after crystallization, from 300°C to 100°C , under the same conditions for temperature steps of 10°C .

The intensity as a function of 2θ for Ψ=0° for the three samples measured at 100°C after the annealing at 300°C is reported in Fig. 4.6. In the same figure the peak positions of rhombohedral GeTe at the experimental wavelength are reported, estimated by considering the lattice parameters a = 4.164 Å and c = 10.69 Å with an hexagonal indexation [25]. It is immediately evident that the SiO_2 interfaced sample shows no trace of Bragg peaks, except a weak peak around 51°. Considering that the same sample has been observed to be fully crystalline after annealing at 230°C through reflectivity measurements, the absence of Bragg peaks is probably an effect of texture, as it will be confirmed

in the next paragraph. For the Ta and TiN interfaced samples it is possible to clearly identify the 101 and 012 peaks, as well as a strongly asymmetric peak around 43°. The peak shape suggests the presence of two peaks that cannot be distinguished due to the measurement resolution and correspond to the 104 and 110 peaks of the GeTe rhombohedral phase. The intense peak around 33° in the Ta interfaced film is due to Ta.

In order to check the samples textures at complete crystallization, the 012 peaks of all the samples measured at 100°C after annealing at 300°C have been reported in Fig.4.7 for each tilting angle Ψ. It is immediately clear from the figure that the SiO_2 interfaced sample is strongly textured, since the peak intensity varies strongly with Ψ. In particular, the peak intensity is maximum for Ψ=40°, very weak for Ψ=20° and equal to zero for Ψ=0°, indicating that the angle between the preferred orientation of the diffracting planes and the sample surface is close to 40°. The Ta and TiN interfaced samples show only a weak texture. The ratio $\Delta A/A_{mean}$, where ΔA is the difference between the maximum and minimum value of the peaks area and A_{mean} is the mean area over all the values of Ψ, is around 2.62 for the SiO_2 interfaced sample, 1 for the TiN one and 0.5446 for the Ta one, confirming the difference in texture.

Considering that the most intense peaks for the SiO_2 interfaced sample are observed for Ψ=40°, the evolution of the 012 Bragg peak of GeTe as a function of temperature for each sample has been measured for Ψ = 40° and the results are reported in Fig.4.8. The Bragg peak appears at around 150°C for the sample interface with TiN, 160°C for the sample interfaced with SiO_2 and 190°C for the sample interfaced with Ta, confirming the difference of crystallization temperature observed in reflectivity measurements (section A.1). The peak area for each sample has been normalized between 0 and 1 to obtain the crystalline fraction as a function of temperature, as reported in Fig.4.9, allowing the direct comparison with the reflectivity data of Fig.4.2. The values of T_x are shown in Table 4.4.

In the case of in situ XRD experiment for all samples the crystallization takes place at lower temperatures compared to the reflectivity measurements due to the different heating rates used in the XRD and reflectivity experiments.

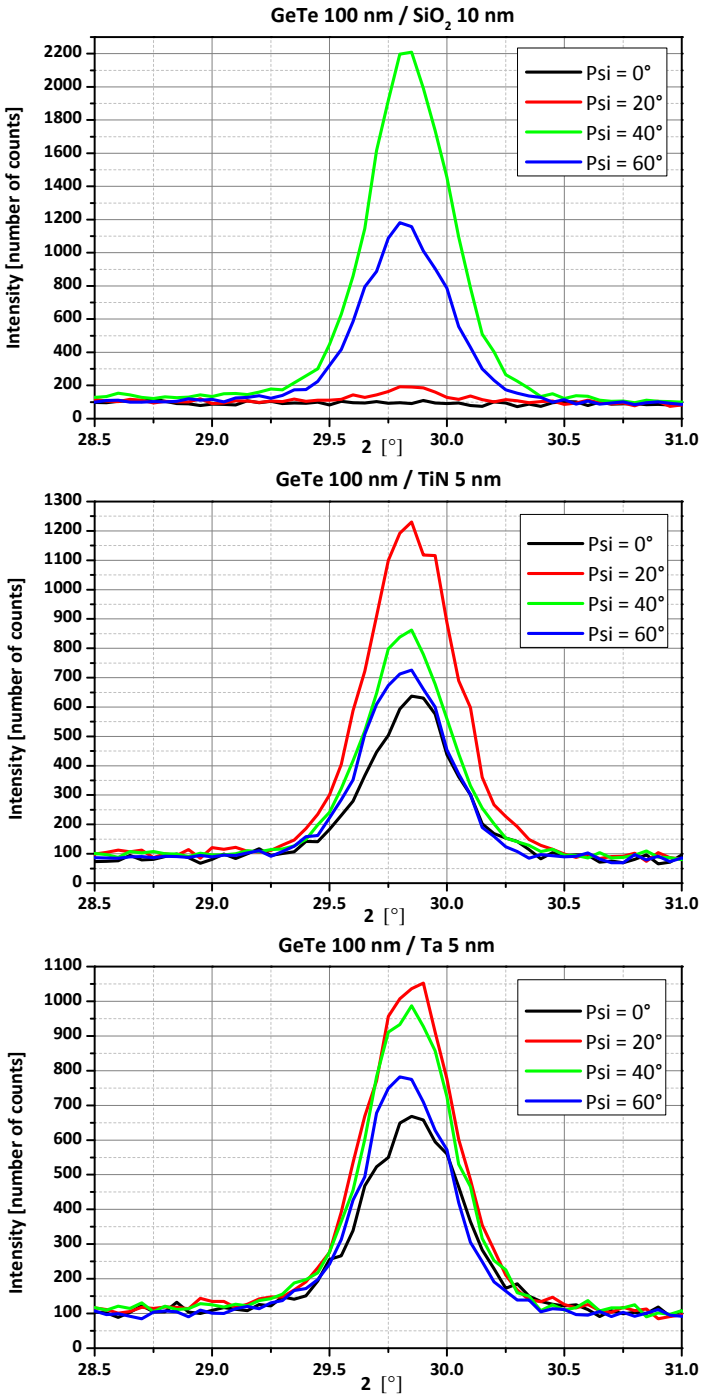

Figure 4.7: 012 Bragg peak for 100 nm thick GeTe films interfaced with SiO_2 , TiN and Ta measured at 100°C after annealing at 230°C (heating rate of about 0.11°C /min) for various tilting angles Ψ of the samples. The Ta and TiN interfaced samples show a weak texture while the sample sandwiched in SiO_2 is strongly textured, with a maximum peak intensity for Ψ=40° and no intensity for Ψ=0°.

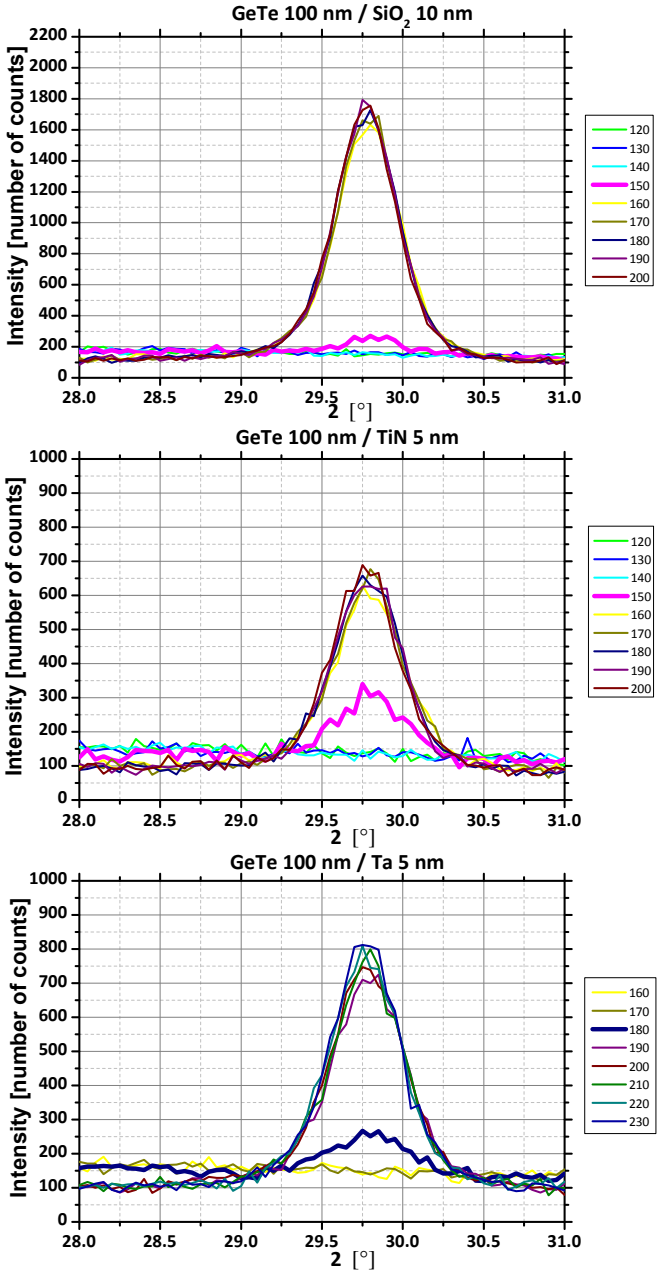

Figure 4.8: Evolution of the GeTe 012 Bragg peak as a function of temperature observed for Ψ=40° (heating rate of about 0.11°C /min) for the 100nm thick GeTe films interfaced with SiO_2 , TiN and Ta. For each sample the thickest line in the graph corresponds to the first temperature at which the Bragg peak becomes visible.

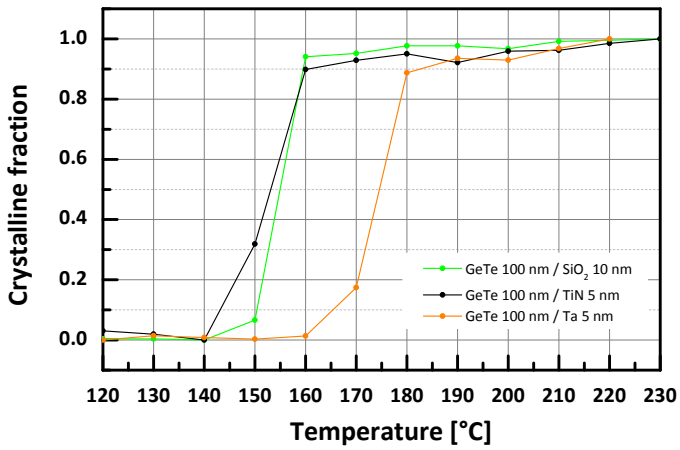

Figure 4.9: Evolution of the crystalline fraction as a function of temperature (heating rate of about 0.11°C /min) for the 100nm thick GeTe films interfaced with SiO_2 , TiN and Ta as obtained from the 012 GeTe Bragg peak area measured by XRD through in situ annealing for a tilting angle Ψ=40°.

In order to investigate a possible evolution of the samples textures with temperature the area of the 012 Bragg peak has also been calculated as a function of temperature for all the tilting angles. The results are shown in Fig. 4.10. The crystallization temperature of each sample, calculated as the temperatures corresponding to the midpoints of the rise steps of the plotted curves, remains constant for all the values of Ψ and correspond to the values already reported in Table 4.4. It can be noticed that at the beginning of crystallization the relative peak intensities for different values of Ψ are the same as at complete

	GeTe 100 nm T_x [°C]
SiO_2	154
TiN	153
Ta	175

Table 4.4: Crystallization temperatures T_x of 100 nm thick GeTe films sandwiched between TiN, Ta or SiO_2 , obtained as the temperatures corresponding to the midpoints of the rise steps of the Bragg peaks areas as a function of temperature reported in Fig. 4.9 (heating rate of 0.11°C /min).

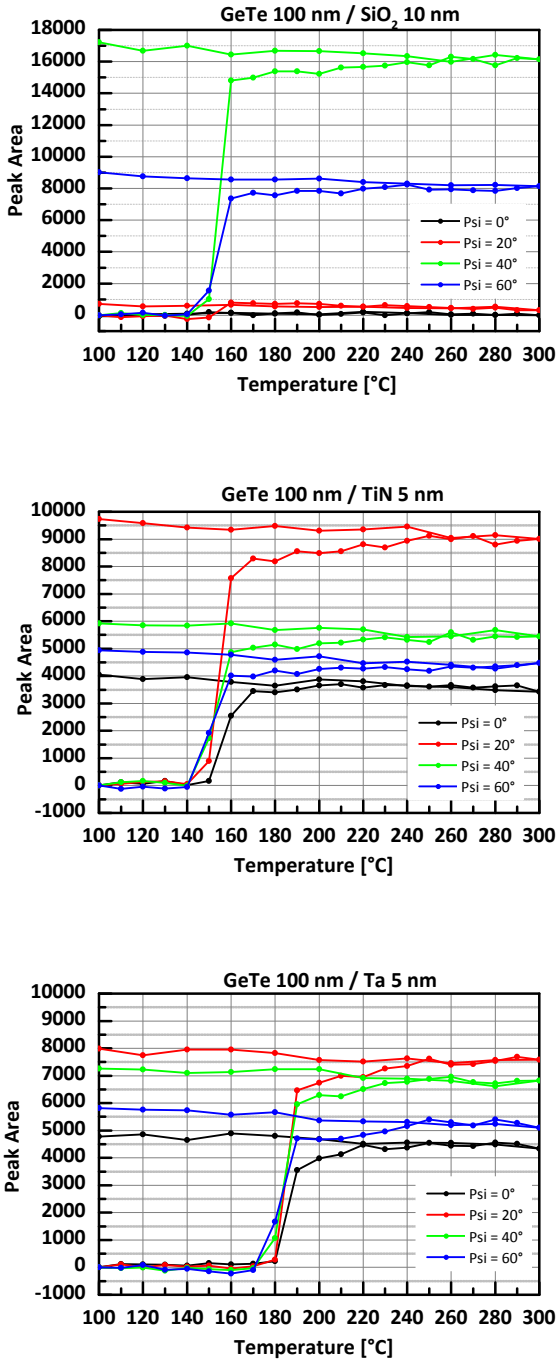

Figure 4.10: 012 Bragg peak area as a function of temperature (heating rate of 0.11°C /min) and of the sample tilting angle Ψ for 100 nm GeTe films sandwiched between TiN, Ta or SiO_2 . The points on the descending temperature ramp are also shown, and no evolution occurs during the cooling down process.

	Ψ=0° [nm]	Ψ=20° [nm]	Ψ=40° [nm]	Ψ=60° [nm]
SiO_2			77	68
TiN	63	67	67	65
Ta	56	60	62	58

Table 4.5: Final mean grain sizes measured at 100°C after annealing for different values of the tilting angle Ψ for 100nm thick GeTe films.

crystallization only for the SiO_2 interfaced sample. For both the TiN and Ta interfaced samples, the most intense peaks at the beginning of crystallization correspond to Ψ=40° and Ψ=60°, while the most intense peak is found for Ψ=20° at complete crystallization. This suggests an evolution of texture with temperature.

The evolution of the grain sizes as a function of temperature, calculated using Sherrer analysis on the 012 Bragg peaks of all the samples and neglecting any inhomogeneous strain (see appendix A.2.1), is shown in Fig.4.11. The instrumental resolution is $FWHM_{instr}$=0.295°and the error bar for the grain size is about ± 5 nm. The grain size has been calculated for each point of the increasing temperature ramp and at 100°C after annealing. For Ψ=0° no peaks are detectable for the SiO_2 interfaced samples and for Ψ=20° the signal is so weak that no reliable results can be obtained, thus for Ψ=0° and Ψ=20° the grain size has been calculated only for the TiN an Ta interfaced samples. When possible, the grain size after in situ annealing has been calculated and is reported in Table 4.5. For both Ψ=40° and 60°, the sample interfaced with SiO_2 has the highest grain size, while the Ta interfaced sample has the smallest grain size and intermediate values are found for the TiN interfaced sample. In particular, the effect is more marled for Ψ=40°. For both Ψ=0° and Ψ=20° the grain size is slightly larger for the TiN interfaced sample than for the Ta interfaced one.

4.4 Synchrotron X-Ray Diffraction

A set of samples of 100 nm thick GeTe films interfaced with Ta, TiN or SiO_2 has been annealed at 400°C for 15 minutes (equivalent heating rate around 26.7°C /min)

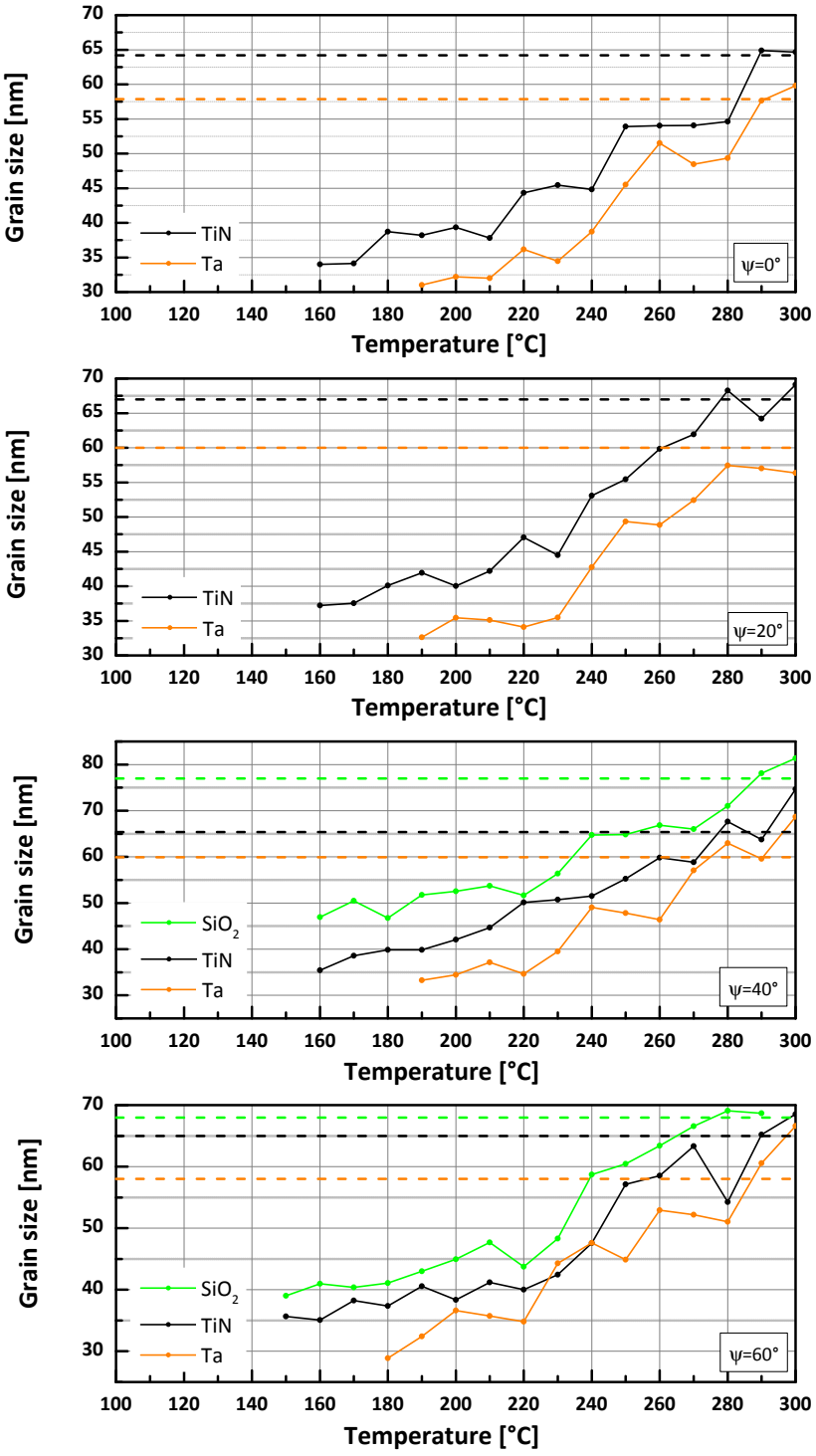

Figure 4.11: Grain size calculated by Sherrer analysis on the 012 Bragg peak of GeTe 100 nm thin films interfaced with SiO_2 , TiN or Ta. The error bar is about ± 5 nm. The dashed lines indicate the final dimensions of grains, measured at 100°C after annealing, and are reported in Table 4.5.

and has been characterized by X-ray Diffraction on the BM02 CRG-D2AM beamline (ESRF Grenoble, France) with an incident photon energy of 17.5 keV photon (λ =0.707 $\mathring{A}$) and using a 2D CCD camera detector. A detailed description of the experimental setup, which is similar to the one used in Chapter 3, can be found in appendix A.2.2. The 3D image of the SiO_2 interfaced sample shown in Fig. 4.12(a) clearly shows that the intensity of the partial diffracted rings corresponding to GeTe 101, 012, 104 and 110 Bragg peaks is zero around the center of the image and very high at the image borders, indicating a strong texture. In Fig.4.12(b) the TiN interfaced sample is characterized by a light texture while the Ta interfaced sample in Fig.4.12(c) exhibit completely isotropic rings. This result is in agreement with those obtained from the in situ XRD experiments described in section 4.3 for the SiO_2 interfaced sample. In particular, the absence of signal measured at Ψ=0° agrees very well with what can be seen in Fig. 4.12(a). However, the weak texture observed in section 4.3 for the Ta sample is absent, while the texture of the TiN interfaced sample is stronger in Fig.4.12(b) compared to what observed in section 4.3. This observation suggests that the final texture is influenced by the anneling conditions. The samples were identical in both experiments but at the synchrotron they have been annealed at 400°C for 15 minutes, while the samples of section 4.3 have been heated up to 300°C at a heating rate of 0.11°C /min, staying at high temperature for a long acquisition time.

4.5 Discussion and conclusions

An effect on the crystallization temperature of interfacing GeTe and GST films with a Ta capping layer has been observed and confirmed both through XRD and reflectivity measurements. First, the increment of T_x for a sample interfaced with Ta compared to SiO_2 or TiN interfaced ones exists even for films 100 nm thick, indicating that it is not correlated to a size effect. Moreover, the activation energy E_A is higher for Ta interfaced samples than for the SiO_2 interfaced ones. The grain size measured for Ψ=40° is higher for the SiO_2 interfaced sample than for the TiN and Ta interfaced samples, and the SiO_2 interfaced sample

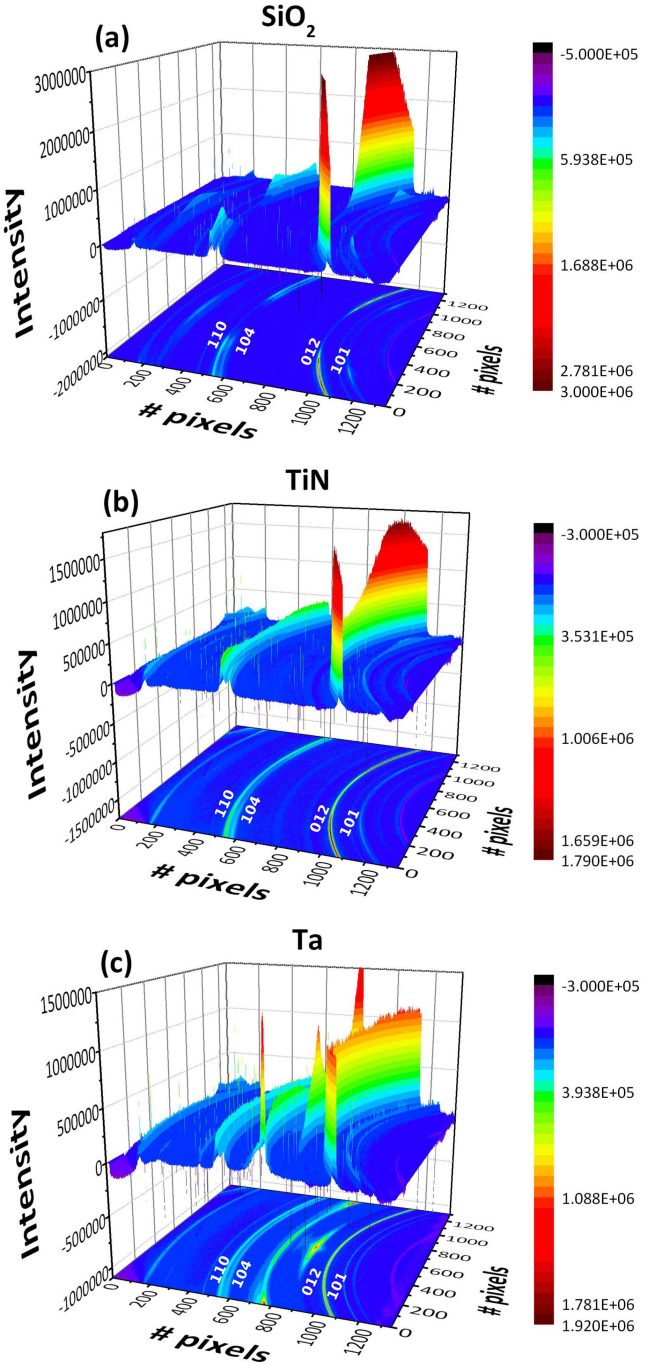

Figure 4.12: 3D images of the diffracted rings obtained for GeTe 100 nm thin films annealed at 400°C for 15 minutes and interfaced with (a) SiO_2 (b) TiN (c) Ta. The SiO_2 interfaced film is strongly textured while only a faint texture is visible for the TiN interfaced film and the GeTe rings are isotropic for the Ta interfaced film. The strongly textured rings that can be seen in (c) correspond to Ta.

	SiO_2	TiN	Ta
GeTe 100 nm T_x [°C]	188	193	213
E_A [eV]	2.58	not measured	3.83
Thickness dependence of T_x	weak	weak	strong
Texture	strong	weak	weak
Grain size for Ψ=40° [nm]	77	67	62

Table 4.6: Summary of the different characteristics observed for GeTe thin films encapsulated in SiO_2 , TiN or Ta. The SiO_2 and Ta interfaced samples present the most relevant differences in their properties, while the TiN interfaced sample can be considered as an intermediate situation.

is strongly textured while it is not the case for the other samples. Finally, the crystallization temperature remains almost constant for the SiO_2 interface as the PC films thickness is reduced from 100 nm to 10 nm, while it increases for the the other samples, the effect being more marked on the Ta interfaced sample. All these different characteristics are summarized in Table 4.6, where it is evident that the samples interfaced with SiO_2 and Ta exhibit relevant differences in their properties while the TiN interfaced sample can be considered as an intermediate situation. For this reason, the discussion will be focused mostly on the differences between SiO_2 and Ta samples.

In order to identify the preferred orientation in the SiO_2 interfaced sample, the diffracted intensity as a function of 2θ (already reported in Fig.4.6 for Ψ=0°) is shown in Fig.4.13 for each value of Ψ. The curves are vertically shifted for clarity. It can be immediately noticed that while the 012 Bragg peak reaches its maximum intensity for Ψ of about 40°(see Fig.4.7), the 101, 202, 104 and 110 peaks exhibit the highest intensity for Ψ=20°. It can be observed that the angle between the (012) plane and the (010) plane is around 38°, while the angle between the (101) and (100) planes is around 21°. This suggest that the grains grow with a preferred orientation with the (100) or (010) plane parallel to the sample surface.

It is worth noting that different values of E_A and T_x could be explained by an effect of doping due to the diffusion of the encapsulating material into the PC

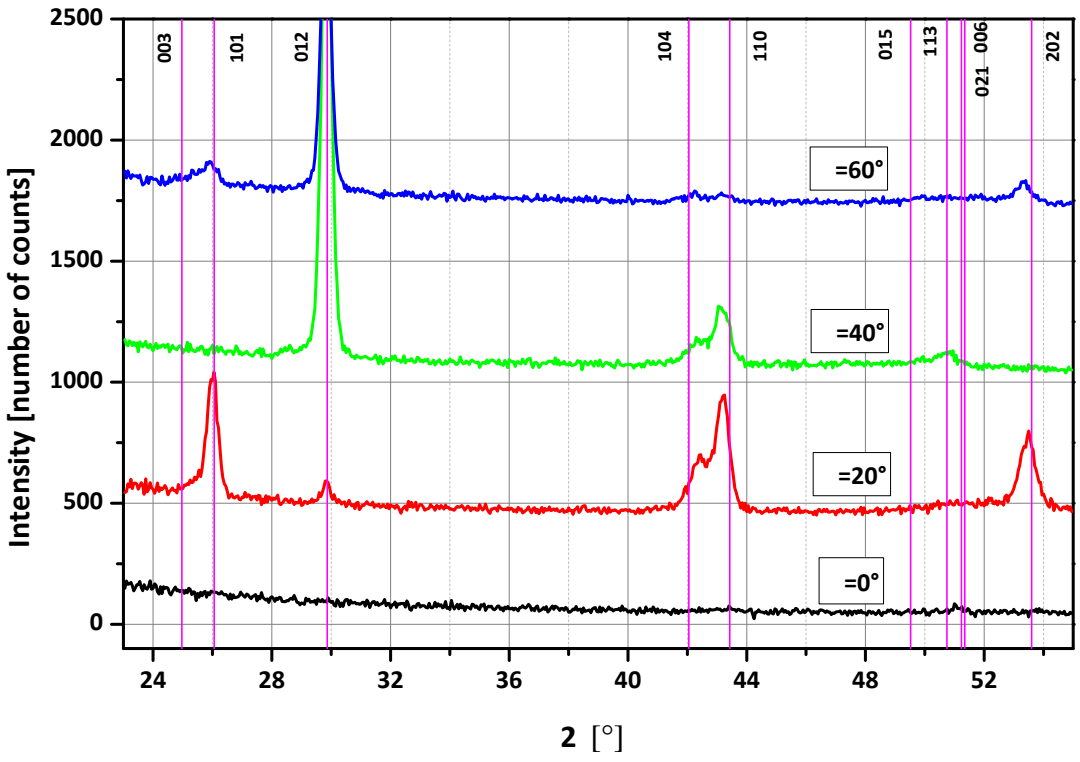

Figure 4.13: Diffracted intensity as a function of 2θ for the GeTe 100 nm thin film interfaced with SiO_2 , measured at 100°C after annealing at 300°C (heating rate around 0.11°C /min) for various tilting angles Ψ. The intensity of the 012 Bragg peak is maximum at around Ψ=40°, as already reported in Fig.4.7, while the 101, 202, 104 and 110 peaks exhibit the highest intensity for Ψ=20°.

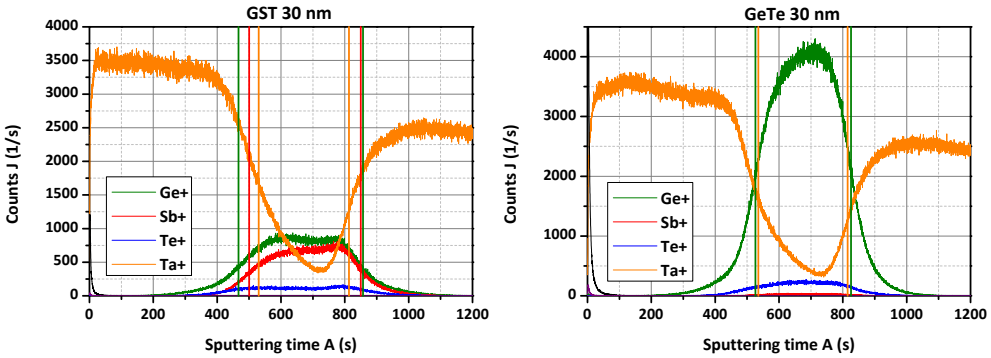

Figure 4.14: Secondary Ion Mass Spectrometry (SIMS) measurements performed on GeTe and GST 30 nm thin films sandwiched with Ta. By definition, the interface for each element can be placed in the point at which half of the signal intensity is lost, corresponding to the vertical lines in the figure. From those measurements the diffusion of Ta inside the GeTe and GST layers is extremely low.

layer, as described in Chapter 2 in the case of N and C doping elements. In order to exclude this effect, Secondary Ion Mass Spectrometry (SIMS) measurements have been performed on GeTe and GST 30 nm thick films sandwiched in Ta. The results, reported in Fig. 4.14, show a very weak diffusion of Ta inside GeTe or GST films, thus establishing that the samples are not Ta-doped.

It is possible to find an explanation for the observed phenomena by making the hypothesis that the SiO_2 /GeTe interface is energetically more favorable for a particular orientation than the Ta/GeTe interface. If this hypotesis is true, it leads to some consequences that will be analyzed in the following. First, the different grain dimensions obtained at Ψ=40°for SiO_2 and Ta interfaced samples can be explained as a result of an abnormal grain growth along a preferred direction [105]. If the interfacial energy between GeTe and SiO_2 is minimized for grain textured with the (012) plane tilted by around 40°with respect to the sample surface, then the the growth of grains with this orientation is preferred. As a result, the grain sizes are larger for those grains and the sample is textured, corresponding to what observed experimentally.

A second consequence of the hypothesis of an energetically favorable SiO_2 interface can be a different crystallization mechanism for the two samples. The crystallization can begin as heterogeneous nucleation at the interfaces for the sample

sandwiched in SiO_2 and then the growth of those nuclei is dominant in the crystallization process, being more rapid than the homogeneous nucleation that takes place in the bulk of the PC material. This situation in illustrated in Fig. 4.15 a. On the other hand, as represented in Fig. 4.15 b, for the sample interfaced with Ta the heterogeneous nucleation at the interfaces could be somehow suppressed or slowed down, so that the crystallization process is now dominated by the homogeneous nucleation which is known to be normally slower than the heterogeneous nucleation (see section 1.3.3).

The difference in the crystallization mechanism between samples interfaced with Ta and SiO_2 is supported by the evolution of the crystallization temperature T_x with thickness. Considering the model of Zacharias reported in section 3.1.1, homogeneous nucleation can induce large variation of T_x with shrinking thickness while it is not necessarily the case for heterogeneous nucleation. This is coherent with what observed for Ta and SiO_2 interfaced samples, as reported in Table 4.6.

The situation of the sample interfaced with TiN is somehow in the middle between the Ta and SiO_2 interface cases. The value of T_x corresponds to the one measured for the SiO_2 interfaced sample, while the weak texture and the grain size indicate no preferred orientation for grains growth. This suggests that the crystallization begins with heterogeneous nucleation as in the SiO_2 interfaced sample case, but with no preferred grain orientation and no consequent abnormal growth, leading to a weak texture of GeTe and a grain size comparable to the one measured for the Ta interfaced sample.

Even if the assumption of an energetically favorable interface for SiO_2 can well explain the obtained results, some questions are still open. If the situation depicted in Fig.4.15 is true, the SiO_2 interface should promote heterogeneous nucleation more than the Ta interface, which should inhibit the formation of nuclei instead. This is unexpected because it looks unlikely that an amorphous could trigger nucleation more easily than a metal. Indeed, in Ref.[12] the nucleation of various Ge-Sb-Te compounds have been studied and no heterogeneous nucleation at the PC material/substrate interface was observed, even for a SiO_2 interface, and the only nucleation observed is the one at the interface with the native oxide

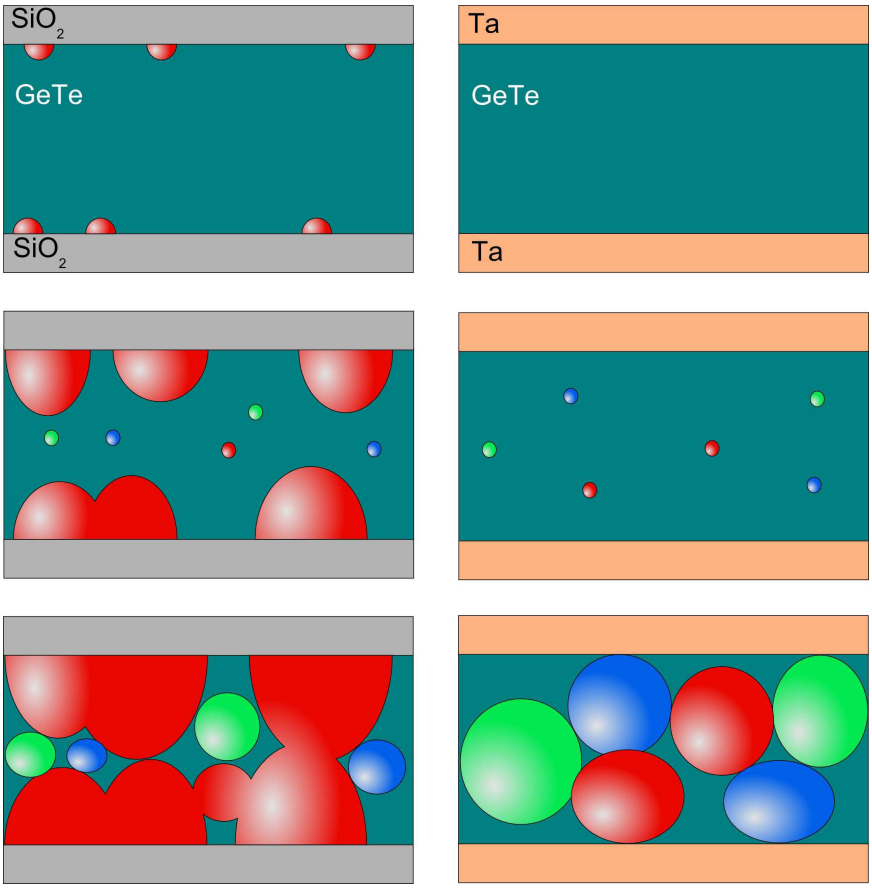

Figure 4.15: Possible models of crystallization for (a) SiO_2 and (b) Ta interfaced GeTe thin films. Different colors correspond to different orientation of the grains. In the case of SiO_2 interface the crystallization begins with heterogeneous nucleation at the energetically favorable interface and the nuclei grow with a preferred orientation before the homogeneous nucleation starts. The final result are bigger grains with a preferred orientation. In the case of Ta interfaced PC thin film, the heterogeneous nucleation at the interfaces is somehow suppressed, thus the crystallization is driven by the homogeneous nucleation that starts later respect the heterogeneous one, leading to a weak texture.

of the PC material. The homogeneous nucleation was not observed either. This can be explained by considering that the native oxide for a Ge-Sb-Te material is usually GeO or GeO_2 so that the Ge-Sb-Te material is Ge-depleted at that interface and this lowers T_x [6]. In the case of samples interfaced with a capping material on both sides, as the films studied here, no native oxide should exist at the interfaces so this preferential nucleation site is absent. However, considering that the film of SiO_2 is deposited by PVD, it can present an excess of Si or O. In case of an O-rich SiO_2 an oxidation at the GeTe/SiO_2 interface cannot be excluded, while in the case of a Si-rich SiO_2 some nanocrystals of Si can possibly form inside the oxide and act as nucleation sites [106].

Even if the effect of different interfaces on the T_x of a PC material is evident, the reasons behind this phenomena are still unclear. Further studies are required, focused on confirming the hypothesis of an energetically favorable grains orientation at the GeTe/SiO_2 interface and the following consequences on the nucleation and growth.Besides, studies by XPS experiments on the local structure at the interfaces are required. TEM measurements could be useful in order to investigate nucleation mechanism for different interfaces.

Conclusion

The present work gives a contribution to understand the properties of some PC materials used in PCM devices and the effects of scaling and interface on the amorphous to crystalline phase transformation.

The first part of the thesis has been dedicated to investigate the local structure of C and N doped amorphous GeTe. The aim was to understand the local origin of better electrical properties of doped GeTe devices compared to undoped GeTe ones. The impact of doping was observed experimentally through the appearance of a new peak in the pair distribution function of doped GeTe, indicating the formation of a bond at a new distance that is absent in the undoped amorphous material. The formation of new environments involving carbon and nitrogen has been confirmed through ab-initio simulations. In the case of carbon doping, strong changes are induced at the second neighbor level through tetrahedral and triangular units centered on carbon. The new peak observed experimentally corresponds to new Ge-Ge distances in these units, while for N-doping it correspond to the new Ge-Ge distance in tethahedral and pyramidal units centered on nitrogen. It should be remarked that for C doped GeTe measured and calculated pair distribution functions are in good agreements, whereas the agreement is not as good for N doped GeTe. One possible explanation, to be confirmed, is that an important proportion of nitrogen form N_2 molecules in the film. Further steps require the study of the crystalline phase of doped materials, in order to understand the role played by doping elements during

and after crystallization. This is extremely important from the point of view of optimizing materials for a device.

The subject of the second part of this work has been the impact of confinement on GST crystallization. A fundamental requirement for further development of PCM is their ability to be scaled without deterioration of their properties. The results known from literature for thin films, reported in Chapter 3, were not encouraging. In this thesis, nano-sized clusters of GST embedded in Al_2O_3 have been made using a sputtering gas phase condensation source and their crystallization has been studied through X-ray diffraction. The amorphous to cubic crystalline phase transition has been unambiguously observed for clusters. The crystalline clusters experience a tensile strain that can be ascribed to the effect of the surrounding rigid Al_2O_3 matrix. The crystallization temperature of clusters is only slightly higher than that of a 10 nm thin film of GST deposited under the same conditions. It is worth underlining that this result is positive for PCM because it shows that the scaling effect on the crystallization temperature in a phase change material can be small. Further studies are required in order to clarify the origin of this difference in crystallization temperature, since many different effects can be involved. A composition effect (rising from the fact that clusters are slightly Te-depleted compared to the thin film), different surface to volume ratio, matrix influence, stress effects or an intrinsic size effect could all play a role. The obtained results open new possibilities for the study of nano-sized clusters of phase change materials. These particles have been deposited by a method which is close to the one used for PCM thin films deposition, thus giving information that can be easily exported to device fabrication. It would be interesting to deposit smaller GST clusters, but with this method their size distribution will be larger. Furthermore, it would be useful to study if nanoclusters of other PC material, such as GeTe, show the same evolution of T_x with scaling. Finally, a study of the variability of phase change properties with size, i.e. identification of intrinsic vs extrinsic effects, should be done. In addition, the electrical properties of clusters can be measured.

The third and last part of the thesis has been dedicated to the investigation of the interface material effect on the crystallization temperature of GeTe

and GST. It has been observed through reflectivity measurements that both GeTe and GST interfaced with Ta show a crystallization temperature around 20°C higher than the one of GeTe and GST interfaced with TiN or SiO_2 . Even if some studies in literature had evidenced the influence of interfaces over the crystallization temperature of Ge-Sb-Te materials, such a remarkable difference in T_x , due only to an interface effect, was never reported before. X-Ray diffraction results on GeTe showed that the SiO_2 interfaced samples are characterized by a strong texture while a weak texture is observed for Ta and TiN interfaced samples. The results obtained for T_x and the samples texture can be explained by supposing different nucleation and growth mechanisms for the different samples. Nucleation would begin at the SiO_2 /GeTe interface and grains grow along a preferred direction through the film thickness, originating a textured crystalline film. For Ta interfaced samples the nucleation at the Ta/GeTe interface would be somehow suppressed and the nucleation would be only homogeneous with no preferred orientation and no texture. The case of the TiN interface is somehow intermediate. However, it is unclear how an amorphous interface can promote nucleation of crystal phase more easily than a metallic interface. Actually, a simulation in COMSOL Multiphysics is already in progress in order to quantify the crystallization parameters that are influenced by different interface materials.

From a more general point of view, studies should move from a global to a local approach. It will be interesting to check the nucleation mechanism for different interfaces not only through simulation, but also through transmission electron microscopy measurements. This technique will be useful to observe the phase change in nanoclusters of Chapter 3. Similarly, X-ray photoelectron spectroscopy can be used to study the chemical bonding near the interfaces and to investigate the chemical bonding of C and N doped GST and GeTe samples, both in the amorphous and crystalline phase.

Finally, let us recall that the goal of these studies is the understanding of scaling and confining effect on advanced phase change materials used in PCM. In this thesis, the effects of doping, scaling and interfaces have been addressed separately. The obtained results and the success of the cluster deposition method

open new perspectives. For instance, considering the remarkable interface effect evidenced in thin films, it would be interesting to deposit and characterize different PC materials clusters embedded in different matrices as Ta, TiN, W or SiO_2 . Indeed, such nanoparticles offer a high surface to volume ratio that can enhance the interface effect. Another perspective is to deposit N or C doped clusters. This could allow to study the impact of doping on such small systems, as well as the effect of doping concentration variability.

Appendix A

Experimental Techniques

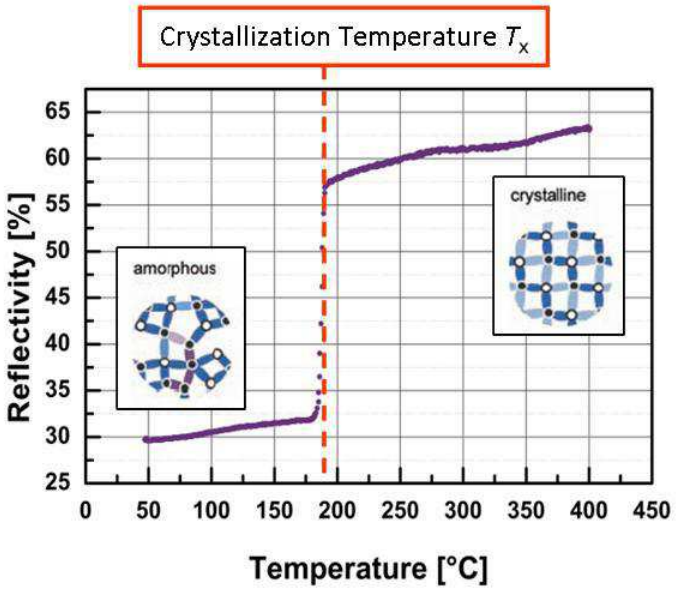

Figure A.1: Evidence of the different optical properties of the PC material $Ge_2Sb_2Te_5$ in the amorphous and crystalline phases. The reflectivity of GST is reported as a function of temperature starting from an initially amorphous sample. The amorphous phase is characterized by a low reflectivity value compared to the one of the crystalline phase. On the graph it is easy to identify the crystallization temperature at which the phase transformation occurs.

A.1 Reflectivity measurements

Reflectivity measurements consist in monitoring the reflectivity value of a PCM sample as a function of temperature. The amorphous phase is characterized by a lower reflectivity than the crystalline phase, so when the phase transformation occurs the measured reflectivity value increases. An example of a measured curve has been shown in the Introduction of Chapter 1 (Figure 1.2). The crystallization temperature can be defined as the point of maximum derivative of the measured reflectivity curve (other definitions of T_x can be considered, as discussed in section 3.1.1). The measured reflectivity can be normalized in order to obtain the crystalline fraction.

A schematic description of the reflectometer used for the experiments performed in this thesis is reported in Figure A.2. An amorphous sample is placed in a vacuum chamber on a heating plate and the sample reflectivity is measured through a red laser beam (λ=670 nm). The plate temperature can reach

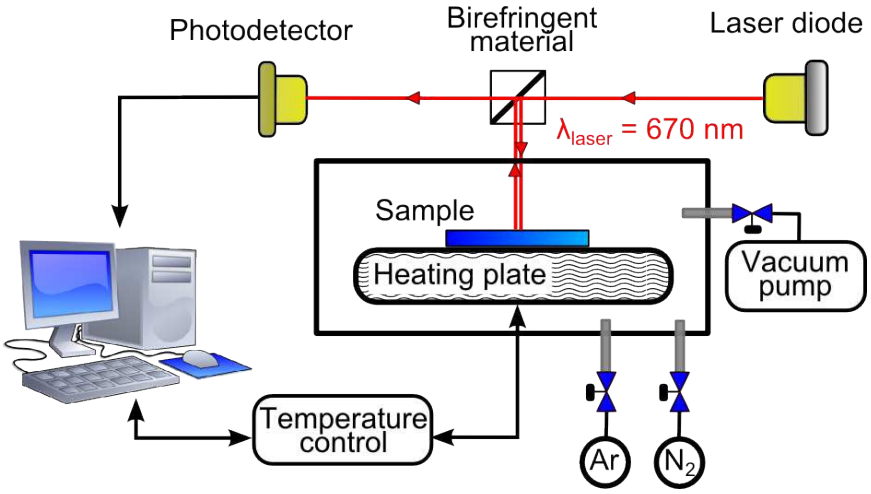

Figure A.2: Schematic representation of the reflectometer used for reflectivity measurements. The laser beam is directed onto a birefringent filter and divided in two beams, and one of them is directed to the sample. The direct and reflected beams are collected by a photodetector and processed to obtain the measured signal.

a maximum value of 400°C with a heating rate that can vary between 2°C /min and 20°C /min. The temperature is continuously measured by a thermocouple and controlled by a temperature feedback. The samples can be measured under vacuum or in an argon atmosphere, in order to limit the oxidation at high temperatures. It is important to remark that the crystallization can be observed only for the part of sample in which the laser beam penetrates (around 30 nm). The capping layer that is deposited over the phase change material should then be sufficiently thin to let the beam reach the underlying layer. Moreover, the effect of beam reflection by the capping layer can affect the measured reflectivity and can even hide the PCM signal if the capping material is not transparent enough to the laser beam.

A.2 X-Ray Diffraction

From the analysis of X-ray diffraction it is possible to deduce information on the sample structure and microstructure.

When an incident wave interacts with the electrons of an atom, if no energy loss occurs, the result is a new spherical wave with the same energy of the incident

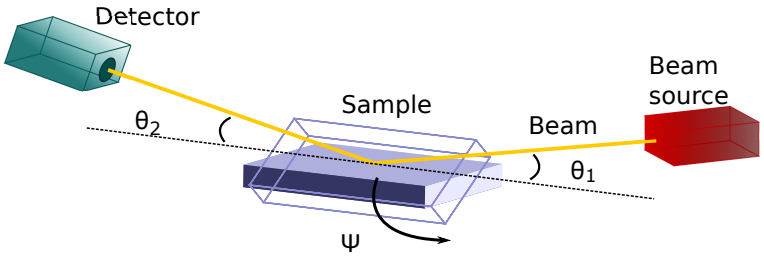

Figure A.3: Schematic representation of the geometry used for XRD analysis in laboratory. The experiment is performed in a θ-2θ configuration ($\theta_1 = \theta_2$) and the tilting angle Ψ allows to measure the sample texture.

wave (elastic scattering). When two or more atoms are involved, the resulting spherical scattered waves interact by constructive or destructive interference depending on their phases.

In this thesis, the XRD experiments have been performed by means of two different X-Ray sources. The first one is a conventional source, an X-Ray tube used in laboratory measurements. The second one is the synchrotron radiation that is required for measuring very small systems (as the nanoclusters described in Chapter 3) due to its high brilliance.

A.2.1 Conventional X-Ray Diffraction laboratory experiment

In laboratory, the XRD experiments were performed in the θ-2θ configuration with the geometry schematically reported in Fig.A.3. The variation of the tilting angle Ψ allows to measure the sample texture. The instrument consists in a XPERT PRO MRD diffractometer equipped with a Cu anode (λ=1.5406$\AA$) and a PANalytical pixel point detector. A furnace (Anton Paar) is used for XRD with in-situ annealing in the temperature range 100$-$300°C . In order to get the peak width and position the diffracted peaks are fitted by a Pseudo-Voigt function. Supposing that there is no inhomogeneous strain effect, the grain size can be calculated from the peak width by using the Scherrer's formula

$$D_{hkl} = \frac{0.9 \cdot \lambda}{(\Gamma_{\text{meas}} - \Gamma_{\text{instr}})\, cos\theta} \tag{A.1}$$

where D_{hkl} is the grain size calculated for the direction perpendicular to the ⟨hkl⟩ plane, λ is the experimental wavelength, Γ_{meas} is the measured Full Width Half Maximum, Γ_{instr} is the instrumental Full Width Half Maximum and 2θ is the peak position. For the instrument used $\Gamma_{\text{instr}} = 0.295°$.

A.2.2 Large-scale facilities experiments

In this thesis, experiments have been performed at two different Synchrotron beamlines, the CRISTAL beamline (SOLEIL, Saclay) for the experiments described in Chapter 2 and the BM02 CRG-D2AM beamline (ESRF, Grenoble) for the experiments reported in Chapters 3 and 4 respectively. In both cases the intensity as a function of 2θ is obtained by integration over a bidimensional image but the experimental methods differ. On beamline CRISTAL X-ray scattering has been measured up to large scattering angles in order to determine the pair distribution function, while at ESRF selected Bragg peaks have been studied.

SOLEIL data analysis

The experiment at the synchrotron SOLEIL have been performed in transmission geometry over the powder samples described in Chapter 2. The experimental setup is shown in Fig.A.4. The incident beam has an energy of of E=45.4793 keV ($\lambda = 0.4441$Å) and the transmitted scattered beam is collected by an image plate detector MAR350 (3450x3450 100μm pixels). An example of image is reported in Fig.A.5 for an amorphous GeTe sample. The distance D between the sample and the image plate was equal to $\approx$ 21cm and could not be reduced (see Fig.A.4). Considering that obtaining a good quality structure requires measurements in a large range of Q, and considering that the distance D could not be reduced further, one chose a configuration where the center of the image plate does not coincide with the incident beam as can be seen in Fig.A.5. This allows to obtain a wider range of Q (up to 20.1 Å^{-1}) by integrating over a vertical sector. One drawback of this set-up is a loss of intensity since only a fraction of the diffraction ring is selected for integration.

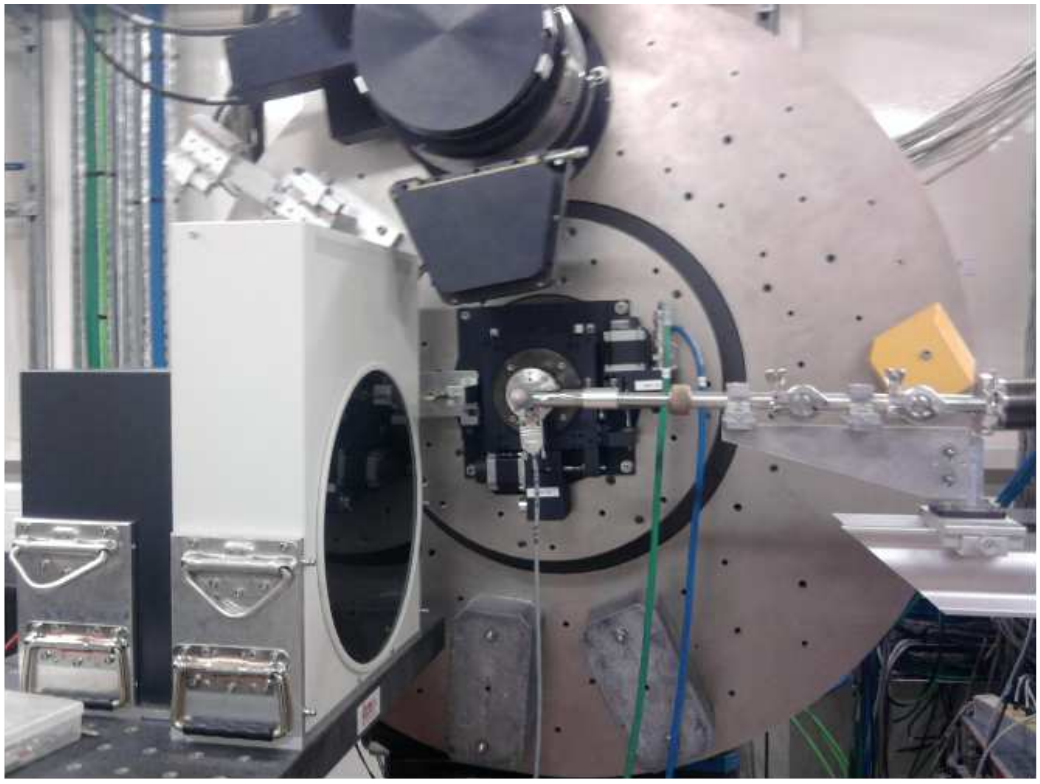

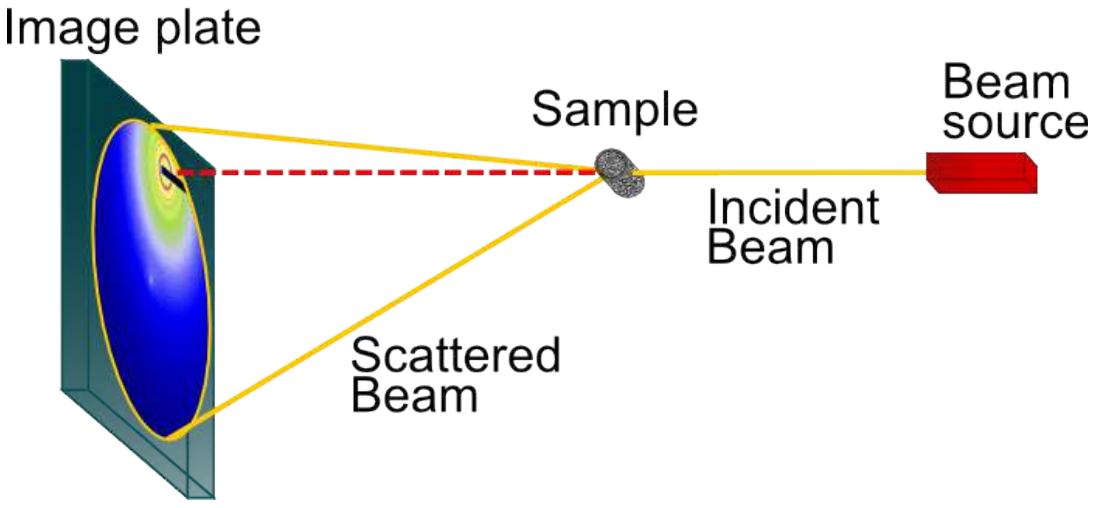

Figure A.4: Picture and schematic representation of the experimental setup used at the synchrotron SOLEIL. The scattered transmitted beam is collected by an image plate detector placed at a distance D≈ 21cm from the sample, which is the minimum allowed distance in this configuration. Thus, in order to obtain a high value of Q, the center of the image does not correspond to the center of the detector.

The counting time for one image was 300 s. Each image has been corrected by subtracting the dark image acquired without beam in the same conditions. All the images have been treated by using the freeware software Fit2D [107]. It is necessary to first correct the image for the geometrical errors due to the tilting of the image plate with respect to the plane perpendicular to the incident beam. The tilt parameters as well the distance between the sample and the detector can be obtained by analysing the image of a LaB_6 powder sample measured in the same conditions. Each image can then be integrated. The integration sector is shown in Fig.A.5. The integration process takes into account polarization corrections. The value of polarization was 0.96.
The resulting intensity as a function of 2θ must finally be multiplied by $\frac{1-e^{\left(-\frac{d\mu_{IP}}{cos2\theta}\right)}}{1-e^{-d\mu_{IP}}}$ in order to take into account the incomplete absorption of photons in the active layer of the image plate of thickness d and absorption coefficient μ_{IP}.
In order to extract the scattering from the sample from the intensity measured on the filled capillary, it is necessary to substract the scattering by the empty capillary, taking into account the sample transmission, and to remove the scattering by air. For each case (filled capillary, empty capillary or air) 4 images have been acquired for 300 s and the obtained integrated intensities summed up. The integrated intensity scattered by the sample I(2θ) is obtained by using the following relation

$$I(2\theta) = [(I_{raw} - I_{air}) - t \cdot (I_{emptycap} - I_{air})] \cdot \frac{1 - e^{\left(-\frac{\mu_{IP}}{cos2\theta}\right)}}{1 - e^{-\mu_{IP}}} \qquad \text{(A.2)}$$

where I_{raw} is the raw intensity measured on the filled capillary , I_{air} is the air signal, $I_{emptycap}$ is the intensity of the empty capillary and t is the measured transmission coefficient. The obtained quantity has then been processed by using the PDFgetX2 software [108] which removes the Compton and fluorescence signals, converts 2θ in Q and by adequate normalization gives the structure factor S(Q). It should be emphasized that all the data corrections and normalization must be performed carefully since any inadequacy directly affects the asymptotic behaviour of S(Q). If S(Q) is not tending to 1 at large Q the pair distribution function obtained by Fourier transform of Q(S(Q)-1) (see Eq. 2.18 in Chapter 2) is dramatically affected.

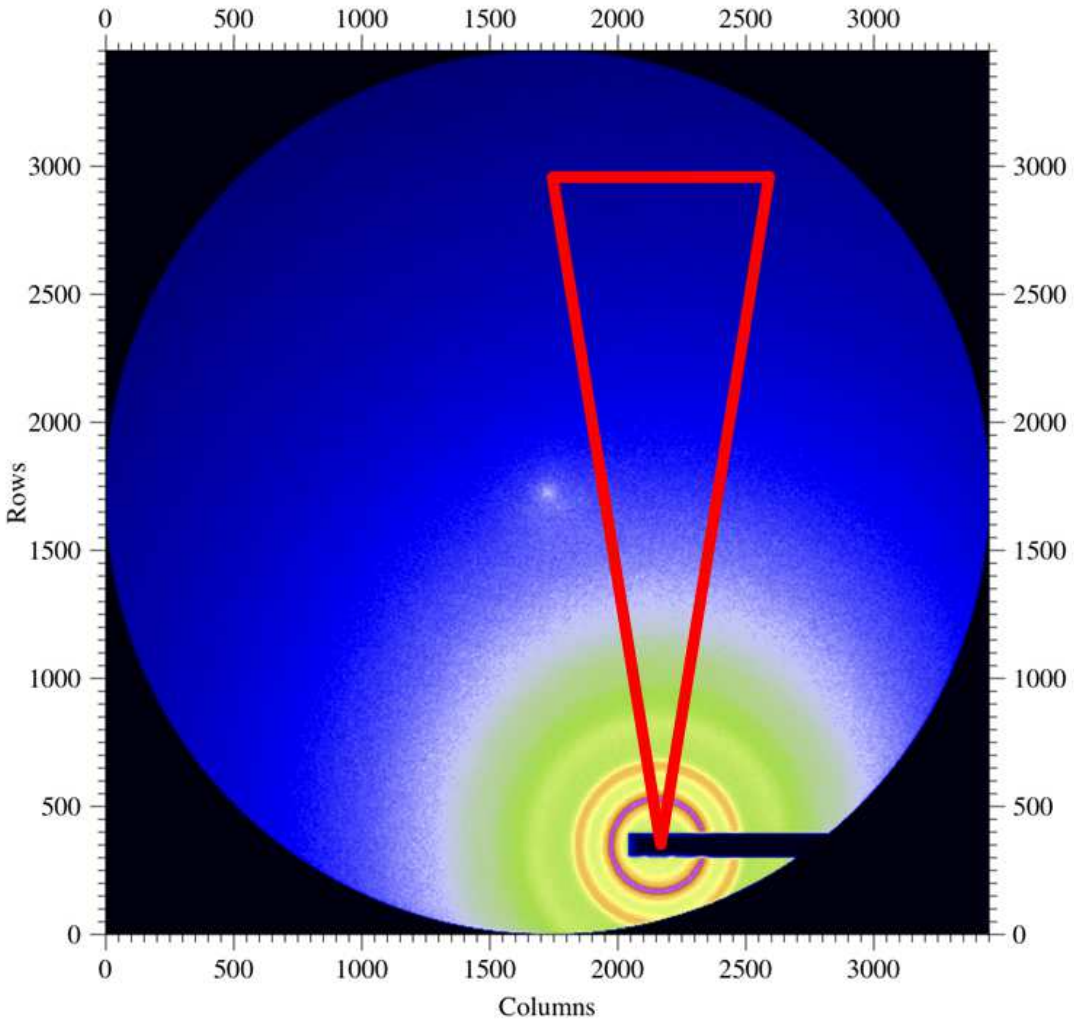

Figure A.5: Image acquired on the capillary containing amorphous GeTe. Only the pixels contained in the vertical triangular sector shown on the figure have been selected for integration. The pixels that appear as a white spot at the center of the image plate are damaged and must be avoided.

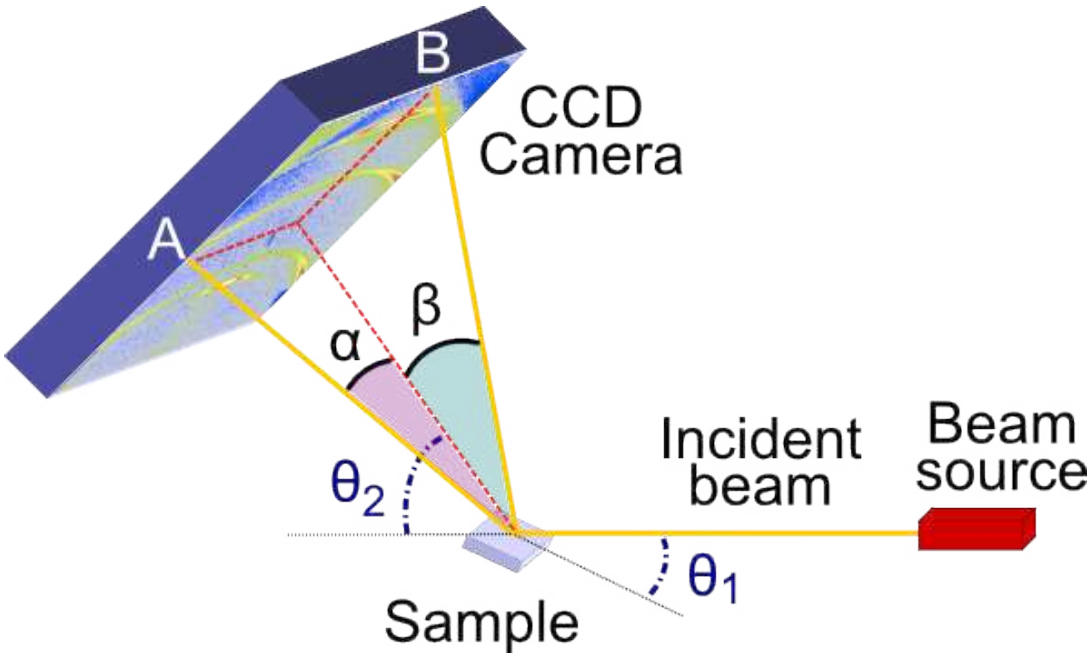

Figure A.6: Schematic representation of the experimental setup used at the synchrotron ESRF. The diffracted beam is collected by a CCD camera at a distance D from the sample of around 20 cm. The camera and the sample are tilted of an angle θ_2 and θ_1 with respect to the incident beam, respectively. If $\theta_1 = \theta_2$, the configuration is in a strict $\theta - 2\theta$ geometry only at the center of the camera.

ESRF data analysis

The diffraction experiments at the ESRF synchrotron (beamline BM02 CRG-D2AM) have been performed in a θ-2θ configuration or in pseudo-grazing incidence, over thin film samples and clusters samples described in Chapters 4 and 3.

The experimental setup is shown in Fig.A.6. The incident beam is directed onto the sample, and the diffracted beam is collected by a CCD camera placed at a distance D from the optical center. The CCD camera is a screen of 1340x1300 squared pixels of 50 μm. The angle between the camera and the incident beam (θ_2) has been chosen to be 17.5°for all the performed experiments, while the angle between the incident beam and the sample surface (θ_1) was 8.75°for the θ-2θ configuration and 4°for the pseudo-grazing configuration used in Chapter 3. The incident angle of 4°cannot be strictly considered as a grazing incidence, but for smaller angles, the beam spot over the sample would have been larger than the

sample size (between 25nm^2 and 400nm^2). The diffracted beams are collected in an angular range $\pm\alpha$ in the horizontal direction and $\pm\beta$ in the vertical direction. Strictly speaking, for θ_1=8.75°the geometry is in a real θ-2θ configuration only at the center of the image. For all other points, the measured intensity collected by the CCD camera is not due to diffraction of planes parallel to the sample surface. In particular, at point B of Fig.A.6 is collected the beam diffracted by a plane rotated by $\beta/2$ around an axis perpendicular to the figure plane. Considering that the CCD camera is almost squared, $\alpha \approx \beta$ and their values depend on the distance D that determines the angular aperture measured by the camera. For example, for the experiment on cluster described in Chapter 3 the signal is measured in a 2θ range from 8° to 26°, meaning that $\alpha \approx \beta \approx 9°$. The exact value of the distance D is calculated for each experiment by measuring the position of the direct beam on the camera without sample for θ_2 values varying between -6°and 6°.

For the experiments described in Chapter 3 on clusters and thin films, the intensity as a function of 2θ has been obtained from each bidimensional image by integrating over the rings (excluding only a border of 100 pixels on each side of the image). A dedicated program, developed on the BM02 beamline, has been used for integration. This program takes into account geometrical corrections, in particular the fact that the camera plane is not vertical so that the diffraction rings are not circles. The resulting angular integrated intensities includes the contribution of all the planes contributing to the measured partial rings on the image, so any information on the texture of samples between this angular aperture is lost in the final result. This means that the final integrated peak positions and widths are the sum of the peaks over the various Ψ, so care must be taken in analyzing their width [95]. However, for non textured samples, as the clusters characterized in Chapter 3, the rings are isotropic and no information is lost with integration.

The samples described in Chapter 3 (GST thin film and nanoclusters) have been studied by XRD as deposited, after ex-situ annealing and also during in situ annealing experiment. In all cases, in order to get the signal of the studied material it is necessary to subtract the contribution of the Si substrate and of

the Al_2O_3 encapsulating material from the measured signal. For this purpose, the signal of a blank sample constituted of a 20 nm thick Al_2O_3 film deposited on a Si substrate has been measured. However, the intensity of the substrate and Al_2O_3 signal in sample measurement is not exactly the same as the one measured for the blank sample, meaning that the intensity diffracted by GST, I_{GST}, should be obtained through the relation

$$I_{GST} = I_{measured} - \alpha I_{Si+Al_2O_3} \tag{A.3}$$

where $I_{measured}$ is the intensity measured for the sample thus including the substrate and Al_2O_3 contributions, $I_{Si+Al_2O_3}$ is the intensity measured for the blank sample and α is a coefficient that needs to be adjusted for each sample. The fact that α is not equal to 1 can be due to many reasons, including a difference in the quantity of Al_2O_3 matter between the samples. It is important to determine α accurately since $I_{Si+Al_2O_3}$ is much larger than I_{GST}. However, a perfect subtraction of the substrate signal could not be achieved. This is probably due to the fact that the relative contributions of the Al_2O_3 signal and Si signal are not the same in the blank sample and in presence of GST.

For the in situ experiments of Chapter 3, the furnace used is the same Anton Paar furnace as for laboratory experiments (section A.2.1), equipped with a PEEK dome. This dome gives an extremely intense undesired diffracted signal, which is two orders of magnitude higher than the GST film signal and even three orders of magnitude higher than the GST clusters signal.

Appendix B

Deposition method

All the thin film studied in this thesis have been deposited by Physical Vapor Deposition (PVD) through sputtering. In this method, a thin film is deposited on the surface of a substrate by condensation of a vapor. The vapor is obtained by bombarding a solid target (cathode) with a plasma and the ejected material is directed onto the substrate (anode). In order to confine plasma on the surface of the target, sputtering sources are equipped with magnetrons that utilize strong electric and magnetic fields to increase the number of ionizing collisions near the target surface.

The deposition apparatus is the Equipement Alliance Concept Cluster ACT200 (BHT, CEA Leti), which is composed of three deposition chambers. The co-sputtering chamber is equipped with three targets of 100 mm of diameter that can be used independently from each other or in co-sputtering to deposit different compounds, and the substrate is a 200 mm Si wafer. The film uniformity is improved by a satellite and sweeping motion of the target. The deposition is done under Ar atmosphere at a pressure of 5 10^{-3} bar. The two other deposition chambers are used to deposit electrodes and capping materials such as Ti, TiN or Ta, while all the phase change thin films are deposited in the co-pulverization chamber. The C-doped GeTe samples studied in Chapter 2 have been deposited into the co-sputtering chamber by using two targets, one of GeTe and another one of C. The N-doped GeTe samples have been deposited by pulverization of a GeTe target in an Ar+N_2 atmosphere. The film thickness is controlled by the deposition time and the power applied to the targets. The thickness uniformity is checked after deposition by 9 points measurements along the wafer diameter and the films compositions are checked through Rutherford Back Scattering (RBS).

List of Figures

List of Tables

Bibliography

[1] G.E. Moore. Cramming more components onto integrated circuits. *Electronics*, 38(8):114–117, 1965.

[2] G. W. Burr, M. J. Breitwisch, M. Franceschini, D. Garetto, K. Gopalakrishnan, B. Jackson, B. Kurdi, C. Lam, L. A. Lastras, A. Padilla, B. Rajendran, S. Raoux, and R. S. Shenoy. Phase change memory technology. *Journal of Vacuum Science & Technology B: Microelectronics and Nanometer Structures*, 28(2):223, 2010.

[3] S. Ovshinsky. Reversible electrical switching phenomena in disordered structures. *Physical Review Letters*, 21(20):1450–1453, November 1968.

[4] S. Raoux and M. Wuttig. *Phase change materials: science and applications*. Springer Verlag, 2008.

[5] N. Yamada, E. Ohno, N. Akahira, K. Nishiuchi, K. Nagata, and M. Takao. High speed overwritable phase change optical disk material. *Japanese Journal of Applied Physics*, 26S4(Supplement 26-4):61–66, 1987.

[6] N. Yamada, E. Ohno, K. Nishiuchi, N. Akahira, and M. Takao. Rapid-phase transitions of $GeTe-Sb_2Te_3$ pseudobinary amorphous thin films for an optical disk memory. *Journal of Applied Physics*, 69(5):2849, 1991.

[7] M. Wuttig and N. Yamada. Phase-change materials for rewriteable data storage. *Nature Materials*, 6(11):824–832, November 2007.

[8] D. Lencer, M. Salinga, and M. Wuttig. Design rules for phase-change materials in data storage applications. *Advanced Materials*, 23(18):2030–2058, May 2011.

[9] G. Betti Beneventi. Characterization and modeling of phase-change memories. *PhD Thesis*, 2011.

[10] D. Ielmini and Y. Zhang. Analytical model for subthreshold conduction and threshold switching in chalcogenide-based memory devices. *Journal of Applied Physics*, 102(5):054517–054517–13, September 2007.

[11] D. Ielmini. Threshold switching mechanism by high-field energy gain in the hopping transport of chalcogenide glasses. *Physical Review B*, 78(3):035308, 2008.

[12] J. A. Kalb. Crystallization kinetics in antimony and tellurium alloys used for phase change recording. *Doctoral thesis, RWTH Aachen University*, 2006.

[13] J. W. Christian. *The Theory of Transformations in Metals and Alloys.* Pergamon Press, 1975.

[14] K. F. Kelton, H. Ehrenreich, and D. Turnbull. Crystal nucleation in liquids and glasses. In *Solid State Physics*, volume Volume 45, pages 75–177. Academic Press, 1991.

[15] O. Penrose. *The Becker-Dring equations for the kinetics of phase transitions.* August, 2001.

[16] D. Turnbull and J. C. Fisher. Rate of nucleation in condensed systems. *The Journal of Chemical Physics*, 17(1):71, 1949.

[17] J. Willard Gibbs. *The scientific papers of J. Willard Gibbs.* Dover, New York, 1961.

[18] D. T. Wu. Nucleation theory. *Solid State Physics - Advances in Research and Applications, Vol 50*, 50:37–187, 1997.

[19] H. E. Kissinger. Reaction kinetics in differential thermal analysis. *Analytical chemistry*, 29(11):1702–1706, 1957.

[20] S. Senkader and D. C. Wright. Models for phase-change of $Ge_2Sb_2Te_5$ in optical and electrical memory devices. *Journal of Applied Physics*, 95(2):504, 2004.

[21] H.Y. Cheng, T.H. Hsu, S. Raoux, J.Y. Wu, P.Y. Du, M. Breitwisch, Y. Zhu, E.K. Lai, E. Joseph, S. Mittal, R. Cheek, A. Schrott, S.C. Lai, H.L. Lung, and C. Lam. A high performance phase change memory with fast switching speed and high temperature retention by engineering the $Ge_xSb_yTe_z$ phase change material. In *Electron Devices Meeting (IEDM), 2011 IEEE International*, pages 3.4.1 –3.4.4, December 2011.

[22] A. Fantini, L. Perniola, M. Armand, J.F. Nodin, V. Sousa, A. Persico, J. Cluzel, C. Jahan, S. Maitrejean, S. Lhostis, A. Roule, C. Dressler, G. Reimbold, B. De Salvo, P. Mazoyer, D. Bensahel, and F. Boulanger. Comparative assessment of GST and GeTe materials for application to embedded phase-change memory devices. In *Memory Workshop, 2009. IMW '09. IEEE International*, pages 1–2, 2009.

[23] E. Gourvest, B. Pelissier, C. Valle, A. Roule, S. Lhostis, and S. Maitrejean. Impact of oxidation on $Ge_2Sb_2Te_5$ and GeTe phase-change properties. *Journal of The Electrochemical Society*, 159(4):H373H377, 2012.

[24] L. Perniola, V. Sousa, A. Fantini, E. Arbaoui, A. Bastard, M. Armand, A. Fargeix, C. Jahan, J.-F. Nodin, A. Persico, D. Blachier, A. Toffoli, S. Loubriat, E. Gourvest, G. Betti Beneventi, H. Feldis, S. Maitrejean, S. Lhostis, A. Roule, O. Cueto, G. Reimbold, L. Poupinet, T. Billon, B. De Salvo, D. Bensahel, P. Mazoyer, R. Annunziata, P. Zuliani, and F. Boulanger. Electrical behavior of phase-change memory cells based on GeTe. *IEEE Electron Device Letters*, 31(5):488 –490, May 2010.

[25] T. Nonaka, G. Ohbayashi, Y. Toriumi, Y. Mori, and H. Hashimoto. Crystal structure of GeTe and $Ge_2Sb_2Te_5$ meta-stable phase. *Thin Solid Films*, 370(1):258–261, 2000.

[26] N. Yamada and T. Matsunaga. Structure of laser-crystallized Ge_2Sb_2 + xTe_5 sputtered thin films for use in optical memory. *Journal of Applied Physics*, 88(12):7020–7028, December 2000.

[27] Shinji Kohara, Kenichi Kato, Shigeru Kimura, Hitoshi Tanaka, Takeshi Usuki, Kentaro Suzuya, Hiroshi Tanaka, Yutaka Moritomo, Toshiyuki Matsunaga, Noboru Yamada, Yoshihito Tanaka, Hiroyoshi Suematsu, and Masaki Takata. Structural basis for the fast phase change of ge[sub 2]Sb[sub 2]Te[sub 5]: Ring statistics analogy between the crystal and amorphous states. *Applied Physics Letters*, 89(20):201910, 2006.

[28] J. Akola and R. Jones. Structural phase transitions on the nanoscale: The crucial pattern in the phase-change materials $Ge_2Sb_2Te_5$ and GeTe. *Physical Review B*, 76(23), December 2007.

[29] A. V. Kolobov, P. Fons, A. I. Frenkel, A. L. Ankudinov, J. Tominaga, and T. Uruga. Understanding the phase-change mechanism of rewritable optical media. *Nature Materials*, 3(10):703–708, September 2004.

[30] S. Hosokawa, T. Ozaki, K. Hayashi, N. Happo, M. Fujiwara, K. Horii, P. Fons, A. V. Kolobov, and J. Tominaga. Existence of tetrahedral site symmetry about Ge atoms in a single-crystal film of $Ge_2Sb_2Te_5$ found by x-ray fluorescence holography. *Applied Physics Letters*, 90(13):131913, 2007.

[31] K. S. Andrikopoulos, S. N. Yannopoulos, G. A. Voyiatzis, A. V. Kolobov, M. Ribes, and J. Tominaga. Raman scattering study of the a-GeTe structure and possible mechanism for the amorphous to crystal transition. *Journal of Physics: Condensed Matter*, 18(3):965–979, January 2006.

[32] K.S. Andrikopoulos, S.N. Yannopoulos, A.V. Kolobov, P. Fons, and J. Tominaga. Raman scattering study of GeTe and $Ge_2Sb_2Te_5$ phase-change materials. *Journal of Physics and Chemistry of Solids*, 68(5-6):1074–1078, May 2007.

[33] J. Akola and R. Jones. Binary alloys of Ge and Te: Order, voids, and the eutectic composition. *Physical Review Letters*, 100(20), May 2008.

[34] R. Kojima, S. Okabayashi, T. Kashihara, K. Horai, T. Matsunaga, E. Ohno, N. Yamada, and T. Ohta. Nitrogen doping effect on phase change optical disks. *Japanese Journal of Applied Physics*, 37(Part 1, No. 4B):2098–2103, 1998.

[35] S. Y. Kim, S. J. Kim, H. Seo, and M. R. Kim. Complex refractive indices of GeSbTe-Alloy thin films: Effect of nitrogen doping and wavelength dependence. *Japanese Journal of Applied Physics*, 38(Part 1, No. 3B):1713–1714, 1999.

[36] S. Privitera, E. Rimini, and R. Zonca. Amorphous-to-crystal transition of nitrogen- and oxygen-doped $Ge_2Sb_2Te_5$ films studied by in situ resistance measurements. *Applied Physics Letters*, 85(15):3044, 2004.

[37] K. Kim, J. Park, J. Chung, S. A. Song, M. Jung, Y. M. Lee, H-J Shin, B. Kuh, Y. Ha, and J-S Noh. Observation of molecular nitrogen in n-doped Ge2Sb2Te5. *Applied Physics Letters*, 89(24):243520–243520–3, December 2006.

[38] L. W. Fang, Z. Zhang, R. Zhao, J. Pan, M. Li, L. Shi, T. Chong, and Y. Yeo. Fermi-level pinning and charge neutrality level in nitrogen-doped $Ge_2Sb_2Te_5$: Characterization and application in phase change memory devices. *Journal of Applied Physics*, 108(5):053708–053708–7, September 2010.

[39] H. Horii, J.H. Yi, J.H. Park, Y.H. Ha, I.G. Baek, S.O. Park, Y.N. Hwang, S.H. Lee, Y.T. Kim, K.H. Lee, U.-In Chung, and J.T. Moon. A novel cell technology using n-doped GeSbTe films for phase change RAM. In *2003 Symposium on VLSI Technology, 2003. Digest of Technical Papers*, pages 177 – 178, June 2003.

[40] S.J. Ahn, Y.J. Song, C.W. Jeong, J.M. Shin, Y. Fai, Y.N. Hwang, S.H. Lee, K.C. Ryoo, S.Y. Lee, J.H. Park, H. Horii, Y.H. Ha, J.H. Yi, B.J. Kuh,

G.H. Koh, G.T. Jeong, H.S. Jeong, Kinam Kim, and B.I. Ryu. Highly manufacturable high density phase change memory of 64Mb and beyond. In *Electron Devices Meeting, 2004. IEDM Technical Digest. IEEE International*, pages 907 – 910, December 2004.

[41] A. Fantini, V. Sousa, L. Perniola, E. Gourvest, J.C. Bastien, S. Maitrejean, S. Braga, N. Pashkov, A. Bastard, B. Hyot, A. Roule, A. Persico, H. Feldis, C. Jahan, J.F. Nodin, D. Blachier, A. Toffoli, G. Reimbold, F. Fillot, F. Pierre, R. Annunziata, D. Benshael, P. Mazoyer, C. Vallee, T. Billon, J. Hazart, B. De Salvo, and F. Boulanger. N-doped GeTe as performance booster for embedded phase-change memories. In *Electron Devices Meeting (IEDM), 2010 IEEE International*, pages 29.1.1 –29.1.4, December 2010.

[42] K. Kim, S. Choi, J. Chung, J. Lee, and S. Heo. Changes in chemical and structural properties of phase-change material GeTe with nitrogen doping and annealing. *Japanese Journal of Applied Physics*, 49(6):061801, June 2010.

[43] C. Peng, L. Wu, F. Rao, Z. Song, X. Zhou, M. Zhu, B. Liu, D. Yao, S. Feng, P. Yang, and J. Chu. Nitrogen incorporated GeTe phase change thin film for high-temperature data retention and low-power application. *Scripta Materialia*, 65(4):327–330, 2011.

[44] G. Betti Beneventi, L. Perniola, V. Sousa, E. Gourvest, S. Maitrejean, J.C. Bastien, A. Bastard, B. Hyot, A. Fargeix, C. Jahan, J.F. Nodin, A. Persico, A. Fantini, D. Blachier, A. Toffoli, S. Loubriat, A. Roule, S. Lhostis, H. Feldis, G. Reimbold, T. Billon, B. De Salvo, L. Larcher, P. Pavan, D. Bensahel, P. Mazoyer, R. Annunziata, P. Zuliani, and F. Boulanger. Carbon-doped GeTe: a promising material for phase-change memories. *Solid-State Electronics*, 6566(0):197–204, November 2011.

[45] P. Noe, J. Y. Raty, G. E. Ghezzi, F. Hippert, E. Souchier, L. Perniola, V. Sousa, A. Persico, E Henaff, M. Tessaire, C. Bichara, and S. Maitrejean. Effect of dopant incorporation in phase change material. *E\PCOS 2012 Proceedings*, 2012.

[46] G. E. Ghezzi, J. Y. Raty, S. Maitrejean, A. Roule, E. Elkaim, and F. Hippert. Effect of carbon doping on the structure of amorphous GeTe phase change material. *Applied Physics Letters*, 99(15):151906, 2011.

[47] D. A. Keen. A comparison of various commonly used correlation functions for describing total scattering. *Journal of Applied Crystallography*, 34(2):172–177, April 2001.

[48] H. E. Fischer, A. C. Barnes, and P. S Salmon. Neutron and x-ray diffraction studies of liquids and glasses. *Reports on Progress in Physics*, 69(1):233–299, January 2006.

[49] T. E. Faber and J. M. Ziman. A theory of the electrical properties of liquid metals. *Philosophical Magazine*, 11(109):153–173, 1965.

[50] M. Micoulaut, J.-Y. Raty, C. Otjacques, and C. Bichara. Understanding amorphous phase-change materials from the viewpoint of maxwell rigidity. *Physical Review B*, 81(17), May 2010.

[51] J-Y. Raty, C. Otjacques, J-P. Gaspard, and C. Bichara. Amorphous structure and electronic properties of the $ge_1sb_2te_4$ phase change material. *Solid State Sciences*, 12(2):193–198, February 2010.

[52] J. Akola and R. Jones. Structure of amorphous $Ge_8Sb_2Te_{11}$ GeTe-Sb_2Te_3 alloys and optical storage. *Physical Review B*, 79(13), April 2009.

[53] C. Bichara and J-Y. Raty. Temperature-induced density anomaly in te-rich liquid germanium tellurides: p versus sp^3 bonding. *Physical Review Letters*, 95(26), December 2005.

[54] J. Akola, J. Larrucea, and R. Jones. Polymorphism in phase-change materials: melt-quenched and as-deposited amorphous structures in $Ge_2Sb_2Te_5$ from density functional calculations. *Physical Review B*, 83(9), March 2011.

[55] T. Chattopadhyay, J. X. Boucherle, and H. G. VonSchnering. Neutron diffraction study on the structural phase transition in GeTe. *Journal of Physics C: Solid State Physics*, 20(10):1431–1440, April 1987.

[56] Alexander V. Kolobov, Paul Fons, Berangere Hyot, Bernard Andre, Junji Tominaga, Yusuke Tamenori, Hideki Yoshikawa, and Keisuke Kobayashi. Local structure of nitrogen in n-doped amorphous and crystalline GeTe. *Applied Physics Letters*, 100(6):061910, 2012.

[57] K. B. Borisenko, Y. Chen, D. J.H. Cockayne, S. A. Song, and H. S. Jeong. Understanding atomic structures of amorphous c-doped $Ge_2Sb_2Te_5$ phase-change memory materials. *Acta Materialia*, 59(11):4335–4342, June 2011.

[58] E. Cho, Y. Youn, and S. Han. Enhanced amorphous stability of carbon-doped $Ge_2Sb_2Te_5$: Ab initio investigation. *Applied Physics Letters*, 99(18):183501–183501–3, November 2011.

[59] Eunae Cho, Seungwu Han, Dohyung Kim, Hideki Horii, and Ho-Seok Nam. Ab initio study on influence of dopants on crystalline and amorphous Ge2Sb2Te5. *Journal of Applied Physics*, 109(4):043705–043705–10, February 2011.

[60] Y.M. Lee, H.J. Shin, S.J. Choi, J.H. Oh, H.S. Jeong, K. Kim, and M.-C. Jung. Nitrogen contribution to N-doped GeTe (N: 8.4at.%) in the structural phase transition. *Current Applied Physics*, 11(3):710–713, May 2011.

[61] J-Y. Raty, P. Noe, G. E. Ghezzi, S. Maitrejean, C. Bichara, and F. Hippert. Vibrational properties and stabilization mechanism of the doped gete phase change material amorphous phase. *Submitted to Phys. Rev. Lett.*, ().

[62] X. Zhou, L. Wu, Z. Song, F. Rao, M. Zhu, C. Peng, D. Yao, S. Song, B. Liu, and S. Feng. Carbon-doped $Ge_2Sb_2Te_5$ phase change material: A candidate for high-density phase change memory application. *Applied Physics Letters*, 101(14):142104–142104–4, October 2012.

[63] Xavier Biquard, Milos Krbal, Alexander V. Kolobov, Paul Fons, Robert E. Simpson, Brangre Hyot, Bernard Andr, Junji Tominaga, and Tomoya Uruga. Effect of doping on global and local order in crystalline GeTe. *Applied Physics Letters*, 98(23):231907–231907–3, June 2011.

[64] B. Liu, Z. Song, T. Zhang, J. Xia, S. Feng, and B. Chen. Effect of n-implantation on the structural and electrical characteristics of $Ge_2Sb_2Te_5$ phase change film. *Thin Solid Films*, 478(12):49–55, 2005.

[65] G. E. Ghezzi, R. Morel, A. Brenac, N. Boudet, M. Audier, F. Fillot, S. Maitrejean, and F. Hippert. Crystallization of $Ge_2Sb_2Te_5$ nanometric phase change material clusters made by gas-phase condensation. *Applied Physics Letters*, 101(23):233113–233113–4, December 2012.

[66] N. Ohshima. Crystallization of germaniumantimonytellurium amorphous thin film sandwiched between various dielectric protective films. *Journal of Applied Physics*, 79(11):8357, 1996.

[67] X. Wei, S. Luping, Z. Chong, C. T.and Rong, and L.H. Koon. Thickness dependent nano-crystallization in $Ge_2Sb_2Te_5$ films and its effect on devices. *Japanese Journal of Applied Physics*, 46(4B):2211–2214, April 2007.

[68] S. Privitera, S. Lombardo, C. Bongiorno, E. Rimini, and A. Pirovano. Phase change mechanisms in $Ge_2Sb_2Te_5$. *Journal of Applied Physics*, 102(1):013516, 2007.

[69] J. Kalb, F. Spaepen, and M. Wuttig. Calorimetric measurements of phase transformations in thin films of amorphous te alloys used for optical data storage. *Journal of Applied Physics*, 93(5):2389, 2003.

[70] S. Raoux, Jean L. J.-S., and A. J. Kellock. Crystallization properties of ultrathin phase change films. *Journal of Applied Physics*, 103(11):114310, 2008.

[71] M. Zacharias and P. Streitenberger. Crystallization of amorphous superlattices in the limit of ultrathin films with oxide interfaces. *Physical Review B*, 62(12):8391, 2000.

[72] R. E. Simpson, M. Krbal, P. Fons, A. V. Kolobov, J. Tominaga, T. Uruga, and H. Tanida. Toward the ultimate limit of phase change in $Ge_2Sb_2Te_5$. *Nano letters*, 10(2):414419, 2009.

[73] W. D. Nix. Mechanical properties of thin films. *Metallurgical Transactions A*, 20(11):2217–2245, November 1989.

[74] H.-Y. Cheng, S. Raoux, C.-W. Cheng, and J. L. Jordan-Sweet. The crystallization behavior of stressed $Ge_2Sb_2Te_5$ phase-change material. *MRS Spring Meeting 2012*, 2012.

[75] F. Oki, Y. Ogawa, and Y. Fujiki. Effect of deposited metals on the crystallization temperature of amorphous germanium film. *Japanese Journal of Applied Physics*, 8:1056, 1969.

[76] H. Homma, I. K. Schuller, W. Sevenhans, and Y. Bruynseraede. Interfacially initiated crystallization in amorphous germanium films. *Applied Physics Letters*, 50(10):594, 1987.

[77] N. Ohshima. Structural analysis and crystallization studies of germaniumantimony tellurium sputtered films on different underlayers. 83(10), 1998.

[78] M. H. Jang, S. J. Park, D. H. Lim, M.-H. Cho, Y. K. Kim, H.-J. Yi, and H. S. Kim. Structural stability and phase-change characteristics of $Ge_2Sb_2Te_5$ nano-multilayered films. *Electrochemical and Solid-State Letters*, 12(4):H151, 2009.

[79] S. Meister, H. Peng, K. McIlwrath, K. Jarausch, X. F. Zhang, and Y. Cui. Synthesis and characterization of phase-change nanowires. *Nano letters*, 6(7):15141517, 2006.

[80] D. Yu, J. Wu, Q. Gu, and H. Park. Germanium telluride nanowires and nanohelices with memory-switching behavior. *Journal of the American Chemical Society*, 128(25):8148–8149, 2006.

[81] S.-H. Lee, Y. Jung, and R. Agarwal. Highly scalable non-volatile and ultra-low-power phase-change nanowire memory. *Nature Nanotechnology*, 2(10):626–630, September 2007.

[82] S.-H. Lee, Y. Jung, and R. Agarwal. Size-dependent surface-induced heterogeneous nucleation driven phase-change in $Ge_2Sb_2Te_5$ nanowires. *Nano letters*, 8(10):3303–3309, October 2008. PMID: 18778106.

[83] S. Raoux, C. T. Rettner, J. L. Jordan-Sweet, A. J. Kellock, T. Topuria, P. M. Rice, and D. C. Miller. Direct observation of amorphous to crystalline phase transitions in nanoparticle arrays of phase change materials. *Journal of Applied Physics*, 102(9):094305, 2007.

[84] Y. Zhang, S. Raoux, D. Krebs, L. E. Krupp, T. Topuria, M. A. Caldwell, D. J. Milliron, A. Kellock, Philip M. Rice, J. L. Jordan-Sweet, and H.-S. P. Wong. Phase change nanodots patterning using a self-assembled polymer lithography and crystallization analysis. *Journal of Applied Physics*, 104(7):074312, 2008.

[85] H. S. Choi, K. S. Seol, K. Takeuchi, J. Fujita, and Y. Ohki. Synthesis of size- and structure-controlled $Ge_2Sb_2Te_5$ nanoparticles. *Japanese Journal of Applied Physics*, 44(10), 2005.

[86] H. R. Yoon, W. Jo, E. H. Lee, J. H. Lee, M. Kim, K. Y. Lee, and Y. Khang. Generation of phase-change Ge–Sb–Te nanoparticles by pulsed laser ablation. *Journal of non-crystalline solids*, 351(43):3430–3434, 2005.

[87] G.-S. Park, J.-H. Kwon, M. Kim, H. R. Yoon, W. Jo, T. K. Kim, J.-M. Zuo, and Y. Khang. Crystalline and amorphous structures of Ge–Sb–Te nanoparticles. *Journal of Applied Physics*, 102(1):013524, 2007.

[88] I. U. Arachchige, R. Soriano, C. D. Malliakas, S. A. Ivanov, and M. G. Kanatzidis. Amorphous and crystalline GeTe nanocrystals. *Advanced Functional Materials*, 21(14):2737–2743, July 2011.

[89] M. A. Caldwell, S. Raoux, R. Y. Wang, H.-S. Philip Wong, and D. J. Milliron. Synthesis and size-dependent crystallization of colloidal germanium telluride nanoparticles. *Journal of Materials Chemistry*, 20(7):1285, 2010.

[90] M. J. Polking, H. Zheng, R. Ramesh, and A. P. Alivisatos. Controlled synthesis and size-dependent polarization domain structure of colloidal germanium telluride nanocrystals. *Journal of the American Chemical Society*, 2011.

[91] R. Morel, A. Brenac, P. Bayle-Guillemaud, C. Portemont, and F. La Rizza. Growth and properties of cobalt clusters made by sputtering gas-aggregation. *European Physical Journal D*, 24(1-3):287–290, June 2003.

[92] H.R. Yoon, W. Jo, E. Cho, S. Yoon, and M. Kim. Microstructure and optical properties of phase-change GeSbTe nanoparticles grown by pulsed-laser ablation. *Journal of Non-Crystalline Solids*, 352(3637):3757–3761, October 2006.

[93] W. K. Njoroge, H.-W. Woltgens, and M. Wuttig. Density changes upon crystallization of $Ge_2Sb_{2.04}Te_{4.74}$ films. *Journal of Vacuum Science & Technology A: Vacuum, Surfaces, and Films*, 20(1):230, 2002.

[94] T. P. Leervad Pedersen, J. Kalb, W. K. Njoroge, D. Wamwangi, M. Wuttig, and F. Spaepen. Mechanical stresses upon crystallization in phase change materials. *Applied Physics Letters*, 79(22):3597, 2001.

[95] D.-M. Smilgies. Scherrer grain-size analysis adapted to grazing-incidence scattering with area detectors. *Journal of Applied Crystallography*, 42(6):1030–1034, October 2009.

[96] S. Meister, D. T. Schoen, M. A. Topinka, A. M. Minor, and Y. Cui. Void formation induced electrical switching in phase-change nanowires. *Nano Letters*, 8(12):4562–4567, December 2008.

[97] V. Weidenhof, I. Friedrich, S. Ziegler, and M. Wuttig. Laser induced crystallization of amorphous $Ge_2Sb_2Te_5$ films. *Journal of Applied Physics*, 89(6):3168, 2001.

[98] L. H. Zhang, E. Johnson, and U. Dahmen. Observations of vacancy-controlled decay of elastic strain caused by phase transformation of small pb inclusions in al. *Acta materialia*, 53(13):36353642, 2005.

[99] K. J. Choi, S. M. Yoon, N. Y. Lee, S. Y. Lee, Y. S. Park, B. G. Yu, and S. O. Ryu. The effect of antimony-doping on $Ge_2Sb_2Te_5$, a phase change material. *Thin Solid Films*, 516(23):88108812, 2008.

[100] M. Wuttig, D. Lsebrink, D. Wamwangi, W. Wenic, M. Gillessen, and R. Dronskowski. The role of vacancies and local distortions in the design of new phase-change materials. *Nature Materials*, 6(2):122–128, December 2006.

[101] J.A. Kalb, M. Wuttig, and F. Spaepen. Calorimetric measurements of structural relaxation and glass transition temperatures in sputtered films of amorphous te alloys used for phase change recording. *Journal of Materials Research*, 22(03):748–754, March 2011.

[102] A. Marmier, K. Kohary, and D. C. Wright. Determination of the anisotropic elastic properties of $Ge_1Sb_2Te_4$. *Applied Physics Letters*, 98:231911, 2011.

[103] S. Raoux, B. Munoz, H.-Y. Cheng, and J. L. Jordan-Sweet. Phase transitions in Ge–Te phase change materials studied by time-resolved x-ray diffraction. *Applied Physics Letters*, 95(14):143118, 2009.

[104] M. Chen, K. A. Rubin, and R. W. Barton. Compound materials for reversible, phasechange optical data storage. *Applied Physics Letters*, 49(9):502–504, September 1986.

[105] C. V. Thompson and R. Carel. Stress and grain growth in thin films. *Journal of the Mechanics and Physics of Solids*, 44(5):657673, 1996.

[106] B.J. Mrstik, H.L. Hughes, P. Gouker, R.K. Lawrence, and P.J. McMarr. The role of nanoclusters in reducing hole trapping in ion implanted oxides. *IEEE Transactions on Nuclear Science*, 50(6):1947 – 1953, December 2003.

[107] A.P. Hammersley. FIT2D: an introduction and overview. *ESRF Internal Report, ESRF97HA02T*, 1997.

[108] X. Qiu, J. W. Thompson, and S. J. L. Billinge. PDFgetX2: a GUI-driven program to obtain the pair distribution function from x-ray powder diffraction data. *Journal of Applied Crystallography*, 37(4):678–678, July 2004.

Acknowledgments

First of all, I would like to thank with all my heart my Thesis Director Françoise Hippert. With her exceptional energy and dedication to work, not to mention her sense of humor, she helped and encouraged me constantly through these three years like no-one else could do. I learnt much from her, and we had such wonderful (even when hard!) times between synchrotrons, office work at night and conferences that filled those three years with beautiful memories I will never forget. My deep gratitude goes also to the co-Director of this thesis, Sylvain Maitrejean, that was able to take care of me even if time was never enough, always with an optimistic aptitude that can make any problem easier. I would also like to thank with all my heart Frederic Fillot, who taught me so much and with whom I had many wonderful conversations that I really treasure. I wish we had more time to spend together.

A great thank goes to all the PCM team of CEA Leti. First of all to the project leader Véronique Sousa and to Pierre Noe, not only for their competence in work, patience, dynamism and optimism, but also for being the best companions that one can desire when night never comes in Finland. I thank Luca Perniola, great worker and solid reference for all the italians PhD students, for the fruitful discussions and for the good laughs. Thanks to Olga Cueto for helping me with learning COMSOL, to Alain Persico, Carine Jahan, Jean-François Nodin, Christope Vallee, Philippe Michallon, and to everyone that I could have forgotten to add. Thanks to Anne Roule, Mathieu Petit and Ewen Henaff for the thin films samples depositions. I deeply thank Robert Morel and Ariel Brenac for their

wonderful clusters deposition and for the good time we had while characterizing them, as well as for their enormous knowledge and competence that helped me so much. I am particularly grateful to Jean-Yves Raty, who can find a theoretical explanation for all our experimental evidences even before they are found (really impressive!). Thanks to Jean-Paul Simon, Nathalie Boudet and Jean-François Bérard, that were our precious contact on the BM02 D2NT beamline at the ESRF, and to Erik Elkaim that supported us so much at SOLEIL.
My gratitude goes to all the PhD students of the laboratory, old and new. I would like to thank in particular Audrey who is one of the kindest persons I have ever met, and my wonderful cobureau Kavita, Sylvia, Raul and Bilel with whom I divided for almost two years a small office room that felt like home. I deeply thank all the PhD students of the PCM group, each of whom placed its brick in building the PCM project: Giovanni e Stefania, Emmanuel, Jean Claude, Eddie, Gabriele, Quentin, Manan, the sweet Sarra and everyone else.
I hope I did not forget anyone, and I apologize if I did so. Thank you all, I wish you all the best.

I would like to make some more personal acknowledgments and the best thing to do is to write them in the own language of the persons I would like to thank.

Il primo ringraziamento va alla mia splendida, sgangherata famiglia grenoblese, passata e presente: Lia, Ramo, Chiara, Gan, Vera, Paolo, GBB e Stefania, Giova1, Siméon, Eric, Caro, Giova2, Ricky, Carlo e Clio+Panga, Cus, Fil... Senza di voi sarei disperata (e probabilmente sotto un ponte (ˆ.-)). Siete davvero la mia famiglia, e questa tesi esiste grazie a voi.
Je remercie encore une fois Françoise, pas dans son rôle de Directrice de thèse mais plutôt comme une chère amie qui a partagé avec mois le travail de ces trois années. Merci pour tout, je n'ai pas les mots pour t'exprimer ma gratitude. Merci aussi à Robert, l'extraordinaire mari de Françoise, pour sa gentillesse, son esprit agréable, les conversations en italien et l'habilité infaillible de trouver les meilleurs restos à San Francisco et à Helsinki. Merci à Sylvain qui a été toujours prêt à m'aider quand j'en ai eu besoin, et qui ma toujours donné des bons conseils. Merci à Fred, qui m'a aidé beaucoup pendent mes premiers jours au

Leti. Merci encore à l'équipe PCM, formée des personnes tellement agréables que travailler avec eux c'est un plaisir. Un merci et un biz à Pilou et à Georgette! Je remerci beaucoup Robert et Ariel pour la gentillesse et les moments de bonheur, et le très sympa Jean-Yves sans lequel cette thèse n'aurait que trois chapitres.

Merci encore à mes amies Audrey, Kavita, Sylvia, aux thésards du labo et du projet, et merci aussi aux thésards DCOS "collègues de Lia" pour les repas bien passés. Merci à Radekko, Cornelia, Pablo et à tout les autres "étrangers de Grenoble" qui forment une communauté très chaleureuse.

Ringrazio gli amici lasciati a Milano, che non mi hanno dimenticata in questi tre anni: la Piera, che resta la mia insostituibile migliore amica, Deiv e i suoi cappelli che amo immensamente, Albe, Eleele e Qc (e il terzo incomodo), Vera, Noja, Rezzo, il Niggah, Vanish, Dade, Tumji e Sunday, la Brini, Matt e il sempregiovane Frank. Un pensiero pieno di gratitudine va a Marco, che mi ha accompagnata alla soglia di questo viaggio, e alla sua famiglia. Ringrazio con tantissimo affetto le meravigliose amiche del giardino, Gloria, Rubina, Elisa, Stefania e Tosca, che tra alti e bassi e nonostante la lontananza restano un caposaldo fondamentale della mia vita. Grazie di cuore a tutta la famiglia Arbrun/Maurino, ed in particolare a Matilde, Ezio e Floriana, per avermi accolta con tanto affetto.

Rigrazio con tutto il cuore il mio Stefano, compagno della difficile stesura di questa tesi e compagno della mia vita, senza il quale nulla avrebbe senso. Grazie per essere stato con me in questa avventura, e per tutte quelle che ancora ci aspettano.

Il ringraziamento più sentito e profondo va alla mia piccola ma solida famiglia: Ernesto, Antonella, Nike, Serena e Giò, Angelo e Silvia, i miei nonni. In particolare, tutta la mia gratitudine va a mamma e papà. Il vostro amore, la comprensione e il supporto che mi avete sempre dato sono la base su cui poggia la mia vita.

Abstract

Phase Change Memories (PCM) are one of the best candidates for the next generation of non volatile memories. A great research effort is still needed in order to optimize the properties of phase change (PC) materials which are used in PCM devices. In particular, doping has been demonstrated to improve retention in devices. Moreover, a study of the effect of scaling and interface material on PC materials properties is still an open research field. In this context, the first part of the thesis is dedicated to investigate the local structure of C or N doped amorphous GeTe. The impact of doping is observed experimentally with the appearance of a new peak in the pair distribution function of doped GeTe, indicating the formation of a bond at a new distance that is absent in the undoped amorphous material. The presence of new environments involving carbon and nitrogen is confirmed through ab initio simulations. The subject of the second part of this thesis is the impact of confinement on $Ge_2Sb_2Te_5$ (GST) crystallization mechanism. Nano-sized clusters of GST have been made by sputtering, deposited and then studied through X-ray diffraction using synchrotron radiation. The crystalline clusters experience a tensile strain that can be ascribed to the effect of the embedding Al_2O_3 matrix. Their crystallization temperature has been found to be only 25°C higher than the one observed for a thin film of GST of 10 nm deposited under the same conditions. This result is positive for the future development PCM because it indicates that the scaling effect on the crystallization temperature in phase change material can be small. The third and last part of the thesis is dedicated to the investigation of the interface material effect on the crystallization temperature of GeTe and GST thin films through reflectivity and X-ray diffraction measurements. In both GeTe and GST film 100 nm thick interfaced with Ta the crystallization temperature is higher than in the case of TiN or SiO_2 interface. Such an interface effect on relatively thick films was never reported before. The results suggest that the SiO_2 /GeTe interface is energetically favorable for the nucleation and growth of grains with a preferred orientation and that nucleation and growth mechanisms are different for different interface materials.

Résumé

Les mémoires à changement de phase sont l'un des candidats les plus prometteurs pour la prochaine génération de mémoires non-volatiles. Un intense effort de recherche est requis pour optimiser les matériaux à changement de phase (PC) utilisés dans ces mémoires. En particulier, il a été démontré que le dopage améliore les propriétés de rétention des dispositifs. Par ailleurs, l'étude des effets de réduction de taille et des effets des matériaux d'interface sur les propriétés des matériaux à changement de phase est encore un sujet de recherche ouvert. Dans ce contexte, la première partie de la thèse est dédiée à l'investigation de la structure locale de GeTe amorphe dopé avec C ou N. L'effet du dopage sur la structure a été observé expérimentalement via l'apparition d'un nouveau pic dans la fonction de distribution de paires de GeTe dopé, ce qui montre la formation d'une nouvelle liaison interatomique absente dans le matériau non dopé. La présence de nouvelles configurations incluant le carbone et l'azote a été confirmée par des simulations ab initio. L'objet de la deuxième partie de la thèse est l'influence de la réduction de taille sur la cristallisation de $Ge_2Sb_2Te_5$ (GST). Des agrégats nanométriques de GST ont été fabriqués par pulvérisation puis déposés et étudiés par diffraction des rayons X en utilisant le rayonnement synchrotron. Dans l'état cristallisé une très forte déformation positive des agrégats est observée et attribuée à la matrice d'Al_2O_3 qui entoure les agrégats. La température de cristallisation des agrégats est de 25°C plus élevée que celle d'un film de GST de 10 nm déposé dans les mêmes conditions. Ce résultat est encourageant pour les futurs développements des mémoires à changement de phase car il montre que l'effet de réduction de taille sur la température de cristallisation peut-être faible. La troisième et dernière partie de la thèse est dédiée à l'investigation des effets des matériaux d'interface sur la température de cristallisation de films minces de GeTe et GST par des mesures de réflectivité et de diffraction des rayons X. Pour les deux matériaux, la température de cristallisation de films de 100 nm est plus grande pour une interface avec du Ta que pour une interface avec du TiN ou du SiO_2 . Une différence aussi marquée n'était jamais montré auparavant. Les résultats suggèrent que l'interface SiO_2 /GeTe est énergétiquement favorable pour la nucléation et la croissance de grains avec une orientation préférentielle et que les mécanismes de nucléation et croissance sont différents pour différents matériaux d'interface.